1640

Institut de physique
Université de Neuchâtel

Far-infrared Quantum Cascade Lasers

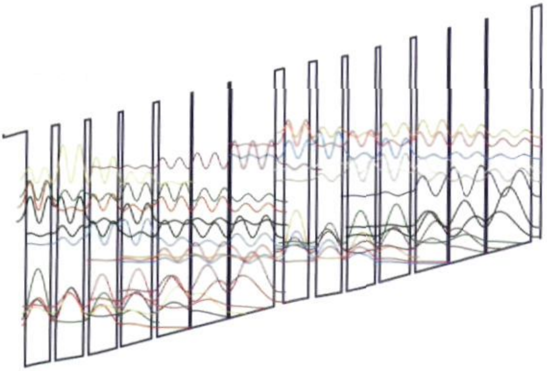

Thèse de doctorat

présentée à la

Faculté des Sciences
de l'Université de Neuchâtel

par

Michel Rochat

Neuchâtel, 2002

Institut de physique
Université de Neuchâtel

Far-infrared Quantum Cascade Lasers

Thèse de doctorat

présentée à la

Faculté des Sciences
de l'Université de Neuchâtel

par

Michel Rochat

Neuchâtel, 2002

IMPRIMATUR POUR LA THESE

Far-infrared Quantum Cascade Lasers

de M. Michel Rochat

UNIVERSITE DE NEUCHATEL

FACULTE DES SCIENCES

La Faculté des sciences de l'Université de Neuchâtel sur le rapport des membres du jury,

MM. J. Faist (directeur de thèse)
P. Martinoli, K. Unterrainer (Vienne)
et C. Sirtori (Paris)

autorise l'impression de la présente thèse.

Neuchâtel, le 26 août 2002

Le doyen:

F. Zwahlen

Pour Catherine et Léa

Résumé

Cette thèse traite du développement des lasers à cascades quantiques (QC) dans l'infrarouge lointain ($\lambda > 34\mu m$). A la différence des lasers semi-conducteurs inter-bandes, la technologie des cascades quantiques utilise des transitions inter sous-bandes unipolaires. Les transitions ont lieu entre des états électroniques dans des puits quantiques créés par des couches semi-conductrices déposées par jets moléculaires (MBE). Une émission laser utilisant cette technologie a été démontrée pour la première fois dans l'infrarouge moyen ($\lambda = 4.2\mu m$) utilisant une alternance de couches InGaAs/AlInAs. La force de cette technologie est la capacité de réaliser une émission laser sur une large bande spectrale par ingénierie de bande électroniques avec un couple donné de matériaux ($\lambda = 3.2\mu m$ jusqu' à $\lambda = 24\mu m$ pour le couple InGaAs/AlInAs).
L'objectif de ce travail était la réalisation d'une émission laser utilisant cette technologie à une longueur d'onde supérieure à la bande *reststrahlen*, où l'énergie du photon est inférieure à celle des phonons optiques des matériaux utilisés. Pour les lasers QC dans l'infrarouge moyen, l'émission de phonons optiques est le processus non-radiatif principal utilisé pour obtenir une inversion de population électronique. Dans l'infrarouge lointain, ce processus ne peut être utilisé et d'autres processus sont donc nécessaires pour obtenir une inversion de population électronique. Le premier pas vers un laser QC-FIR a été obtenu avec la démonstration d'une électro-luminescence dans l'infrarouge lointain par une hétéro-structure basée sur transition optique verticale. La dynamique électronique de cette structure à été étudiée par la mesure de la dépendance de l'intensité lumineuse avec l'augmentation de la température. Ces mesures ont montré que dans cette structure, l'interactions électron-électron est le processus non-radiatif dominant aux basses températures. La population électronique à été calculée en résolvant les équations de bilan stationnaires. Les résultats ont montré que le taux d'extraction des électrons de l'état fondamental est le principal goulet d'étranglement limitant la formation d'une inversion de population électronique. Afin d'obtenir un effet laser, il est nécessaire d'avoir un milieu amplificateur avec un gain suffisant et un résonateur avec de faibles pertes. Un guide d'onde double plasmon a été créé et des mesures de pertes de guide ont été effectuées. Les résultats montrent que de tels guides d'ondes ont des pertes trop importantes pour atteindre le seuil laser avec ce type de structure.
Une structure QC de type super-réseau avec une extraction optimisée des états inférieurs a été crue. De plus, un guide d'onde simple plasmon utilisant un substrat semi-isolant pour le confinement a permis de réduire notablement les pertes. Une émission laser à $\lambda = 69\mu m$ a été obtenue jusqu'à une température de 44K.

Abstract

This thesis reports on the development of far-infrared ($\lambda > 34\mu m$) quantum cascade (QC) lasers. In contrast to interband semi-conductor lasers, the quantum cascade technology is based on unipolar intersubband transitions. The transitions occur between electronic states in quantum wells engineered by deposition of semi-conductor heterolayers by molecular beam epitaxy (MBE). Laser action using this technology was first demonstrated in the mid-infrared using InGaAs/AlInAs hetero layers at $\lambda = 4.2\mu m$. The strength of this technology is the possibility to achieve laser action over a very broad range of wavelengths using electronic band engineering for a given couple of materials ($\lambda = 3.2\mu m$ up to $\lambda = 24\mu m$ for the InGaAs/AlInAs material pair).

The objective of this work was to achieve laser action using the same technology at wavelength above the *reststrahlen* band, where the photon energy is smaller than the optical phonon energies of the materials. In mid-infrared QC lasers, the emission of optical phonons is the main non-radiative scattering process used to achieve population inversion. In the far-infrared, this scattering process cannot be used and other scattering processes are necessary. The first step towards laser action was achieved with the demonstration of electroluminescence from a vertical transition quantum cascade structure in the far-infrared. The electronic dynamics was studied with temperature dependent measurements of the emission intensity. These measurements demonstrated that electron-electron scattering is the dominant nonradiative scattering process at low temperature in such structures. The electronic population has been calculated by solving the steady state rate equations. The results show that the extraction of the carrier from the ground state is the main bottleneck limitating population inversion build-up in the structure. Laser action requires both an active region and a low loss resonator in the considered spectral region. A double plasmon waveguide was designed and waveguide loss measurements have been performed. Results from these measurements show that such a waveguide exhibited too high losses to achieve laser action with the available active regions.

A chirped supperlattice QC structure was then designed where the extraction from the lower states of the optical transition is enhanced. Furthermore, a single plasmon waveguide, where a semi-insulated substrate is used as lower cladding was designed to achieve low losses. Laser action at $\lambda = 69\mu m$ was finally demonstrated up to 44k.

Contents

Chapter 1

Introduction

1.1 Introduction and Motivation

The history of the LASER, acronym for light amplification by stimulated emission of radiation, starts as early as 1917 when A. Einstein predicted the phenomenon of stimulated emission.[1] The first realization of a stimulated emission amplifier and oscillator by Townes and co-workers occurred in 1954 with the MASER in the microwave spectral region. After a theoretical study done by Schawlow and Townes concluding on the possibility of stimulated amplification in the visible, Maiman builds the first ruby optical MASER or laser in 1960.[2] The laser amplifier operating range covers today most the electromagnetic spectra from the microwave and up the ultraviolet. The amplifying laser media can be in any physical state of matter (liquid, solids, vapor and even plasma) where a population inversion can be produced. The inversion is generally reached by either optical or electrical pumping. The applications are as numerous as various going from eye surgery to heavy industry, from gas sensing to

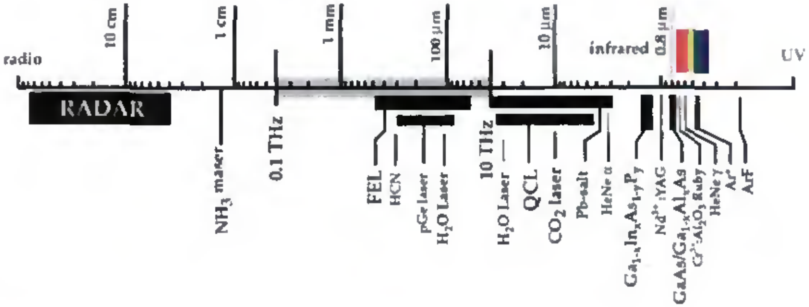

Figure 1.1: Electromagnetic spectrum ranging from the millimetric to the sub-nanometric wavelength range. A lack of convenient powerful room-temperature operating sources is observed in the terahertz spectral region.

data storage via telecommunications. The latter field is a powerful technological engine for the development of laser sources as the needs are very specific and demanding. The need for low cost, robust, high power, small sized, room temperature operating and spectrally well defined laser sources is increasing. The market needs for such laser is enormous and increasing meaning that important resources are available for their development. In 1962 semiconductor laser have simultaneously been demonstrated by three groups (Hall *et al.*, Nathan *et al.* and Quist *et al.*).[3] They have become key components as they demonstrate very high performances capabilities and are even now entering new fields where more traditional gas and solid state laser are usually used due to high power requirements. High performance semiconductor lasers are essentially available from mass production in the near-infrared and infrared spectral region. In the mid and far-infrared the need for high power, frequency tunable and user friendly laser sources is increasing in fields such as environment monitoring, medical imaging, astronomy and telecommunications.[4, 5, 6] Even if various efficient laser sources are available, they usually are unpractical for many applications being huge in size and unaffordable such as the free electron laser or need specific operating conditions as the p-Ge or lead-salt lasers.[7]

The demonstration of the quantum cascade laser (QCL) in 1994 at AT&T Bell laboratories by Faist and coworkers opened a new trail in the development of mid and far-infrared lasers. This type of laser differs in a fundamental way from traditional bipolar semiconductor as the optical transition occurs between subbands with only one type of charge carrier. The realization of this laser relies totally on energy band structure engineering. In traditional gas or solid state laser, the optical transition occurs between naturally available atomic or molecular energy states. With the QCL technology, the possible transition energies are not bound by the semiconductor bandgap, but by the bandgap offset of two different semiconductors. As shown in Fig. 1.2 compounds with different bandgaps and similar lattice parameter are available from III-V semiconductors. This allows the growth of monocrystals with alternate succession of layers of different semiconductor material with different band edge creating an artificial energy band structure. This alternate succession of hetero-junctions form potential wells where carriers can be trapped and confined (Fig. 1.3). Confinement of the carriers inside the well forces them to occupy discrete energy levels and optical transitions between these energy levels are possible. Suggestions to use electrically pumped intersubband optical transitions for laser action has been proposed by Kazarinov and Suris in 1971. In their proposal, light amplification is due to the transition of an electron from the ground state in one quantum well to an excited state in an other quantum

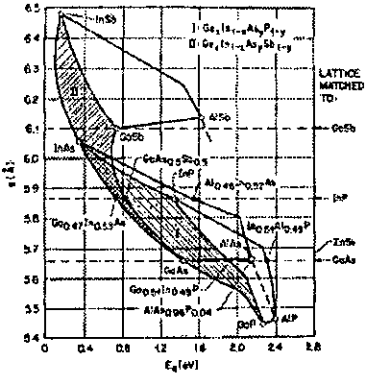

Figure 1.2: Lattice parameter versus energy gap at room temperature for various III-V compounds and their alloys.[8]

well which is accompanied by photon emission.[9] Population inversion is possible due to relatively long non-radiative relaxation time between adjacent wells compared to the desexcitation time inside the well. Optical intersubband transitions at semiconductor-insulator interfaces have been experimentally observed in photo-induced experiments by Wheeler *et al.* in 1975. One year later (1976) Gornik and Tsui detected hot-electron induced infrared emission caused by intersubband transitions.[10, 11] In 1985 West and Eglash reported the first observation by infrared absorption of a direct intra-conduction band transition between square quantum well states.[12] This was made possible by the development of extremely high precision epitaxial growth techniques such as the molecular beam epitaxy (MBE).[13] Helm *et al.* successfully implemented Kazarinov and Suris proposal with the observation of intersubband electro-luminescence from quantum wells.[14, 15] But no laser action was observed in such structures. Many proposals for the realization of a quantum cascade laser

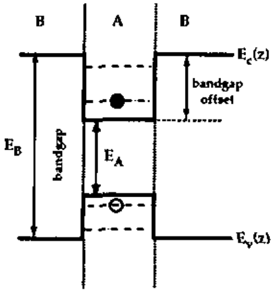

Figure 1.3: Conduction and valence band profile in a type I heterostructure.

were made [16, 17, 18, 19, 20, 21, 22] but a new step was achieved in 1993 when Faist *et al.* demonstrated intersubband electro-luminescence at $\lambda = 5\mu m$ up to room temperature from a quantum-well cascade structure.[23] With this structure they claimed population inversion and possible laser action when embedded in a suitable waveguide. Laser action was demonstrated a few months later at a wavelength of $\lambda = 4.2\mu m$.[24] Since then the evolution of the QCL has been constant and very recently room temperature continuous wave operation has been achieved at a wavelength of $\lambda = 9.1\mu m$.[25]

The spectral limit of the quantum cascade technology is fixed on the high energy side of the electromagnetic spectra by the maximum bandgap offset. The large bandgap offset of the $Ga_{0.47}In_{53}As - In_{0.48}In_{0.52}As$ hetero junction of $\Delta E_c = 0.52eV$ enables to design QC laser up to a wavelength of $\lambda = 3.4\mu m$.[26] On the low energy side of the spectrum, laser action has been achieved up to a wavelength of $\lambda = 24\mu m$ using the QCL technology [27] but is virtually only limited by level broadening due to monolayer fluctuation of the hetero junctions.[10] Practically intersubband emission was observed up to a wavelength of $\lambda \approx 140\mu m$ by Helm

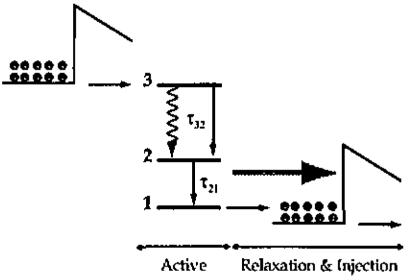

Figure 1.4: The quantum cascade design philosophy is to divide each cells in an active region and an injection region . The latter is used to selectively inject carriers at the with the desired energy into the active region.

and co-workers.[14]

The realization of a quantum cascade laser is a difficult task because of fast non-radiative relaxation processes present with the emission of optical phonons. The success of the QCL in the mid-infrared was to design a structure with an intersubband optical transition larger than the optical phonon energy and to take advantage of these fast relaxation processes to induce a population inversion. As shown in Fig. 1.4, the active region where the population inversion and gain takes place consist schematically of a ladder of three states engineered to maintain a population inversion between states n=3 and n=2. This is reached when the total non-radiative rate τ_2^{-1} out of level n=2 is higher than total non-radiative rate τ_{32}^{-1}.[22] By designing the energy difference ΔE_{21} in resonance with optical phonon emission energy, depopulation of state n=2 is extremely fast and population inversion may be achieved. An relaxation/injection is then necessary to cool down the electrons and re-inject them into the next period. In the far-infrared, i.e beyond the *Reststrahlen* region, the optical transition is smaller than the optical phonon emission energy ($\Delta E_{32} < \Delta E_{21}$). A structure design with the far-infrared optical transition above states in resonance with the optical phonon energy transition should not be possible without a magnetic field. Optical phonon emission from state n=3 to state n=1 is much likely to happen as only small momentum exchange is required. Depopulation of level n=3 will therefore be very efficient preventing any population inversion. Furthermore, as shown in this work, non-radiative electron-electron scattering is very efficient between states n=3 and n=2. In contrast in the mid-infrared optical phonon emission from level n=3 is much more likely happen to level n=2 than to level n=1. Carrier dynamics in far-infrared structures is thus totally different in the mid-infrared for this structure scheme.

Many attempts to obtain a far-infrared source have been made using intersubband transitions in quantum wells. Luminescence was successfully demonstrated from Helm *et al.* implementation of Kazarinov and Suris proposal. However no laser action was demonstrated from such a structure.[15] An other approach was tried in 1996 by Maranowski *et al.* with emission from parabolically graded quantum wells with demonstration of far-infrared electroluminescence.[28] Gain in an ideal parabolic potential is in principle impossible on any given optical transition since the next higher transition is capable of absorbing photons at the same energy. Since then mainly three groups have published emission from QC structures in the far-infrared. Emission from a three level QC diagonal structure with an optical phonon was achieved by Xu and Williams *et al.*[29, 30] and from a vertical and a diagonal transition with no optical phonon by us and Ulrich *et al.*.[31, 32, 33]

1.2 Scope and Organization of the text

The objective of the present work is to achieve laser action in a quantum cascade structure beyond the *reststrahlen* band, i.e at wavelengths beyond $\lambda \approx 34\mu m$. Chapter 2 is a presentation of the used techniques and equipment for sample processing and characterization. The first generation of luminescence samples is discussed in chapter 3. Both the vertical and the diagonal intersubband transitions are explored to demonstrate the possibility of far-infrared electro-luminescence from a quantum cascade structure designed with an injector and an active region. Electrical and optical properties of the samples are performed to understand the physical properties of the devices. In chapter 4 electronic dynamics in the heterostructure is explored. Understanding of the electron dynamics in the QC structure is the key for the design of an active region with optical gain. In chapter 5 the other key component of a laser is discussed. The design and realization of a low loss optical resonator for far-infrared wavelengths is demonstrated. Waveguide characterization of the loss and gain are performed. In chapter 6 a second generation of QC structures are designed and tested. These structures are expected to have increased gain compared with the first generation. Performance of the waveguide is increased to achieve laser action in the far-infrared. A mid-infrared high performance laser structure is optimized for mid-infrared long-wavelength and characterized for further optimization of the laser performances in the far-infrared.

Chapter 2

Sample Processing and Characterization

2.1 Sample Processing

The first process into the realization of our samples is the growth of the crystals. The stating material for a MBE growth is a two inch GaAs or InP substrate. They serve as crystalline seed for subsequent crystal deposition. In general, a quantum cascade (QC) structure starts with a highly doped contact layer followed by the QC hetcterostructure and is terminated by a top contact layer (fig. 2.1). This process is done by Molecular Beam Epitaxy (MBE)on both the InP and GaAs material system.[13, 34] The first quality test operated on the new-grown samples is an X-ray diffraction. The results of this measurement allows us to measure the periodicities of the crystal, and particularly the periodicity of the repeated Quantum Cascade (QC) structure. Knowing the periodicity we can then estimate the real thicknesses

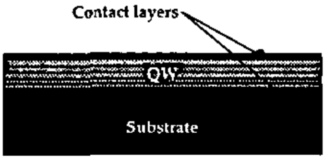

Figure 2.1: The QC structure consists in general of a heterostructure grown between two contact layers on a substrate by MBE.

of the layers and use these experimental values to re-simulate the structure.

Commonly three different processing of the sample is performed. Namely they are the surface emission, where the light is extracted by the surface of the sample, the edge emission, and finally the "Schottky" processing used for doping characterization.

The processing are performed in clean room conditions using contact lithography and wet chemical etching. It starts by a cleaning sequence of trichloroethylene, acetone and isopropanol baths. The samples are then dehydrated at a temperature of 160^0C for 3 minutes. This dehydratation of the samples has shown to significantly increase the adherence of the photo-resist to the semi-conductor surface. Shipley 5214 photo-resist is then deposited on the samples and spined at 5000 RPM. This allows to obtain an average thickness of $1.5\mu m$. During the spinning, resist accumulates in the corners of the sample and must be removed manually with a thin glass plate before any further action. The samples are then heated for 120s at a temperature of 110^0C to dry the resist. The samples are then exposed to ultra violet light through a quartz window with patterns. The exposed surface is then removed chemically by immersion of the sample into a developer (Microposit Developer) for 40-60 seconds leaving the unexposed patterns. Depending on the stage of the processing, either metallic depositions or wet chemical etching is performed. The metallic deposition is performed by electron-beam evaporation under high vacuum ($3 \times 10^{-7} - 1 \times 10^{-6} mbar$). Depending on the type of contacts which are chosen, either non alloyed Ti/Au (10/400nm) or alloyed Au/Ge/Ag/Au (12/27/50/100 nm) contacts are deposited. The metal is then selectively removed with the dissolution of the resit using acetone ("Lift-off"). Before chemical etching, on the other hand, the resist must be post baked during 60s at 110^0C. This increases further more the adherence of the resist on the edge of the patterns preventing localized under-etch and leads to sharp edges. The etching is performed by the use of $H_2SO_4 : H2O_2 : H_2O$ for GaAs material system. The relative concentration of the various components is 1:8:1 with an etching rate of $0.1\mu m/s$ at room temperature while shaking the sample at 1 Hz. The rate can be controlled by changing the relative concentration of H_2O_2. This rated decreases with a decrease of its concentration. In the InP material system, $HBr : HNO_3 : H_2O$ etching solution is used. The etching rate is typically $0.5\mu m/minute$.

2.2 Coupling light with ISB Quantum Wells

In order for an electromagnetic wave to interact with an intersubband transition, it must satisfy the intersubband selection rule.[35] This rule requires that a propagating wave in the plane of the layers must have its electric-field vector parallel to the growth axis of the structure (Fig. 2.2. Specific waveguide geometries, as a multi-pass 45^0 wedge waveguide geometry (Fig. 2.3(a)), are therfore necessary to perform absorption experiments on quantum wells. [36, 37, 38, 39, 40, 41] For infrared emission experiments, similar configuration could in principle be used, but practically other configurations are more suitable. In the far infrared, the intersubband spontaneous emission power is expected to be in the pico-watt range. These low intensities together with increased Drude absorption compared to the mid-infrared ($\alpha \approx \lambda^2$), requires a coupling method with short optical path length inside the material. Two approaches can be used to fulfill the required conditions. The first is to process the samples in a waveguide configuration, the light being extracted from the edge of the sample. This method in not straight forward and is a major challenge of this work (chapter 5). The second approach is much more simple and is done with the use of a grating coupler (Fig. 2.5). This technique allows us to extract the light directly through the surface of the sample, reducing considerably the optical path length. As shown in Fig. 2.4 the action of the grating is to diffract the light falling normal to the sample surface nearly parallel to the surface. Similarly for an intersubband emission, the grating will diffract the light traveling parallel the layers into a light traveling normal to the layers and may then escape from the surface.[42, 43, 41]. It has been shown experimentally that the coupling efficiency is proportional to the ratio of the grating period p to the intersubband emission wavelength in the material λ/n, where n is the material refractive index. [14] Two regime appear depending on the grating periods. If the grating period p is greater than λ/n the

Figure 2.2: To couple light with ISB quantum wells, the electric field vector must be normal to the layer.

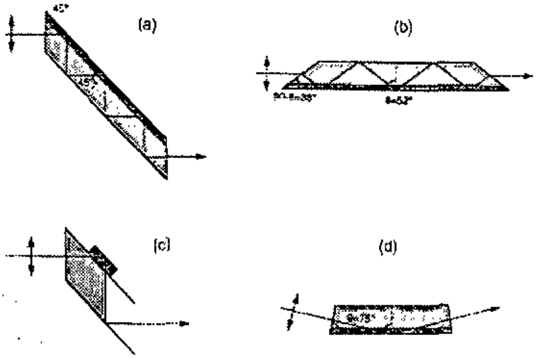

Figure 2.3: Multipass,(a) and (b) or two pass (c) and (d), waveguide geometries for intersubband absorption measurements (taken from [41]).

diffraction angle is real and the diffracted wave is a propagating wave (Fig.2.4 (b)). On the other hand if p is smaller than λ/n, the diffraction angle is imaginary and an evanescent surface wave is formed with a decay length δ (Fig. 2.4(a)). The coupling efficiency η defined as the ratio $(E_z)^2/E_0$ of the total energy density z-polarized wave E_z and the in-plane polarized incident wave E_0 is shown in figure 2.4. The simulation is performed for various metal filling factor f, or duty-cycle of the grating period (Fig. 2.4 (c)). It turns out that the coupling efficiency decreases rapidly for grating periods greater than the wavelength of light in the material (diffractive case) and increases for the evanescent regime. Surprisingly, the efficiency increases with the filling factor and eventually increases above unity due to wave build up. The optimal grating coupler period p can be determined by fixing the decay length

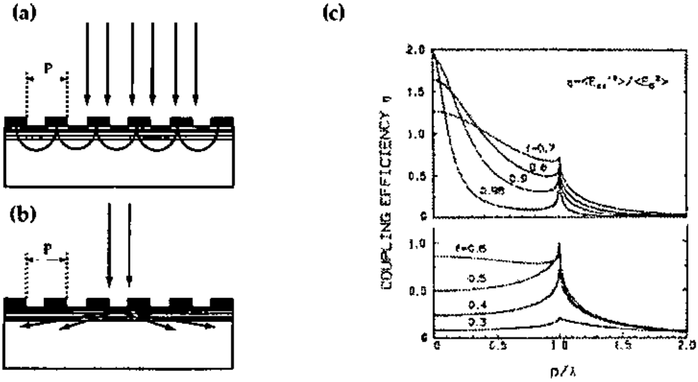

Figure 2.4: (a) The grating period p is smaller than the wavelength and (b) the grating period p is larger than the wavelength.(c) Coupling efficiency for various metal filling factors (taken from [41, 44]).

of the evanescent wave in relation 2.2.1 equal to the quantum cascade structure thickness.

$$(\frac{2n\pi}{\lambda})^2 = (\frac{2\pi}{p})^2 - \frac{1}{\delta^2} \tag{2.2.1}$$

Practically, the grating coupler can either be etched into the semi-conductor surface or deposited on top of the sample surface as a metallic grating. For the experiment, a photolithographic mask has been designed with grating periods of $15\mu m$, $10\mu m$ and $5\mu m$ with a 50% duty-cycle. The first step of the sample processing is to deposit the Ti/Au gratings on the surface of the sample. After providing the contacts on top of the gratings, the sample is etched to the substrate into mesa of sizes ranging from $900 \times 900\mu m^2$ down to $80 \times 80\mu m^2$. Practically, mesa of $450 \times 450\mu m^2$ are more commonly used as they match the optical focal point size of our optics. Figure 2.5 shows respectively a photograph (a) and a schematics

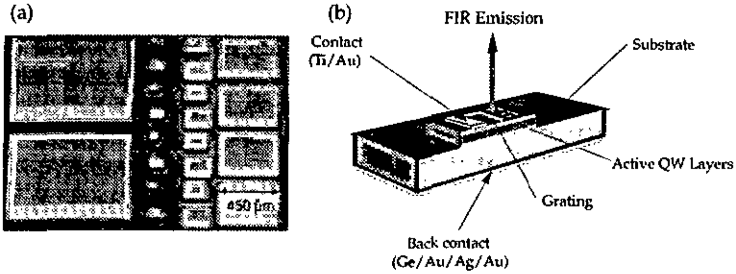

Figure 2.5: (a)Photograph of sample processed in the surface emission configuration with gratings deposited on top of the mesas. (b) Schematics of the processed sample with a mesa.

(b) of the finished processed sample for surface emission experiments.

2.3 Sample doping characterization

In a quantum cascade structure, the well and barrier thicknesses are determined in order to obtain a specific positioning of the electronic wavefunctions inside the structure. In order to obtain the desired electronic intersubband energy level configuration, it is crucial to have a homogenous and stable electric field across the structure and prevent space charge build up. The structure is therefore doped to compensate the donors positive charge and keep the structures overall electrical neutrality when biased.[22] However as the absorption of light in semiconductors due to free carriers increases like λ^{2-3}, this effect become increasingly important for far infrared radiation.[45] Low average doping is therefore required in the active region in order to reduces free carrier absorption. Average Si doping in the order $10^{15}cm^{-3}$ have been achieved in our samples. Such low dopings requires a clean growth system and

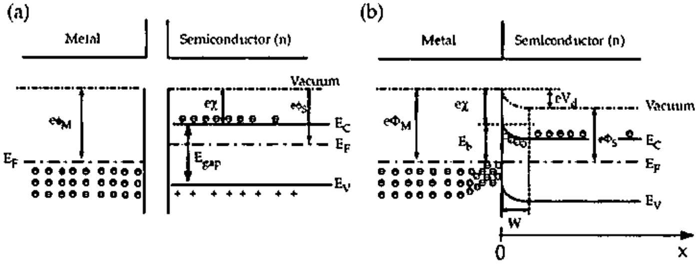

Figure 2.6: Band structure of (a) a metal and a n-doped semiconductor and (b) of a Schottky contact at thermodynamical equilibrium.

good doping control. It is therefore crucial to be able to characterize the samples after growth, specially when the samples do not behave electrically as expected. The average doping characterization of the samples are performed by capacitive measurements.[3] At the interface between a metal and a semiconductor, the Fermi level must be continuous across the junction and leads to a transfer of charges between the two materials. Depending on the work function $e\phi_M$ and $e\phi_s$ of the two materials, a *Schottky* junction may be formed. This arises when the metal extraction energy is greater than the electrical affinity of the semiconductor ($e\phi_M > e\chi$). In this case, the electrons cascade into the metal until the Fermi levels are equalized as shown in Fig. 2.6. The height of the barrier is defined by relation 2.3.2. [46]

$$E_b = e\phi_M - e\chi \tag{2.3.2}$$

The electron density being much smaller in the semi-conductor than in the metal, an important portion of the semiconductors volume becomes depleted of electrons when equilibrium is reached forming a depletion layer. By integrating the Poisson equation (relation 2.3.3) we can derive the value of the electric field at the interface between the materials (x=0) as a function of the doping N_d and of the depletion length W.

$$\int_x^W \frac{d^2V(x)}{dx^x}dx = -\int_x^W \frac{eN_d}{\epsilon_s}dx = -E(x) = -\frac{eN_d}{\epsilon_s}(x - W) \tag{2.3.3}$$

Integrating once more and setting $V_d = V(x = W) - V(x = 0)$ the difference of potential at the edges of the depletion layer allows to compute the depletion length as a function of the applied bias. This depletion width of a Schottky diode is given in relation 2.3.4.

$$W(V) = (\frac{2\epsilon_s V_d}{eN_d})^{1/2} \tag{2.3.4}$$

Applying of a positive bias on the metal, will increase the barrier potential to $V_d - V$. The depletion length and the space charge will increase accordingly creating a differential capacity given by relation 2.3.5.

$$C(V) = \frac{dQ}{dV} = (\frac{\epsilon_s eN_d}{2})^{1/2} \times \frac{1}{(V_d - V)^{1/2}} = \frac{\epsilon_s}{W} \tag{2.3.5}$$

The average doping density N_d as a function of the depletion length is then finally given by relation 2.3.6.

$$N_d(W) = \frac{2}{\epsilon_s e} \times \frac{dV}{d(1/C^2)} \tag{2.3.6}$$

The doping cannot be measured on the samples grown in the InGaAs material system

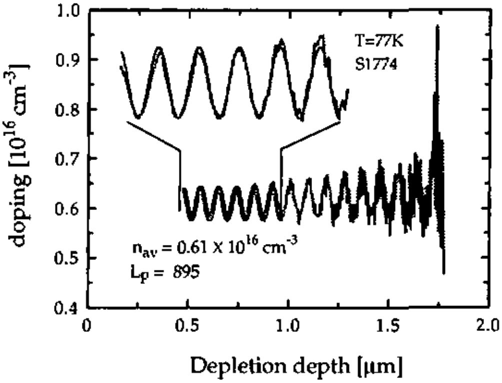

Figure 2.7: Typical result from a C-V measurement obtained for sample S1774.

as the Schottky barrier height on n-InGaAs is too low ($\phi_b \approx 0.2eV$).[47] However in the GaAs material system, the barrier hight is $\phi_b \approx 0.9eV$ allowing $C - V$ measurements to be performed.[48]

For the experiment, a small surface of the wafer is processed into mesas of various sizes ranging from $8.1 \times 10^{-3}cm^2$ to $1.4 \times 10^{-4}cm^2$. Before evaporation of the Ti/Au metallic contact, the highly doped top contacts are removed by wet etching to form the Schotty barrier. The samples are then soldered on sub-mounts and immerged in liquid nitrogen. The capacitance is measured with a HP4284A Precision LCR Meter with increasing applied DC bias with a fully automatized system using a Labview^{TM} environment. Typical doping profile is shown in Fig. 2.7 for sample S1774, described in details in the next chapter, where an average doping $0.61 \times 10^{16}cm^{-3}$ is measured. This value is very close to the expected doping of $0.42 \times 10^{16}cm^{-3}$. We clearly observe an oscillation of the doping due to the repeated

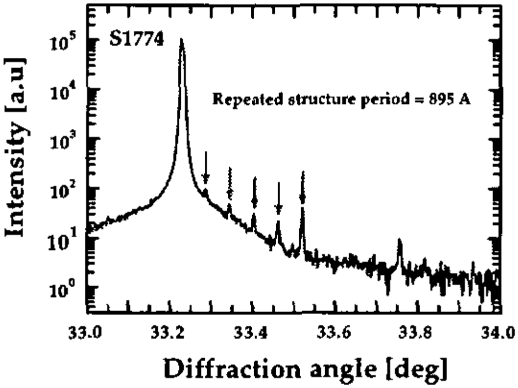

Figure 2.8: Typical X-ray diffraction spectra obtained for quantum cascade structure grown in the AlGaAs/GaAs material system. The regular repetition of the small peaks originates from the repetition of the quantum cascade structure (Courtesy of Dr. M. Beck, UNINE).

growth of the active region with the localized doped regions of the injector. The data has been fitted with a *sin* function on five periods with a period of 895Å. In this particular case, the obtained period value matches exactly the periodicity extracted from the X-ray diffraction data (Fig. 2.8).

2.4 Far-infrared detection

2.4.1 Introduction

In our experiment, the main difficulties from the detection aspect comes from the detector's spectral responsivity and its sensitivity. In the frame of this work, the spectral region is defined as the region where the photon energies are smaller than the optical phonon energy in the considered material ($\lambda > 35\mu m$). The expected emitted power of our structures can be estimated using relation 2.4.7 where the radiative lifetime τ_{rad} is computed using relation 2.4.8, z_{if} being the matrix element between the optical transition levels.[29, 49, 22, 11]. The non-radiative lifetime τ_{nr} is a key issue of this work and will be discussed in detail in chapter 4.

$$P = \eta_c \frac{\tau_{nr}}{\tau_{rad}} \hbar\omega N_p A \frac{J}{e} \tag{2.4.7}$$

$$\tau_{i \to f} = \frac{3\pi c^3 \hbar \epsilon}{e^2 \omega^3 n^3} \times \frac{1}{z_{if}^2} \tag{2.4.8}$$

Assuming $450\mu m \times 450\mu m$ emission surface with a collection efficiency at the detector of $\eta_c \approx 1 - 10\%$ (Fig. 2.4 (c)), a quantum efficiency of $\tau_{nr}/\tau_{rad} \approx 10^{-6}$, a number of periods of $N_p = 35$, a photon energy of $\hbar\omega = 20meV$ and a current density of $100Acm^{-2}$, the expected output power ranges between 15 and 150 pW. Specific detectors are therefore needed to detect such low light intensities and at such long wavelengths.

Two principal types of photo-detectors are commonly available : photoelectric detectors and thermal detectors. The photoelectric detectors use an optical transition between two sets of quantum states in a material that absorb the incoming photons by exciting electrons to

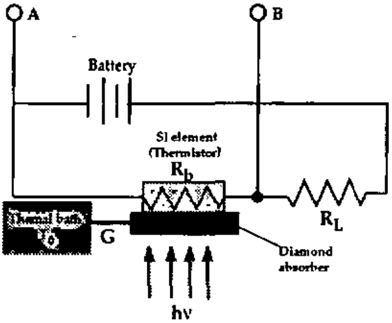

Figure 2.9: Diagram of a bolometer detector.

upper states. In general, such detectors have a fast recovery time ($<< 1\mu s$) but are however spectrally limited on the low energy side of the spectrum by their finite energy bandgap. The other type are the thermal detectors which convert directly the photon energy into thermal phonons in an absorber. Their sensitivity is therefore independent in the incoming photon energy but the recovery time is rather slow ($\approx ms$). An diagram of a bolometer is shown in Fig. 2.9. The incoming light is absorbed by a thin diamond absorber thermally connected to a thermal bath by a thermal conductance $G[W/K]$. The temperature of the absorber rises with the incident optical light until the power flowing onto the absorber equals the power flowing out into the thermal bath of temperature T_0. The temperature of the absorber is then measured with a very sensitive thermometer (thermistor) which in our case is a Si element. This element is connected to a battery through a load resistance R_L delivering a constant current. The temperature variations changes of the Si element induced by the absorber will change the resistance R_b changing the bias at terminals A and B. The electrical

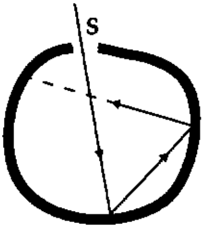

Figure 2.10: The surface S of the hole drilled in the box is a practical approximation of a black-body surface.

response $S[V/W]$ of the bolometer can be deduced by performing a load curve measurement. Description of this procedure is described in the bolometer documentation [50] and the theory of the thermal and electrical characteristics of bolometers is discussed in detail in ref. [51].

2.4.2 Bolometer Optical response

In the characterization processes of far-infrared emitting devices it is important to have an absolute measurement of the emission powers. As the responsivities given by the manufacturer (Infrared Laboratories) are obtained by measuring the electrical properties of the detector, absorption due to the filters and windows in front of the detector are not taken into account. Optical power calibration of our Si and Ge bolometers have been performed. For such measurements a home made black body source was used. Such a black body absorbs totally any radiation, independently of its frequency, which falls on its surface. In return, a body which strongly absorbs any radiation will re-emit the energy as thermal emission (*Kirchhoffs law*). The volumic spectral density of energy $u(\nu, T)$ is described by ***Planck's distribution law*** (Eq. 2.4.9) depends only on the equilibrium temperature T of the photon

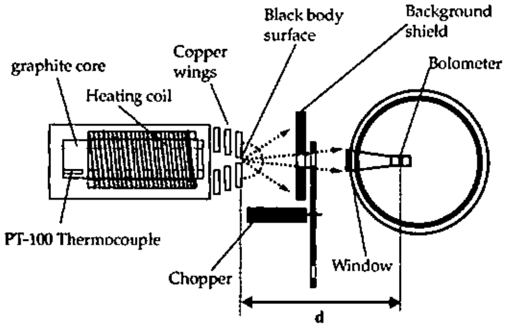

Figure 2.11: Set up used for the calibration of the bolometer.

bath inside the cavity.

$$u(\nu,T)=\frac{8\pi h\nu^3}{c^3}\frac{1}{e^{h\nu/kT}-1} \tag{2.4.9}$$

The total volumic power is obtained by integration of Eq. 2.4.9 over the whole spectrum. The thermal power emitted by an unitary surface is given by the *Stefan-Boltzmann law* (Eq. 2.4.10) where $\sigma = 5.67\times10^{-8}$ $[Wm^{-2}K^{-4}]$ is the Stephan-Boltzmann constant. [52] Knowledge of the temperature and the black body surface gives immediately the emission power.

$$P_{tot}=\frac{2\pi^5k^4}{15h^3c^2}T^4\times S_{bb}=\sigma T^4\times S_{bb} \tag{2.4.10}$$

Such a surface can be approximated by drilling a hole into box as shown in Fig. 2.10. Any radiation falling onto the hole, will be absorbed and has nearly no chance of getting out again after reflections and diffusions inside the box. The experimental set-up used to calibrate the bolometer responsivity is shown in Fig. 2.11. The hot source is made from a graphite cylinder in which a hole has been drilled, surrounded by a heating coil. Copper

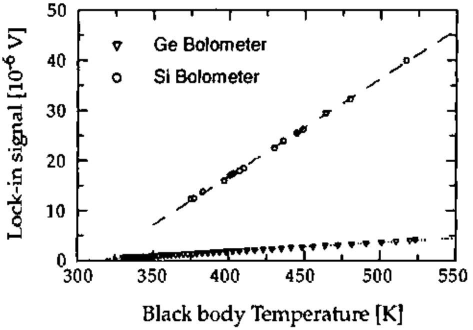

Figure 2.12: Lock-in signal is plotted versus black body temperature for both the Si and the Ge bolometer. Dashed lines are fits to the data.

plates and a thin aluminum foil separated by a few millimeters with different hole diameters are mounted in front of the hole. These plates act as heat shields in order to have the black-body surface surrounded by a cold background with an effective diameter of $2r_{bb} = 6mm$. The temperature of the black body is assumed to be equal to the temperature of the graphite cylinder measured with a PT-100 calibrated thermometer. The black body is placed at a distance d ($d_{Si} = 43cm, d_{Ge} = 51cm$) from the bolometer and its thermal emission is chopped with a mechanical chopper at the maximum response frequency of the bolometers ($\approx 400Hz$ for the Si bolometer and $47Hz$ for the Ge bolometer). Special care has been taken in order to chop only the black body aperture to prevent from detecting temperature changes of the "whole universe" placed behind the chopper. The chopper frequency is then used as reference frequency for the lock-in amplifier. The experimental data is shown in Fig. 2.12 where the bolometer signal is plotted versus black-body temperature. This measurement has been performed for both a Si and a Ge bolometer. The obtained signal is linear with temperature

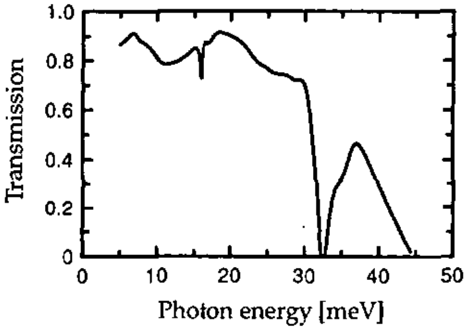

Figure 2.13: Transmission spectra of the low band-pass filter of the Si bolometer. Data provided by the manufacturer IRLabs.

down until the signal saturates, indicating that the temperature of the black body surface and the copper wings are the same. The observed decrease of the saturation temperature is due the presence of additionnal cooling wings when performing the measurements with the Ge bolometer. The total emitted power from the black body is calculated using Eq. 2.4.10. The power reaching the bolometer P_{eff} is proportional to a product of factors taking into account the various experimental proporties of the set-up. The spatial factor η_S introduces the dependence of the transmitted power on the distance r between the source and the detector and on the cosine of the angle θ between the direction of observation and the normal to the emitting surface (*Lambert's law*).[53, 52] Conservation of the emitted power requires $I_0 S_{bb} = I(\theta) S(r)$ to be satisfied, where I_0 is the surface density of power of the source, S_{bb} is the source surface. When the detector is in front of the emission source ($\theta = 0, r$) the power reaching it is proportional to $\eta_S = S_B/S_r$ where S_B is the bolometer surface and S_r is given by Eq. 2.4.13.

$$I_0 S_{bb} = I(\theta)\ S(r) \tag{2.4.11}$$

$$= I_0\ cos\theta\ 2\pi r^2 \int_0^{\pi/2} sin\theta\, d\theta \tag{2.4.12}$$

$$= I_0\ \pi r^2 \tag{2.4.13}$$

Formally, the spectral response of the bolometer is not bounded. However, a low-pass filter with a cut-off frequency at 350 cm^{-1} for the Si bolometer is added to decrease the noise. The η_ω factor gives the ratio of the incoming power which gets through the low-pass filter. This factor is determined manually by integrating the convolution of the spectral response curve (Fig. 2.13) with the theoretical Plank curve between 0 and 350cm^{-1} for each temperature. The chopper placed in front of the source is acting as a grating removing half of the emitted power. The power finally reaching the Si bolometer chip is given by relation 2.4.14 where $S_{bb} = \pi r_{bb}^2$.

$$P_{eff} = 0.5 \times S_{bb} \times \sigma \times T^4 \times \eta_S \times \eta_\omega \tag{2.4.14}$$

The optical response curves for both the Si and the Ge bolometer are shown in Fig. 2.14 (a) and are summarized in Table 2.1. The Si bolometer has a response value of 17750 [V/W] which leads to a responsivity about a factor of 15 lower than the electrical calibration value. Noise measurements have been performed by closing a shutter in front of the bolometer window. The value given in $V/\sqrt{Hz}$ by the lock-in amplifier is converted to Noise Equivalent Power (NEP) with the experimental optical responsivity.

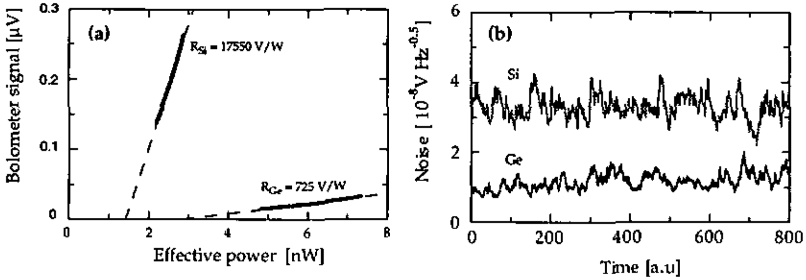

Figure 2.14: (a) Optical response curves for both the Si and Ge bolometer. (b) Noise measurements data.

2.5 Spectral measurements

For far-infrared spectral emission measurements either a Fourier transform infrared (FTIR) spectrometer or a magnetically tuned InSb filter [14], can be used. A variant of the latter, an InSb-cyclotron resonance detector is also possible.[54] The main advantage of the FTIR is its high resolution capabilities as it consists of a *Michelson-Morley* interferometer where the resolution is given by the optical path length difference between two interfering light beams. The magnetically tuned InSb detector, has the disadvantage of having an intrinsic broad linewidth given by the Landau levels scattering times and impurity scattering ($\Delta\nu = 1.1 - 3.4 meV$[54] and §5.4). However a very short optical path free of any beam splitter or mirrors between the sample and the detector is possible. The optical path length is also free of air absorption and of any 300K black body radiation as as the whole system is submerged in liquid helium. Helium bubbles may however appear when the samples are driven at high

Table 2.1: Parameters for both the Si and Ge bolometer. The electrical responsivities are given by the manufacturer.

	Electrical resp. $[VW^{-1}]$	Electrical NEP $[pW/\sqrt{Hz}]$	Optical resp. $[VW^{-1}]$	Optical noise $[10^{-8}V\sqrt{Hz}]$	Optical NEP $[pW/\sqrt{Hz}]$
Ge	1.67×10^4	0.85	0.725×10^3	1.17	16.1
Si	2.69×10^5	0.115	1.775×10^4	3.23	1.8

currents. An InSb system has punctually been used and is described in §5.4.

Two different FTIR spectrometer set-up are used. The first set-up is built around a commercial Nicolet 800 Fourier transform spectrometer (Fig. 2.15 (a)). No lenses are used in the optical path for light guiding. Instead, plane mirrors and parabolic off-axis mirrors are used preventing high material absorption at far-infrared wavelengths. The samples are soldered on a copper mount and are electrically connected to two gold pads by gold wire bonding. The copper mounts are then mounted on the cold finger of a He flow Janis JT-100 cryostat with a maximum testing capacity of two samples. Far-infrared transparent polyethylene windows are used to isolate the cryostat vacuum from atmospheric pressure. The electrical power is provided by a HP-8114A pulse generator. The injected current is measured using a Model 711 calibrated current probe by ALS. The probe is an electrical transformer placed around the injection current line. The current and the bias on the device are measured by a LeCroy 9384L digital 16Mhz oscilloscope. The far-infrared emission was amplified by a EG&G 7260 DSP lock-in amplifier synchronized with the pulse generator. The

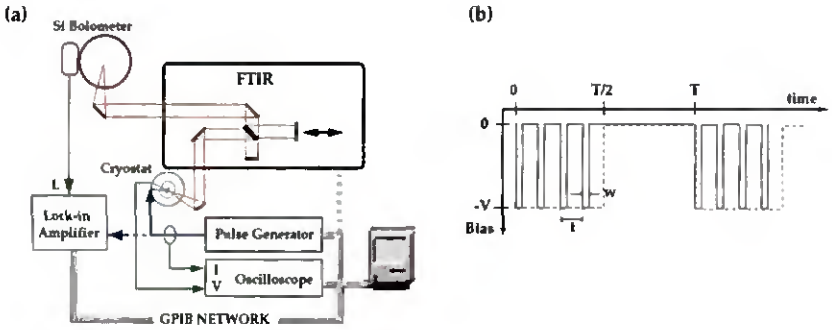

Figure 2.15: (a) Experimental setup used for far-infrared light emission experiments.(b) Due to the low response time of the bolometer, the injected current is modulated at the maximum response time of the detector with macro pulses (dashed line). Micro-pulses instead of DC current are filling the macro pulses to minimize sample heating.

whole experiment is driven via a GPIB network by a computer. Due to the slow response time of the bolometer, the injected current is modulated into low frequency macro pulses with a repetition rate of 1/T = 413 Hz matching the bolometers maximum recovery time. To prevent as much as possible device heating, trains of 627 micro-pulses with a repetition rate of $1/t = 520kHz$ are produced during the macro-pulse durations (Fig. 2.15(b)). The maximum possible overall duty factor is 50%. It can be reduced by changing the micro-pulse duration w or by reducing the number of pulses and their repetition rate. The light coming out from the sample is collected by a gold coated off-axis parabolic mirror with 60 degree collection aperture. The collimated light beam is then sent through the Fourier transform infrared spectrometer used with a standard Si solid state beam splitter. Leaving the FTIR, the light is collected with a 90 degrees aluminum parabolic off-axis mirror and sent on the liquid-helium cooled Si Bolometer detector operated at 4.2K. The entire optical

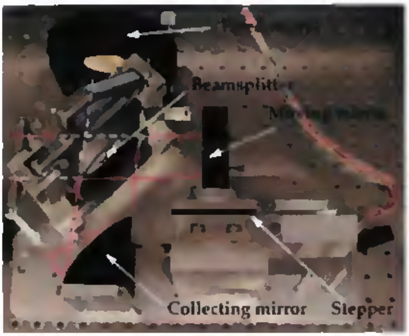

Figure 2.16: Photograph of the interferometer board where the Far-infrared Nicolet beamsplitter is used. The board is then inserted in the vacuum chamber.

path is purged with dry air with a 20 to 30% decrease of the water vapor absorption. Due to the very low intensities of the FIR signal, spectral measurements of the luminescence are performed using the FTIR in the step-scan mode. In contrast to the rapid scan mode, where the mirror is continously traveling back and forth, the step scan mode allows the signal to be detected with a lock-in amplifier. The mirror moves step by step with a waiting period equal to the the lock-in integration time. The measurement parameters is a trade-off between the signal to noise ratio and the resolution. Integration times up to 2 seconds per points at a resolution of 0.12 meV between adjacent spectral points, requires more than an hour of measurement time. Light versus current ($L-I$) properties of the device are performed with FTIR mirror left free.

The measurement efficiency is increased with the second set-up consisting of a vacuum FTIR. Is has been designed and built by our mechanical workshop. In contrast to the Nicolet 800 system which uses a linear motor with a HeNe laser fringe counter to monitor de position of the moving mirror, our system uses by a stepper motor, the position being monitored by counting the steps. The stepper motor model ESP-300 supplied by Newport can move over a length of 25mm with a maximum step displacement of $0.075\mu m$. A photograph of interferometer is shown in Fig. 2.16. The light from the sample is collected by 90^0 off-axis 2 inches gold coated mirror and sent onto the beam splitter. The system is designed either to accept a beam splitter originally used on a Nicolet 860 spectrometer (as shown in Fig.2.16) or a low doped, double sided polished silicon wafer specially cut for this application. The used wafer is $200\mu m$ thick, limiting the light absorption, but unfortunately also limiting the resolution of the spectrometer due to the Fabry-Perot interferences. As a beam-splitter is a three medium system for an incoming wave (vacuum $= 1 \rightarrow$ dielectric $= 2 \rightarrow$ vacuum $= 3$), the interfaces dielectric $\leftrightarrow$ vacuum create mirrors with a transmittance and a reflectance. The transmission through a Fabry-Perot cavity depends on the incident light wavelength and either constructive or destructive interferences build up between the incident and reflected light. The separation between the maxima or mode separation, is given by Eq. 2.5.15 where c is the speed of light in vacuum, n_{op} the refractive index of the dielectric and L_{cav} the length of the cavity.

$$\Delta\nu = \frac{c}{2n_{op}L_{cav}} \tag{2.5.15}$$

For a $200\mu m$ silicon (n=3.4) beam-splitter, the mode separation is $\Delta\nu \approx 7.4cm^{-1}(0.9meV)$, limiting the resolution to this value. The spectrometer is mounted inside a vacuum chamber and the sample is placed at the collecting mirror s focal point positioned by the outside with a x-y-z manipulator. The bolometer is connected to the side of the vacuum chamber.

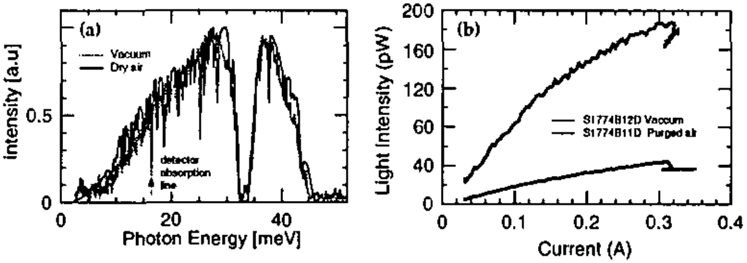

Figure 2.17: (a) Background emission spectra measured in a dry-air purged optical path and in vacuum. (b)Comparison of the detected far-infrared emission from the vacuum FTIR and the Nicolet 800 set-up.

The whole light path, from the sample to the detector is under vacuum. However, the beam has to go through a polyethylene window, separating the bolometer vacuum from the spectrometer chamber. This is necessary as no airlock is mounted in between and allows to change sample without heating up the bolometer. A dedicated LabView program fully controls the stepper motor together with the sample power injection and light detection allowing fully automated multiple runs of spectral measurements. Figure 2.17 (a) shows a background emission spectra performed in dry air and in vacuum. In dry air, we clearly observe important absorption lines which are absent from the spectra performed in vacuum, with the exception of a line at 16.4 meV. This absorption lines originates from the low-pass filter of the bolometer. Quantitative measurements are shown in Fig. 2.17 (b). The light intensity is plotted versus injected current for both the vacuum FTIR and the Nicolet 800 dry-air systems. A factor of four in the detected light intensity has been obtained with the vacuum FTIR system. Typical interferogram obtained with this set-up is shown in figure 2.18. The interferogram was performed with N=2048 points, $\Delta D = 2\mu m$ long

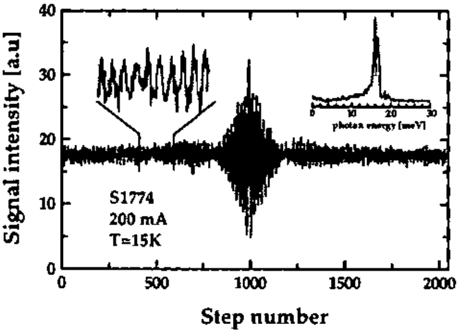

Figure 2.18: Typical interferogram obtained with the vacuum FTIR with a spectral resolution of $1.22cm^{-1}$ (0.15 meV). The resulting spectra is shown in the right inset.We clearly observe the absorption of the filter in the center of the peak. As the interferogram is still oscillating at the end of the fixed stepper traveling distance, the peak is not fully resolved.

steps. The length of the steps ΔD sets the high energy bound of the measured spectra. This energy can be calculated by the applying the *Nyquist theorem* stipulating that the maximum resolution in the frequency domain is half the sampling frequency. In our case, taking into account that the light travels twice the mirrors distance, the high energy limit is set to 155 meV, clearly outside the bolometers detection range (43 meV). As the resolution of a Fourier transform interferometer is equal to the inverse of the length D of the maximum optical path length, it can be written as given in relation 2.5.16.

$$R = \frac{1}{D} = \frac{1}{2 \times N \times \Delta D} \tag{2.5.16}$$

Finally, the spectral resolution is $1.22cm^{-1}$ (0.15 meV) eventually limited by the beam splitter thickness.

Chapter 3

First Generation Far-infrared Active Structures

3.1 Introduction

High performance, long-wavelength, room temperature operating quantum cascade lasers up to photon wavelengths slightly smaller than $\lambda = 34\mu m$ should be possible with standard mid-infrared QC technology. The main reason to the success of the quantum cascade laser in the mid-infrared is to have designed structures with an injection region, allowing high injection efficiency into the excited state of the optical transition conjugated with a very fast carrier extraction rate out of the active region. The latter is provided by having the transition energy ΔE_{21} (Fig. 1.4) resonant with at least one optical phonon emission energy E_{ph} with sub-picosecond lifetime $\tau_{ph} \approx 0.8-0.25ps$ [55, 38, 22, 56]. In the far-infrared the optical transition energy is smaller than the optical phonon energy changing in a considerable manner the

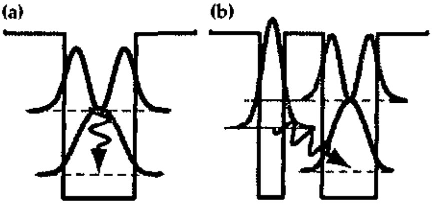

Figure 3.1: Schematic energy band diagram of a vertical transition (a) and a diagonal optical transition (b).

physics of the dynamics of the structure compared to the mid-infrared. Designs having an optical phonon extraction are difficult to achieve as their emission may simultaneously depopulate the ground state and the excited state. Simple transposition of mid-infrared structures to the far-infrared is therefore not straight forward.

In this chapter far-infrared electro-luminescence from a vertical and a diagonal quantum cascade structure is demonstrated. As shown in Fig. 3.1(a), the vertical transition occurs between electronic states that spatially overlap in the same quantum well. In contrast the diagonal transition (b), or photon assisted tunneling transition occurs between states which are spatially separated in two different quantum wells. High quality interfaces are necessary as monolayer fluctuations in the active well have relatively greater influence in the far-infrared than in the mid-infrared. In a vertical transition the effects due to interface roughness are significantly reduced compared to the diagonal transition where the transition occurs through two interfaces. The diagonal transition however, has the great advantage that the non-radiative rate of the excited state is controlled by the injection barrier thickness separating the excited state from the ground state. Population inversion between these states is therefore expected to be easier to achieve with the appropriate choice of the barrier thickness. For a vertical transition, the population inversion is controlled by the extraction processes of the ground state which is more difficult to design. The structure design are done by simulation of the energy band structures where the electronic states of the heterostructure are computed by solving the one-dimensional Schroedinger equation in the envelope function approximation. The non-parabolicity of the dispersion curves is included in the simulation algorithm through an energy dependent effective-mass.[22]

3.2 Vertical transition structure

3.2.1 Structure Design

One period of our structure design consists of four GaAs quantum wells separated by thin $Al_{0.15}Ga_{0.85}As$ tunnel barriers. As in mid-infrared quantum cascade structures, each period consists of an un-doped active region, in which the spontaneous emission occurs, and an injector where the carrier can energetically relax and funnel into the next active region.[57] The active region consists of a 28nm GaAs quantum well coupled through a 2.5nm $Al_{0.15}Ga_{0.85}$ barrier to a 18nm GaAs well. A 40nm extraction barrier separates the injection/relaxation zone from the active zone. Its consists of a 16nm and 15.5nm GaAs well separated by a 2.5 nm AlGaAs barrier. The injection barrier is 60nm thick. The emission occurs in the 28nm well through a vertical transition with a computed energy of $\Delta E_{21} = 15.3meV$ between states n=2 and n=1. The dipole matrix element between these two states, computed using

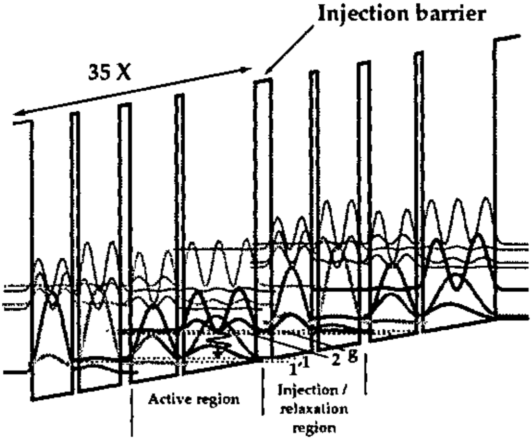

Figure 3.2: Energy band structure for sample S1353 in the GaAs/AlGaAs material system computed with the corrected layer thicknesses obtained from the X-ray diffraction data (+5.6%). The layer sequence, starting from the injection barrier is **6.0**/28/**2.5**/18/**4.0**/16/**2.5**/15.5 where $Al_{0.15}Ga_{0.85}As$ layers are in bold, $GaAs$ in Roman and underlined numbers correspond to doped region.

relation 3.2.1 is $z_{21} = 5.3nm$. The energy band structure is shown in Fig. 3.2.

$$z_{if}^2 = |\langle\Psi_i|Z|\Psi_f\rangle|^2 \tag{3.2.1}$$

The ground state g of the injector is in resonance with excited state of the transition of the next period. The total thickness of one period is $92.5nm$. A similar structure has been designed in the InGaAs/AlInGaAs material system with the structure thicknesses given in caption of Fig. 3.3.

Two wafers (S1353 and S1774) of the GaAs structure have been grown but with different nominal doping values. A long time separation is however separating these growths

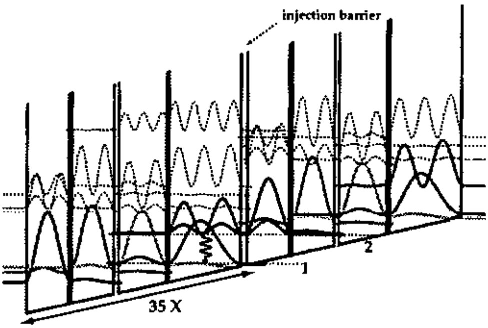

Figure 3.3: Energy band structure for sample S1431 in the InGaAs/AlInAs material system computed with the obtained with the corrected layer thicknesses (-1.5%). The layer sequence, starting from the injection barrier is **3.4**/38/**1.4**/25.5/**2.3**/22.5/**1.4**/22.3 where $In_{0.52}Al_{0.48}As$ layers are in bold, $In_{0.53}Ga_{0.47}As$ in Roman and underlined numbers correspond to the doped region ($Si, 5 \times 10^{15} cm^{-3}$) corresponding to an average doping of $9.6 \times 10^{15} cm^{-3}$.

(S1353:1997 and S1774:1999) and growth conditions are therefore not identical as the background doping and growth rates may differ leading to slightly different structures. Structure S1353 is grown on an n-doped ($1 - 2 \times 10^{18} cm^{-3}$) GaAs substrate. A bottom GaAs contact layer and a buffer layer are grown, respectively $200nm$ and $1000nm$ thick. Their nominal doping are respectively 2×10^{18} and $8 \times 10^{15} cm^{-3}$. The quantum cascade structure follows with a 35 times repetition of the elementary cell. The first well of the injector is nominally doped with Si at $n = 8 \times 10^{15} cm^{-3}$ leading to a nominal average doping of $n_{av} = 1.4 \times 10^{15} cm^{-3}$. Mid-infrared data have demonstrated that it is fundamental not to dope the active region to obtain narrow intersubband transitions.[57] Compared to mid-infrared structures ($n \approx 1.5 \times 10^{17} cm^{-3}$ [22]) the structure is very low doped. Such low doping is chosen to limit the current and thus the sample heating and to prevent important

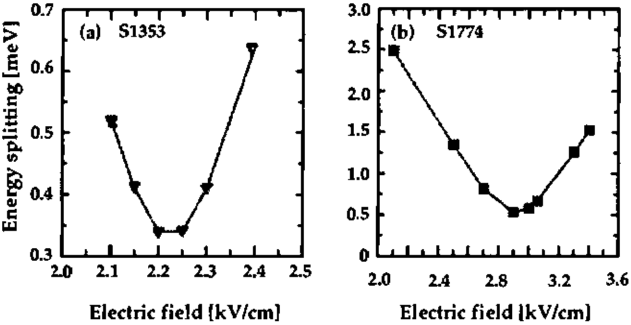

Figure 3.4: Calculated splitting energy between the excited state of the optical transition and the injector with increasing applied electric field for sample (a) S1353 and (b) S1774.

free carrier absorption from the generated photons. On the top of the structure two contact layers are grown respectively a $200nm$ GaAs thick layer nominally doped at $n = 8\times10^{15}cm^{-3}$ and a $30nm(In)GaAs, n = 2 \times 10^{18}cm^{-3}$ highly doped layer finishes the growth. The addition of indium allows to obtain non alloyed Ti/Au ohmic contacts. This highly doped layer is rather thin to reduce free carrier absorption as this structure is processed with a top grating to extract the light from the surface.

X-ray diffraction of the structures have been made on all samples and C-V measurement on the GaAs ones. Sample S1353 is longer than expected (+5.6%) which has the effect to increase the wavelength of the intersubband emission. The measured average doping is a factor 2.1 higher than expected at $n_{av} = 3.0 \times 10^{15}cm^{-3}$. Sample S1774 is however shorter (−3%) and the average doping higher by a factor of nearly 1.5 ($n_{av} = 6.2 \times 10^{15}cm^{-3}$). The calculated structure for sample S1353 with the X-ray diffraction thicknesses is shown in figure 3.2. The InGaAs structure (S1431) is 1.4% shorter than designed. The energy band

Table 3.1: Designed and measured values obtained for vertical transition electroluminescence samples. The recalculated structure used the experimental values of the structure period.

	Period [nm]	n_{av} [$10^{15}cm^{-3}$]	n_s [$10^{10}cm^{-2}$]	Electric Field [kV/cm]	z_{if} [nm]	ΔE [meV]
S1353 (GaAs)	92.5	1.4	1.3	2.7	5.3	15.3
Measured	97.7	3.0	2.9	2.3-3.5	-	14.1
Recalculated	+5.6%	-	-	2.2	4.0	13.9
S1774 (GaAs)		4.2	3.9			
Measured	89.5	6.2	5.5	2.0-4.5	-	16.7
Recalculated	-3%	-	-	3.0	5.3	16.1
S1431 (InGaAs)	116.8	9.6	11.2	2.1	5.7	15.1
Measured	115.1	-	-	1.9	-	15.2
Recalculated	-1.4%		-	2.2	5.8	15.5

structure with the measured thicknesses is given in figure 3.3. The doping however could not be measured with the available technique. The designed and experimental values for vertical luminescence structures are summarized in table 3.1. The devices operating electric field is reached when the energy separation between the ground state of the injector (g) and the energy of excited state of the optical transition (2) has reached a minima. Variation of this energy difference with applied electric field is shown in Fig. 3.4 for samples S1353 and S1774. The calculated operating electric fields are respectively $F = 2.2kVcm^{-1}$ and $F = 3.0kVcm^{-1}$ for sample S1353 and S1774.

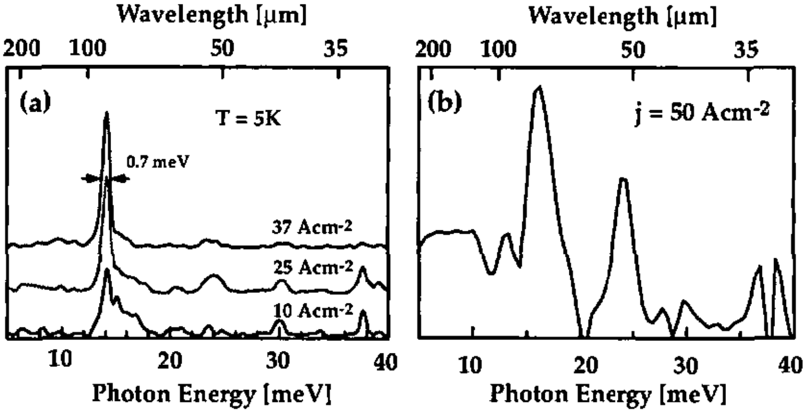

Figure 3.5: (a) Optical spectrum of the emitted radiation for various injected current densities. (b) Optical spectrum of the emitted radiation for an injected current density above the region of negative differential region (NDR).

3.2.2 Experimental results

Representative spectra from sample S1353 taken for increasing injected currents at T=5K are displayed in Figure 3.5. They show that the luminescence spectrum mainly consists of one narrow peak centered at a the photon energy of 14.1meV ($\lambda \approx 88\mu m$). At low injection current density ($j = 10Acm^{-2}$) we observe a small peak on top of a background. As the current density is increased this peak increases in intensity and eventually saturates at an injected current density of $j = 40Acm^{-2}$. Increasing further the current density leads to a broad emission as shown in Fig. 3.5 (b). No Stark shift is observed as expected from a vertical intersubband transition. The peak is easily identified to correspond to the n=2 to n=1 transition in the 28nm well, since its measured photon energy of $h\nu = 14.1meV$ corresponds well to the recalculated value of the n=2 to n=1 transition of $h\nu = 13.9meV$

using the thickness measured by X-ray diffraction (see table 3.1). Working with a spacing of 0.12meV between adjacent points, the Nicolet 800 FTIR allows us to spectrally resolve the luminescence peak and we measure a full width at half maximum (FWHM) of 0.7meV. This luminescence linewidth is much narrower than reported mid-infrared luminescence line widths (14-50 meV).[23, 39, 22] This very narrow linewidth suggest very clean interfaces between the AlGaAs and the GaAs layers as broadening of the luminescence is usually attributed to monolayer fluctuations in the active well.[23] At $j = 10Acm^{-2}$, a small peak appears on the high-energy side of the main luminescence peak. This feature at 15.1meV, present on all the spectra measured at this current, is identified as the transition from the n=2 state to the n=1' ground state of the adjacent well. The calculated splitting between the state n=1 and n=1' is 1.2 meV, and corresponds approximately to the measured separation between this broad feature and the luminescence peak (0.9meV). The high energy shoulder decreases with increasing current, and essentially vanishes at $j = 37Acm^{-2}$. This is expected because the n=2 to n=1' optical matrix element decreases abruptly with increasing applied electric field as the states n=1 and n=1' anti-cross. Simultaneous measurements of the voltage and optical output power versus injection current performed on the same device are reported for temperatures of T = 5K and T=80K (Fig. 3.6). In contrast to measurements performed on mid-infrared devices the luminescence efficiency is not constant with current injection.[23, 58, 39] At T=5K, the optical power rises sub-linearly up to a current of J=80mA ($j \approx 40Acm^{-2}$) with an output power of 10.6pW (Fig. 3.6(a)). This point corresponds very well with the observed breakdown of the voltage where it abruptly increases with no further increase of the current (Fig. 3.6(b)). At T=80K, the $L - I$ characteris-

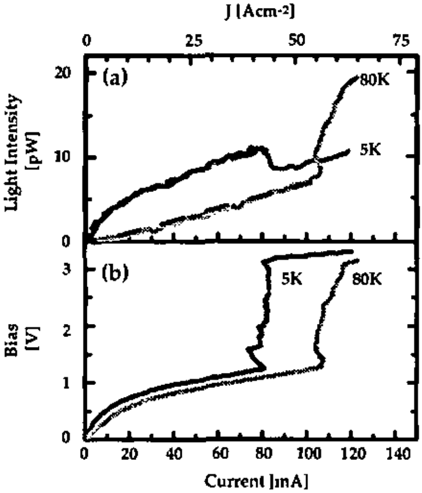

Figure 3.6: Upper figure shows the luminescence intensity versus injected current at T=5K and T=80K. The curve is fitted by a straight line at T=80K and by a square root relation at T=5K (dashed lines). Lower figure shows the bias versus injected current at the same temperature, as indicated.

tic is more linear, with a lower efficiency and an output power of 7.6pW at J=100mA. At higher current the output power increases dramatically. Spectral measurements show that the abrupt change in optical power above J=80mA (for T=5K) and J=100mA (for T=80K) correlated with the abrupt increase of the applied voltage arises when the ground state g of the injector is not anymore resonant with the upper state n=2 of the optical transition and a Negative Differential Resistance (NDR) occur.[16, 59] The optical spectrum in the region of negative differential resistance is extremely broad ($> 30meV$) and features many additional peaks (Fig. 3.5(b)). The spectrum is consistent with a broad injection in many energy levels from electron population with a broad energy distribution. This very good correlation between the electrical and spectral characteristics in the same device is a proof that the electro-luminescence arises from a resonant tunneling injection into the n=2 state and not from a heating of the electron gas. The spectrum of Fig. 3.5 exhibits some additional small features at 24, 30 and 38 meV. The lack of clear current dependence prevents unambiguous assignment to be done. However, the emission at 38meV is believed to be a plasmon mode excited by the polar GaAs optical phonons coupled by the grating through the surface. This peak vanishes for edge emitting devices (ref. Chap. 5).

The shape of the optical output power versus injection current characteristic provides some insight into the scattering mechanism. As it has been shown in previous measurements of the electron lifetime in quantum wells, the non-radiative scattering at T=80K is dominated by optical phonon scattering by electrons with a thermal energy allowing the emission of optical phonons.[60] Indeed, at this temperature, we observe a fairly linear relationship between emitted power and injected current indicating a scattering process with a constant lifetime (Fig. 3.6(a)). However, at T=5K, in the limit of low injection current to prevent significant electron heating, emission of optical phonon is forbidden. It has been shown both theoretically and experimentally that for electron sheet densities higher that $\approx 10^8 cm^{-2}$, electron-electron scattering is an efficient scattering mechanism. *Hyldgaard* and *Wilkins* gave a simplified expression for the electron scattering rate, showing that it is in good approximation proportional to the electron density of the excited sub-band of the transition (chapter 4).[61] Therefore the electronic population, and thus the optical power has a square root dependence with injected current. As shown by the fit on the data at T=5K of Fig. 3.6(a), this is very well observed in our data. This suggests that the main non-radiative

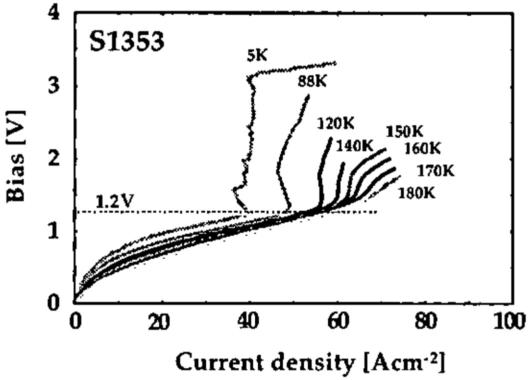

Figure 3.7: Voltage versus current measurements are shown with increasing temperature. We observe that the NDR breakdown occurs at a voltage of 1.2 volts independently from the lattice temperature. On the other hand the current at the breakdown increases with the temperature.

and limitative process in this structure comes from electron-electron scattering in the excited state.

Voltage versus current measurements have been done with increasing lattice temperature (Fig. 3.7). We observe that the NDR breakdown occurs at a nearly constant voltage of 1.2 volts independently from the lattice temperature. But on the other hand the current at the breakdown increases with the temperature. The increase of the current at constant bias can be understood with the existence of a temperature activated leak. At T=5K, and in the low injection approximation to prevent electron heating, the activated carrier population through this channel is marginal.[62] As the temperature is increased, the electrons acquire excess kinetic energy and eventually escape through this channel creating a leakage current. The temperature dependant current can be expressed as the sum of the current at low temperature and of the leakage current $J(T) = J_{5K} + J_L(T)$. Considering an energy level with a population n_0, the number of activated electrons is given by the *Boltzmann* distribution relation 3.2.2 where ΔE is the activation energy, T the lattice temperature, $k = 8.619 \times 10^{-2} [meVK^{-1}]$ *Boltzmann*'s constant, and g the ratio of the energy level degeneracy. .

$$n_L(T) = n_0 \times g \times exp(\frac{-\Delta E}{kT}) \tag{3.2.2}$$

The effective carrier escape rate w_{eff} from level E_2 is the sum of the non-radiative rate w_{5K} at low temperature and the temperature dependant $w_L(T)$ leakage rate. The increase of the leakage current can be expressed by $J_L(T) = qw_Ln_L(T)$. The total current increase with temperature can then be expressed by the ratio $J_L(T)/J_{5K}$ given by relation 3.2.3.

$$\frac{J_L(T)}{J_{5K}} = 1 + \frac{w_L}{w_0} g \times exp(\frac{-\Delta E}{kT}) = 1 + C \times exp(\frac{-\Delta E}{kT}) \tag{3.2.3}$$

A plot of the current density at the NDR with increasing temperature ratioed over the current density at T=5K is very well fitted by using relation 3.2.3 (plain line, Fig. 3.8). The fit gives an activation energy of $\Delta E = 18 \pm 2meV$ consistent with the activation of optical phonons from hot carrier to state n=1 of the optical transition: of the structre of Fig. 3.2 ($\Delta E_{activation} = h\omega_{LO} - \Delta E_{21} = 22meV$). An analysis based on the intensity of the luminescence versus temperature at constant current injection show that the emission of activated optical phonons explains well the decrease of the luminescence intensity with temperature (chapter 4).

The electrical properties of sample S1353, S1774 and S1431 are presented in Fig. 3.9(a).

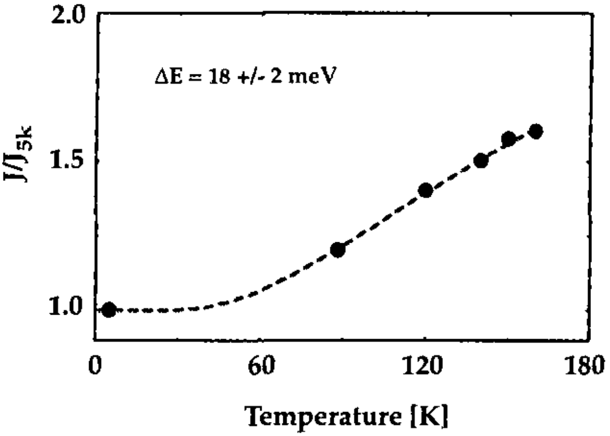

Figure 3.8: The ratio between the NDR current at T=5K and the current for increasing temperature is shown. The plain curve is a two parameter fit to the data using relation 3.2.3.

The maximum currents before the NDR are respectively $40Acm^{-2}$ at 1.2V, $156Acm^{2}$ at $1.4V$ and $33Acm^{-2}$ at $0.78V$. We observe that the bias at the NDR is close to constant for similar structures independently from the sample doping. The higher bias at the maximum current injection observed for sample S1774 compared to sample S1353 is consistent with a shorter structure period (- 8.6%). The maximum current density before appearance of the NDR is plotted versus sample average doping n_{av} multiplied by $exp(-\kappa L_B)$ which is proportional to T_B the tunneling probability for vertical samples used in this work (Fig. 3.9(b)). A linear dependency of the maximum injected current before the NDR with device doping is observed. This shows that the injected current can be increased by increasing the sample doping. This current increase is however not due to sample heating with higher injected

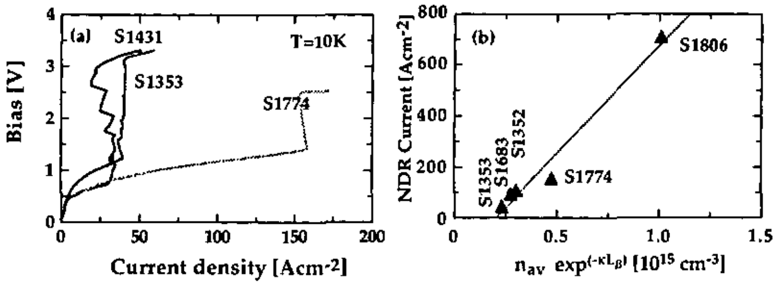

Figure 3.9: (a) Bias versus injected current density are shown for samples S1353,S1431 and S1774. (b) NDR current density versus average doping multiplied by a factor proportional to the carrier tunnel transmission probabilty through the barrier for vertical transition samples ($T \sim exp(-\kappa L_B)$). Computed values of $exp(-\kappa L_B)$ for samples S1353, S1353 and S1774 is $T_B = 0.077$, for S1683 $T_B = 0.098$ and S1806 $T_B = 0.137$.

current as $L - I$ measurements show similar square-root dependence of the light intensity with injected current as observed on sample S1353 (Fig. 4.3). Furthermore, the maximum output power has been increased from $10.6pW$ up to $44pW$ for sample S1774. Spectral measurements performed at the maximum injected current density is shown in Fig. 3.10 and show a peak centered at a photon energy of $h\nu = 16.7meV$. For comparison with the other samples the spectra are normalized in intensity with results obtained from the emitted light power versus current measurements. As the obtained power is the integrated power over the spectral window of the detector, the spectra have been normalized with the integrated surface under the curves equal to the measured light power. This is necessary as the spectrum contains emission that does not originate from the intersubband transition but from black-body emission. We observe that the maximum spectral power of samples S1353 and S1431 are very similar. The FWHM of the InGaAs luminescence peak is 36% broader

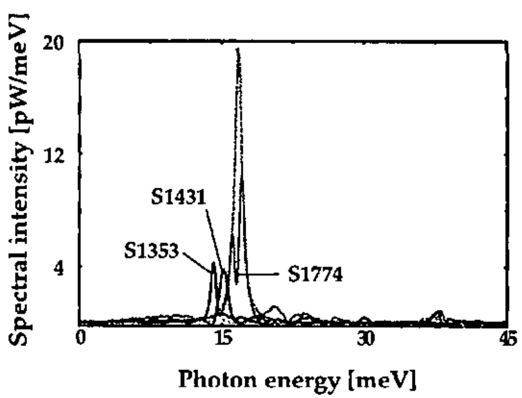

Figure 3.10: Spectral measurements performed at the maximum current density before appearance of the NDR for samples S1353,S1431 and S1774. Measurements have been performed in a dry-air environment. The output power versus injected current density for these samples are shown in figure 4.3.

($1.1meV$) than the GaAs samples. Our measured line widths are however much narrower than those reported from mid-infrared QC diodes luminescence.[57, 63] However they are in agreement with absorption measurements done on quantum wells in the mid-infrared showing a decrease of the intersubband absorption linewidth with an increase of the well width.[64] But, the same study has shown that the FWHM is relatively insensitive ($\approx$ 10%) to the alloy composition, at least for small percentages ($x \approx 10\%$). Due to high concentrations used in our case (>50%), alloy composition could still contribute to the observed linewidth broadening of the (Al)GaInAs luminescence peak compared to the (Al)GaAs sample luminescence peak. The emission spectra of sample S1774 exhibits a double peak due to the absorption line from the detector at 16.4meV and in reality only one peak is present. A fit to the data with a Lorentzian curve show that the maximum occurs a 16.7meV with a FWHM of 0.87meV, very

Table 3.2: The photon flux from the intersubband transition are calculated to compare the output power from the samples. The ratio of the photon flux to the average electron flux is a figure of merit describing the samples ability to convert electrons to photons. Note however that this value is not the quantum efficiency as the collection efficiency is not included in η.

	P_{exp} [pW]	FWHM [meV]	$h\nu$ [meV]	Photon flux [$10^{9}s^{-1}$]	Electron flux [$10^{17}s^{-1}$]	η [10^{-8}]
S1353 (GaAs)	4.4	0.7	14.1	1.97	2.4	0.8
S1774 (GaAs)	26.5	0.9	16.7	9.2	9.2	1.1
S1431 (InGaAs)	5.0	1.1	15.2	3.0	1.8	1.7

close to what is observed for sample S1353. The integrated surface under the fit is 26.5pW, which is an approximation of the emission power due to the intersubband transition without the absorption hole and without any parasitic emission. Similar fit has been performed on the peak at 14.1meV, leading to a power of 4.4pW. This output power is only 42% of the total collected power suggesting an injection efficiency of the same amount. The emission efficiency can however not be compared directly with these numbers, but must be transformed into photon fluxes. The photon flux is obtained by dividing the emission power with the measured photon energy. The obtained values are shown in table 3.2. The highest emission power is clearly obtained by the extrapolated emission peak of sample S1774. The emission efficiency can be obtained by performing the ratio between the injected electrons flux and the photon flux. The results show that the two GaAs samples have the same efficiency and that the InGaAs is slightly better but also with a broader emission. A clear distinction however cannot be made between the used material systems in terms of emission efficiencies as they are very similar. Note however that the calculated efficiency is not the quantum efficiency as it does not include the collection efficiency.

3.3 Diagonal Transition structure

3.3.1 Structure Design

The diagonal or photon assisted resonant tunneling transition structure S1443 consist of three GaAs quantum wells repeated 50 times. The structure starts with a 3.0 nm thick $Al_{0.15}Ga_{0.75}As$ injection barrier. The radiative transitions is diagonal in real space and occurs through the injection barrier from the ground state (2) of a 13.5 nm wide GaAs well to the ground state (1) of a 18.5 nm quantum well. The energy band structure diagram is shown in figure 3.11. It is designed to emit at the far-infrared photon energy of 14.4 meV with an applied electric field of 4.2 kV/cm corresponding to a working bias of 1.18V. The calculated matrix element is $z_{21} = 1.9nm$. As expected this value is less than half than what is calculated for a vertical transition ($z_{21} = 4.2nm$). Because of the diagonal nature of the optical transition, the lifetime of the excited state n=2 of the transition is expected to be much longer than the intersubband lifetimes of the other states.[65] The majority of the carriers should be contained in this state. In contrast to vertical transition structure, the injection barrier controls the current through the structure. The electronic density is therefore quasiconstant and population inversion should be maintained in a wide range of electric fields. A drawback to the diagonal transition is the expected spectrally broad emmission due to interface roughness. The center of the quantum well is doped with Si at a measured sheet density of $n_s = 1.67 \times 10^{10} cm^{-2}$

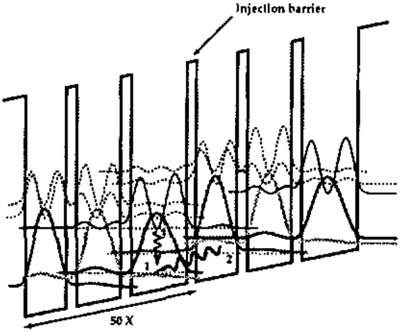

Figure 3.11: Energy band structure for sample S1443 in the GaAs/AlGaAs material system biased at $F = 4.2kVcm^{-1}$. The layer sequence in nanometers starting from the injection barrier is **3.0**/18.5/**3.5**/14.5/**3.5**/13.5 where $Al_{0.15}Ga_{0.85}As$ layers are in bold, $GaAs$ in Roman and underlined numbers correspond to the doped well (Si, $n_s = 1.6710^{10}cm^{-2}$).

3.3.2 Experimental results

The sample were processed in the surface emission configuration with a $15\mu m$ period grating on top of the etched mesa. Light and bias versus injected current measurements are shown in Fig. 3.12(a). In contrast to observed vertical transition transport data (Fig. 3.6) a NDR breakdown occurs with small injected current density showing electrical instabilities. The structure stabilizes with an applied bias of 1.4V corresponding to an internal field of $5.0kVcm^{-1}$.The excited state lifetime versus applied voltage is calculated by assuming that its lifetime is the longest present in the structure and $J = n_s q/\tau$, n_s being the measures sheet density and q the elementary charge (Fig. 3.12(b)). The obtained values of the lifetimes decreases from $\tau_{nr} = 100ps$ at low bias up to $\tau_{nr} = 20ps$ at 2V. Representative luminescence spectra for various current injection are presented in Fig. 3.13. At in injected current density of $J = 25.4cm^{-2}$ and at a bias of V=0.6 volts, we mainly see two peaks emerging from the

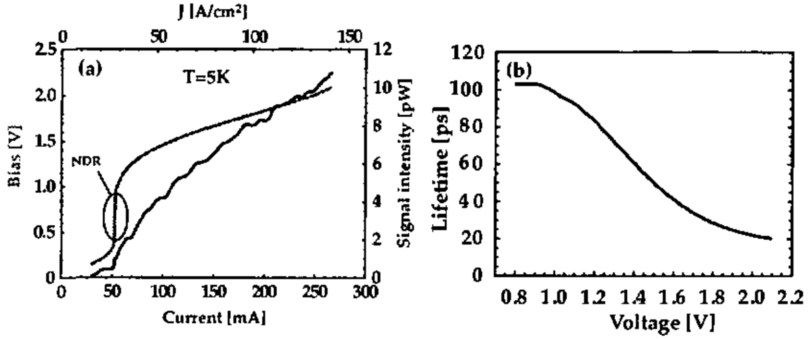

Figure 3.12: (a) Luminescence intensity and applied bias versus injected current. (b) Lifetime of the excited state versus applied bias.

noise. The first is at $h\nu = 28.7meV$. At this operating bias, the injection is broad and many states are populated, in particuler the excite state of the vertical transition n=3 to n=1 corresponding to the emission at 28.7meV. The second emission peak at $h\nu = 37meV$ attributed to the coupled phonon-plasmon emission induced by the grating As the current is increased, we observe that a peak at the photon energy of $h\nu \approx 14meV$ appear. An increase of the high energy peak is also observed. The peak at 14mev correspond very well with calculated diagonal transition energy from stated n=2 to n=1 for an applied electric field of $4.2kVcm^{-1}$. The phonon peak is however the most intense, suggesting strong heating of the sample. At an injected current of J=100mA the low energy peak becomes the most intense and the high energy ones decline. The phonon peak has now become the less intense of the three considered peaks. Finally at an injected current of J=230mA the diagonal emission peak has stronly increased in intensity and has blue-shifted as expected from a diagonal transition. The emission has also considerably broaden from 2.4meV at 59mA up to 12meV

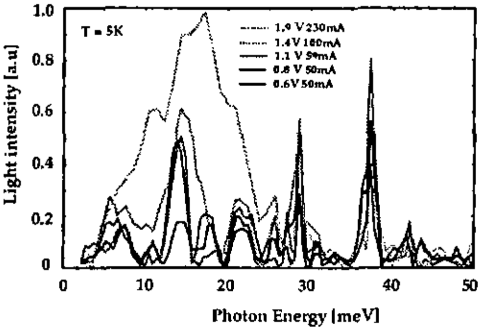

Figure 3.13: Luminescence spectra of the emitted radiaton for increasing injected current.

at 230mA. The observed FWHM at the desiged bias of 1.2V is much broader than what is observed for the vertical transition of sample S1353 and for the n=3 to n=2 transition in this one ($\Delta E = 0.7meV$ in both cases).

The vertical transition excited state n=3 being populated by carriers from the state n=2 having an excess kinetic energy, its population is given by the *Bolzmann* distribution. Extraction of the carrier temperature from the spectral data shown on Fig. 3.13 is possible. The integrated area under the emission peak is proportional to the carrier population, given by relation 3.3.4 where n_i is the population of the excited state and $\nu_{+,-}$ the boundaries of the emission peak.

$$P = \int_{\nu^-}^{\nu^+} I(\nu)d\nu \sim \frac{h\nu \times n_i}{\tau_{rad}} \qquad (3.3.4)$$

The population ratio between the excited states n=2 and n=3 of the diagonal and the vertical transition is given by relation 3.3.5.

$$\frac{n_3}{n_2} = \frac{A_{14meV}\tau_{2\to 1}}{h\nu_{2\to 1}} \times \frac{h\nu_{3\to 1}}{A_{28meV}\tau_{3\to 1}} = 4.810^{-3} = exp(-\frac{\Delta E_{32}}{kT}) \qquad (3.3.5)$$

The calculated spontaneous emission times are respectively for the diagonal and the vertical transition $\tau_{2\to 1} = 95\mu s$ and $\tau_{3\to 1} = 2.4\mu s$ computed with the transitions respective matrix elements. Using the areas under the peaks at a bias of 1.1V ($F = 3.5kVcm^{-1}$), a carrier temperature of T = 30K is obtained. Note however that this approximation does not take into accound the non-radiative depopulation rates for states n=2 and n=3.

An interwell electrically pumped intersubband transition struture has also been tried by Xu and Williams.[29, 30] In contrast to our structure the two lower levels are in resonnance with the optical phonon emission energy and are spatially separated in two adjacent wells. This allows to have a very efficient extraction from level n=2 without the disadvantage of phonon emission from state n=3 to n=1. The far-infrared emission was first very broad but managed in a second publication to have a narrow $\Delta nu = 1.9meV$ emission at 10.6 meV ($\lambda = 116\mu$) attributed to the n=3 to n=2 transition. Ulrich *et al.* have performed comparative measurements in magnetotransport and intersubband electroluminescence with similar vertical and diagonal as shown in this work.[32] They observed stark shift from the diagonal structure but smaller than the one expected with a homogenious electric field. Same emission efficiencies from both the vertical and the diagonal transition were observed.

Chapter 4

Non-Radiative Scattering Rates in FIR Vertical Transitions

4.1 Introduction

Determination of the electronic lifetimes of both the excited and the ground state of the optical transition in a structure is a key issue in understanding the carrier dynamics. In the far infrared, the corresponding sub band energy spacing being less than the optical phonon energy, relaxation through this channel is therefore forbidden as the temperature is lowered (Fig. 4.1). Other scattering channels are therefore responsible for the non-radiative depopulation of the excited state. The electron-electron scattering has shown to be a very efficient decay process for n=2 electrons in large quantum wells. It has been shown experimentally that the n=2 lifetime vary from 40 to 5 ps depending on the carrier density.[66] The sub-linear dependence of the luminescence with injected current observed from our vertical

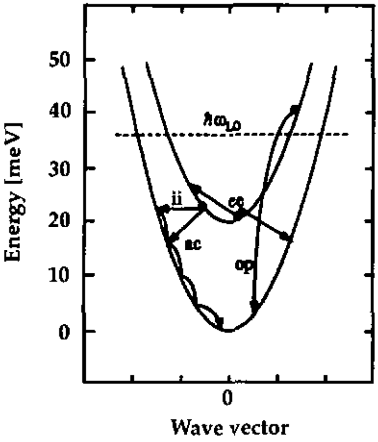

Figure 4.1: Schematic view of the intersubband relaxations processed for a quantum well where the energy separation E_{21} is smaller than the optical phonon energy. In this configuration, various processes may play a role: optical phonon emission (op), electron-electron scattering (EE), ionized-impurity scattering (ii), acoustic-phonon emission (AC).[41]

transition samples strongly suggest that at low temperature, the electron-electron scattering is the main limiting process (§3.2.2). An other important electron scattering process can occur through interface roughness. This effect is however expected to be important in narrow wells where the effect due to thickness fluctuations can become important.[64] This effect is enhanced with structures under high electric field, creating asymmetric potential pushing the electronic wave functions towards one side of the quantum well. This Stark effect however, becomes important under electric fields in the range of 100 $kVcm^{-1}$ and for narrow well width ($L < 10nm$).[41] In the far infrared, our structures are biased under fields not exceeding 5 $kVcm^{-1}$, leading to a weak potential asymmetry and the active wells width are much larger ($L > 20nm$) which strongly reduces the importance of interface roughness scattering for vertical transitions. This is clearly not the case for photon assisted tunneling transitions.

Acoustic phonons is an important relaxation channel as they may be emitted independently of the carriers energy as no frequency gap is present in the dispersion curve. But calculations performed by *Ferreira* and *Bastard* show that the emission lifetime of acoustical phonons increases with the quantum well thickness and has been calculated to be over 240ps for a 20nm well in the GaAs-(Al)GaAs material system with a 30% aluminum fraction.[55] These long lifetimes have been confirmed experimentally by *Faist et al.* as they have obtained lifetimes of $\tau_{ap} = 300ps$.[67] This decay process is not very significative in our case, as the wells used in our samples are very thick (28nm) leading to even longer lifetimes. Electron-impurity scattering however, has shown to have its lifetime decreased with the increasing well width. Calculated lifetime of 31ps for a 15nm thick undoped well are found.[55] This process can be an important decay channel as the active quantum well in our samples is relatively thick (28nm).

4.2 Electron-electron scattering rates

Electron-electron (EE) scattering being an elastic process, the total average energy and momentum of the carriers is conserved after the interaction. Even though energy and momentum may be transfered from one sub band to the other [68], this process does not allow net energy loss, but leads to a thermalization of the electronic populations. The dominat-

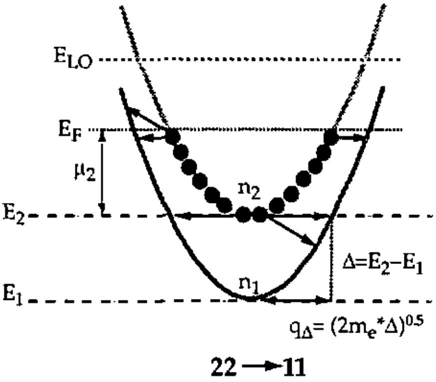

Figure 4.2: Schematic non equilibrium electron-electron scattering 2211 process between two sub-bands. The three pairs of opposite transitions arrows show the scattering between two upper sub band electrons which decay to the lower sub band E_1.

ing electron-electron scattering process between two sub bands are the 1212, 2112 and 2211 processes (where *klmn* is an interaction with carrier 1 scattering from sub-band k to m and carrier 2 from state l to n). 2221 processes also known as Auger processes where only one carrier changes sub band are forbidden. These type of scattering processes do not conserve parity and lead to an intersubband relaxation rate equal to zero.[68, 18] The first two dominating interactions allow energy and momentum transfer between sub band, but carrier populations remain unchanged and in this way do not depopulate the upper state, but lead to thermalization of the electronic populations of the two sub-bands. Process 2211, represented schematically in Fig. 4.2 is however the most effective intersubband scattering process when emission of optical phonons is not allowed and contribute strongly to the upper state depopulation.[66] Two carriers initially in the excited state scatter into the ground state with energy and momentum conservation. This process has shown to be directly proportional to the density of carriers of the upper sub band.[66, 69] As shown in Fig. 4.2, this process does not lead to a cooling of the carrier distribution as the energy is conserved. In contrast to the other processes, net transfer of carriers between sub-bands is achieved proving transport of carriers through the structure. It has been shown experimentally in time resolved pump-probe experiments that the 2211 processes are most efficient during the initial phase of the relaxation process.[69, 62] Its importance decreases as the two sub-bands approach a thermal steady state characterized by common electronic temperature and chemical potentials. This electronic thermalization arises after a few picoseconds after the femtosecond pulse excitation. In our experiments, as the current pulses are much longer than the relaxation time, the upper state is always in strong non-equilibrium during current injection and the EE scattering is always efficient. Knowledge of this rate in our structure is a key to the understanding of the carrier dynamics. At low temperature, maintaining a population inversion between the ground and the excited state rely strongly on the magnitude of the 2211 process rate and the electronic depopulation of the ground state.

The transition rate for a given process can be expressed by *Fermi's Golden Rule*. The rate is proportional to the amplitude for this process to happen (the matrix element), weighted by the density of available final states (The phase space) (Eq. 4.2.1). In relation 4.2.1, H' is the Hamiltonian describing the dynamics of the process.

$$\Gamma_{i\to f} = \frac{2\pi}{\hbar}|\langle f|H'|i\rangle|^2\delta(E_f - E_i) \tag{4.2.1}$$

Hyldgaard and Wilkins gave a simplified expression for the electron-electron scattering rate given by relation 4.2.2 where $U^0(q_\Delta)$ is the unscreened interaction matrix element and $I_P(0) \approx 0.785$ represents a dimensionless integrated phase space measure.[61]

$$\Gamma_{ee} = \frac{Ry*}{\pi^2} \times \frac{\mu_2}{\Delta} \times |U^0(q_\Delta)|^2 \times I_P(0) \tag{4.2.2}$$

Parameter $\mu_2 = E_F - E_2$ is the energy difference between the Fermi energy and the electronic confinement energy of the first excited state. The Fermi energy E_F can be computed by dividing the carrier sheet density n_2 by the two dimensional density of sates given in relation 4.2.3 where S is the macroscopic sample electrical injection surface.[35]

$$\rho(E) = \frac{m^* S}{\pi \hbar^2} \tag{4.2.3}$$

The rate in s^{-1} is then given by Eq. 4.2.4.

$$\frac{1}{\tau_{ee}} = \frac{\Gamma_{ee}}{\hbar} = n_2 \times \frac{Ry*}{\Delta} \times \frac{\hbar}{\pi m^*} \times |U^0(q_\Delta)|^2 \times I_P(0) \tag{4.2.4}$$

Assuming that the electron-electron scattering is the dominant non-radiative process, the injected current density can be written as $J = n_2 q / \tau_{nr} = n_2 q /\ 2 \times \tau_{ee}$ leading to an expression of the current density as a function of the square of the electronic population in the sub band (relation 4.2.5). As Eq. 4.2.4 gives the rate for the 2211 process to occur, the electronic transition rate is obtained by multiplying the latter 2211 rate by a factor of two as two

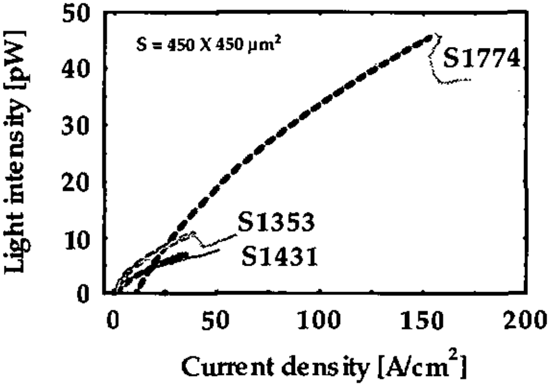

Figure 4.3: Light intensity versus injected current density is shown for vertical transition samples S1774, S1353 and S1431 at T=10K. A fit to the data is done with a square root function (dotted lines).

electrons are relaxing through this process.

$$J = \frac{n_2 q}{2 \times \tau_{ee}} = \frac{n_2 q}{2} \times n_2 \times \frac{Ry*}{\Delta} \times \frac{\hbar}{\pi m^*} \times |U^0(q_\Delta)|^2 \times I_P(0) \sim n_2^2 \qquad (4.2.5)$$

Finally, the emission power has a square root dependence with the injected current (Eq. 4.2.6).

$$P = \eta_c \hbar\omega N_p \frac{J}{e} \times \frac{\tau_{nr}}{\tau_{rad}} \sim \frac{J}{e} \frac{n_2 q}{J \tau_{rad}} = \frac{\sqrt{J}}{\tau_{rad}} \qquad (4.2.6)$$

As expected the emission intensity versus injected current for samples S1353, S1774 and S1431 are well fitted with a square root function (Fig. 4.3). A current offset has been used as the luminescence emission does not start at zero (see curve S1774). A certain current flows through the structure before it is fully aligned. As the injector is not aligned with

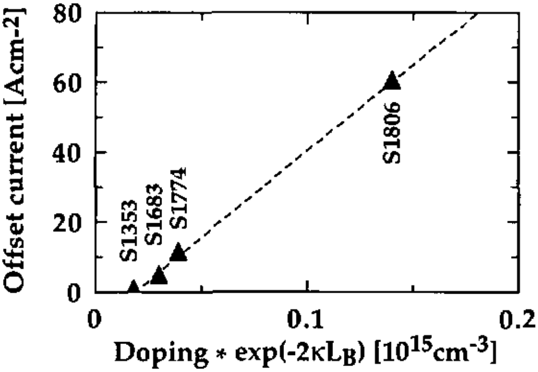

Figure 4.4: The offset current density is plotted versus sample doping. The latter is multiplied by a factor proportional to the (sequential) barrier transmission probability to take into account the different values of the injection barrier thicknesses of the samples($P_{1353} = 0.0059$,$P_{1683}= 0.0096$, $P_{1774}= 0.0063$, $P_{1806}= 0.019$).

excited state, no radiative emission takes place. The emission occurs when the states are aligned. This is achieved when the applied external field has overcome the internal electric field originated by the doped region. The offset therefore increases with the sample doping. In principle, a measure of the starting emission current could allow a determination of the sample doping (Fig. 4.4).

4.3 Measurement of the EE scattering rate

With increasing temperature the square root dependence with injected current has shown to vanish. At T=80K, the dependence on the emission intensity with injected current had become linear suggesting the appearance of a much more efficient scattering channel. At such high temperatures, thermally activated electrons makes the emission of optical phonons possible. This relaxation channel has shown to be extremely efficient with sub-picosecond lifetime and becomes the dominant relaxation process.[55] The non-radiative process in far-infrared vertical transition structures can therefore be described as the interplay between the electron-electron scattering and the emission optical phonon depending on the electronic temperature. Optical phonon emission is however possible at low temperature if we consider intra-sub band electron-electron scattering processes where the carrier gain sufficient excess kinetic energy after the collision. Monte Carlo simulation have shown that the ratio of carrier using this relaxation channel to the ground state is 25% .[62] The total non-radiative rate w_{nr} can be expressed by relation 4.3.7 with w_{ee} being the carrier-carrier scattering rate and w_{op} the optical phonon scattering rate.

$$w_{nr} = w_{ee} + w_{op,e} \times e^{-\frac{\hbar\omega_{lo} - \Delta E_{21}}{kT}} + w_{op,a} \times e^{-\frac{\hbar\omega_{lo}}{kT}} \qquad (4.3.7)$$

The last term of expression 4.3.7 takes into account the reabsorption of optical phonons by the electrons.

As the collected optical power depends on the electrical input power P_{el} and on the ratio of non-radiative lifetime τ_{nr} and the radiative lifetime τ_{rad}, temperature dependent mea-

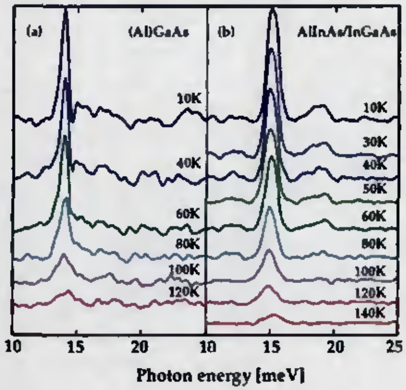

Figure 4.5: Luminescence spectra for (a)sample S1353 and (b) sample S1431 are shown up to respectively T= 120K and T=140K. We observe that intersubband transition peak intensity decreases with increased lattice temperature suggesting that the upper state lifetime decreases strongly with temperature.

surements of the emission power, together with Eq. 4.3.7, allows to extract the value of the carrier-carrier scattering lifetime.[29, 70] The value of the optical phonon scattering rate, however has to be calculated for normalization.

Temperature dependent spectra of the luminescence have been done for samples S1353 and S1431. Special care has been taken to minimize black body emission through sample heating. Unlike electron heating, lattice heating can be minimized by having the sample thermally well coupled to a heat sink. Residual heating can still be discriminated as the black-body's maximum emission intensity is out of phase from the luminescence emission. The injection current is chosen to be as high as possible, at respectively $39Acm^{-2}$ and $28Acm^{-2}$ at T=10K for maximum output power. Representative spectra are shown in Fig. 4.5 for both samples, the temperature being varied from T= 10K up to temperatures above liquid nitrogen for

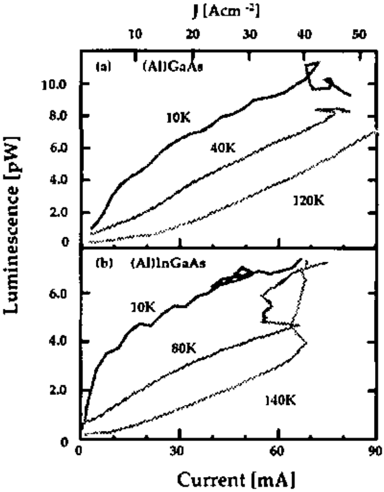

Figure 4.6: Light intensity versus injected current are shown for sample S1353 and S1431. We observe that the intensity of the emission at a given current decreases strongly with temperature. The square root dependence of the emission with injected current vanishes quickly with temperature.

both samples. At low temperature (T=10K), both luminescence spectrum show mainly a narrow peak centered at photon energies of 14.1 and 15.1meV. Increasing the temperature while keeping the injected current constant clearly shows a decrease in the peak intensity for both samples. The luminescence peaks are observed up to 120K for the (Al)GaAs, and 140K for the (Al)GaInAs. The full width at half maximum is equal to 0.7 and respectively 1.1meV up to high temperatures (50K and 60K) before increasing up to 2.2 and 1.9meV at respectively 120K and 140K. Similar line shape dependence with temperature is reported by *Heyman et al.* from absorption measurements.[71] Representative plots of the luminescence intensity versus injected current curves at different temperatures for both samples are shown

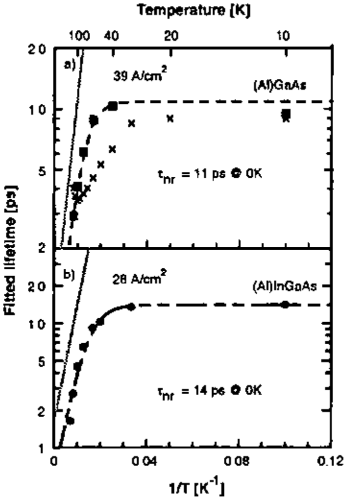

Figure 4.7: Activation graphs for sample S1353 and S1431 are shown. The data was fitted using Eq. 4.3.7 without the last term. Using the calculated optical phonon rates, the fit leads to electron-electron scattering rates of respectively 11ps and 14ps for the GaAs and InGaAs samples.

in Fig. 4.6. Activation graphs of the integrated peak intensity, taken from the spectral data are shown for both samples in Fig. 4.7. The data is well fitted using Eq. 4.3.7 where the last term of relation has been neglected. The calculated optical phonon scattering rate of w_{op}(GaAs)= 1.86 ps^{-1} and w_{op}(InGaAs)= 1.31 ps^{-1} and respectively the energies for the optical phonons of 36 meV, and 33 meV have been used.[55] Electron-electron scattering rates of respectively w_{ee} = 0.09 and 0.07 ps^{-1} for the GaAs and the GaInAs have been obtained, corresponding to intersubband carrier-carrier scattering times of respectively 11 ps and 14 ps. Crosses shown in Fig. 4.7 (a) are the integrated spectral power at the different temperatures. We observe that at low temperatures, it's value matches the integrated peak

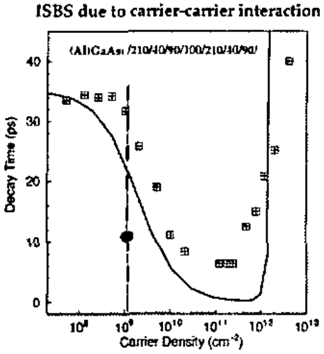

M. Hartig *et al.*, PRB 60(3) 1999

Figure 4.8: Experimental photoluminescence pump-probe data (crossed squares) and calculated (solid line) Intersubband Scattering time due du EE interaction in wide (21nm) quantum well.[66] Temperature dependent measurement data is represented by the black dot.

intensity. But as the temperature increases, the data differ strongly as black body emission increases and dominates the emission power.

The obtained values of the electron-electron scattering lifetime allows us to obtain the upper state density $n_2 = J\tau/q$ for both samples. Assuming a 100% injection efficiency, the carrier densities are respectively $2.7 \times 10^9 cm^{-2}$ and $2.4 \times 10^9 cm^{-2}$ for the GaAs and the InGas samples. These results are in good agreement with pump probe experiments done by *Hartig et al.*, as they have reported intersubband scattering times due to carrier-carrier interaction of 32 ps for similar carrier densities (Fig. 4.8).[66]

4.4 Optical Gain Calculation

In order to obtain light amplification in our structures, the active region must exhibit optical gain. The peak material optical gain of a wave traveling through the active region due to stimulated emission can expressed by relation 4.4.8 where $n_{i,f}$ are the electronic surface density of levels $E_{i,j}$ as defined in Fig. 4.9, n the refractive index of the medium, λ the wavelength of the emission, 2γ the the FWHM of the luminescence and L_w the thickness of the active well. [72, 73, 49, 74, 22]

$$G_p = \frac{4\pi q^2 z_{i,j}^2}{\epsilon_0 n \lambda 2\gamma_{i,j} L_w}(n_i - n_j) \tag{4.4.8}$$

Calculation of the gain requires the knowledge of the population inversion $n_i - n_f$ between the excited and the ground state of the transition. The population inversion can be obtained by solving the steady state rate equations characterizing the carrier dynamics of the structure, modelized in figure 4.9 by a two-level system.

$$\frac{dn_2}{dt} = \frac{J}{q} - n_2\left(\frac{1}{\tau_{spont}} + \frac{1}{\tau_{nr}^{21}}\right) \tag{4.4.9}$$

$$\frac{dn_1}{dt} = n_2\left(\frac{1}{\tau_{spont}} + \frac{1}{\tau_{nr}^{21}}\right) - n_1\frac{1}{\tau_{out}} \tag{4.4.10}$$

The population inversion is then expressed by relation 4.4.11.

$$n_2 - n_1 = \frac{J}{q}\left(\frac{1}{\tau_{spont}} + \frac{1}{\tau_{nr}}\right)^{-1} - n_1\tau_{out} \tag{4.4.11}$$

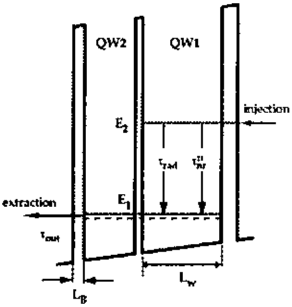

Figure 4.9: The vertical intersubband transition can be modeled as a two-level system where a non-radiative rate and a radiative rate depopulate the excited state E_2. The ground state E_1 is depopulated through a sequential tunneling to the relaxation/injection region of the structure.

We assume that the electronic population of the ground states of QW1 and QW2, instantly thermalize as they are separated with a small energy difference. The extraction however is assumed to be a incoherent (sequential) tunneling process through the 4nm barrier separating the active region from the relaxation region in sample S1353.[16] If the energy E_1 is such that $e^{-\kappa L_B} << 1$, where $\kappa = \sqrt{2m(V_0 - E)/\hbar^2}$, and L_B is the extraction barrier thickness, the transmission probability through the barrier of an electron can be approximated using Eq. 4.4.12. [3, 75]

$$T_B(E) \approx \frac{16E(V_0 - E)}{V_0^2} \times e^{-2\kappa L_B} \tag{4.4.12}$$

The tunneling time through the barrier can then be approximated using Eq. 4.4.13 with the effective mass of the electrons in the barrier.[16] The effective mass of the electrons in the $Al_xGa_{1-x}As$ is computed by a linear interpolation between the GaAs effective mass $m^{\Gamma_6}_{GaAs} = 0.067m_0$ and the effective mass of the AlAs $m^{\Gamma_6}_{AlAs} = 0.124m_0$. [35] The effective mass for

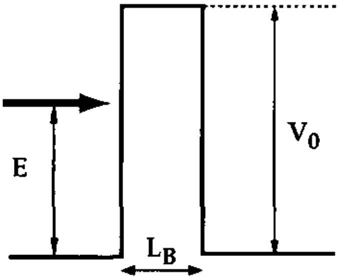

Figure 4.10: Particle of energy E incident on a single barrier of thickness L_B.

$Al_xGa_{1-x}As$ with x=0.15 is $m^* = 0.076m_0$. Figure 4.11 shows the electron tunneling time for increasing barrier thickness. For a barrier thickness of L_B=4nm we compute an extraction time τ_{out} = 6.4ps.

$$t_B \approx \frac{h}{E_1 T_B} \tag{4.4.13}$$

Using the experimental values obtained with sample S1353 of $J = 39Acm^{-2}$, with an injection efficiency of 42% (page 51) and $\tau_{eff}^{21} = 11ps$, an inverted population of $\Delta n = 4.7 \times 10^8 cm^{-2}$ is computed. Using Eq. 4.4.8, the peak material gain is $G_p = 43cm^{-1}$. In order to compare this result with mid-infrared results, the gain coefficient, $g = G_p/J$ traditionally used in the mid-infrared is $g = 2.6cmA^{-1}$ a factor 100 higher than what is computed for mid-infrared laser at threshold ($g \approx 0.015 - 0.029cmA^{-1}$).[72, 25] This suggest that the efficiency of this structure is much higher than mid-infrared ones. However due to the carrier density dependence of the EE scattering, this gain advantage is considerably reduced and eventually canceled with increasing operating current densities as the extraction time is constant. High temperature operation of such a laser seem to be difficult with

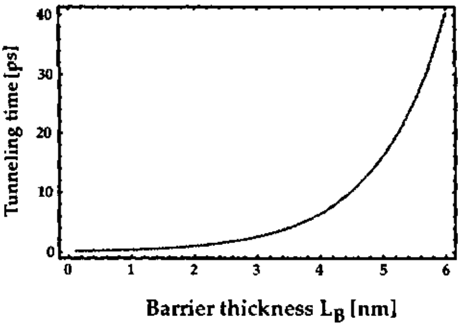

Figure 4.11: Calculated electronic tunneling time from state $E_{l'} = 0.014eV$ versus barrier thickness.

this structure as with increasing temperature, activation of optical-phonon emission will be possible and strong increase the non-radiative rate of the excited state will occur preventing any population inversion to build up.

Chapter 5

Waveguides

5.1 Waveguide Design

5.1.1 Introduction

The design of a low loss waveguide in the far-infrared is crucial for the realization of a laser device. As schematized in Fig. 5.1,at the interface between two dielectrics, total reflexion of an electromagnetic wave traveling in the material refractive index n_1 can be achieved at the condition that the refraction index $n_1 > n_2$. Furthermore the angle of incidence θ of the light inside the core must be smaller than a critical angle $\theta_c = Arcsin(n_2/n_1)$. In the mid-infrared this type of confinement provides good resonators and are obtained by growing low refractive index cladding below and above a high refractive index active region.[22] This can be done by molecular beam epitaxy (MBE) as the needed cladding thickness is at least in the order of $\lambda/2$ in the material. In the far-infrared however, waveguides based on pure dielectric confinement would require cladding thickness on the order of $10\mu m$ unadapted to MBE growth.

Figure 5.1: A dielectric waveguide is composed of a core with an index of refraction n_1 and a cladding with a refractive index n_2. A light beam inside the core will be totally reflected at the interface if $n_1 > n_2$ and if its angle of incidence $\theta \leq$ than a critical angle θ_c.

This technological difficulty can be avoided by using metal waveguides similar to what is used in microwave engineering. This technique was first used in QC structures by *Sirtori et al* in waveguides where the modes are not supported by a layered transparent medium but are electromagnetic surface waves or surface plasmon at a the metal-semiconductor interface.[76] These surface plasmon are TM electromagnetic modes confined at the interface between materials with dielectric constants of opposite sign. Metals below the plasma frequency exhibit negative dielectric constants and may be used for confinement. As the intersubband transitions selection rule requires TM polarizations, this type of waveguide is very suited for a quantum cascade laser.

5.1.2 Metallic Waveguides

In contrast to pure undoped dielectrics, metal may show Drude absorption due to free carriers. A metal can therefore be characterized with a complex index of refraction $\bar{n} = n + i\kappa = \sqrt{\epsilon_r} = \sqrt{1 + \bar{\gamma}/\omega\epsilon_0}$ where n is the usual refractive index and the imaginary part κ the extinction index function of the metal with $\bar{\gamma} = \gamma_0/(1 - i\omega\tau)$ being the Drude-Lorentz conductivity linking the current and the electric field ($J = \gamma E$).[77] The parameter ω is the light pulsation and $\gamma_0 = \tau n_e q_e^2/m$, the stationary conductivity with τ is the collision time (or polarization time). When $\omega\tau \gg 1$ the conductivity is purely imaginary ($\tilde{\gamma} \approx i\gamma_0/\omega\tau$) and the dielectric permittivity expressed in Eq. 5.1.1 is real.

$$\epsilon_r = 1 - \frac{\gamma_0}{\omega^2\tau\epsilon_0} = 1 - \frac{\omega_p^2}{\omega^2} \qquad (\omega\tau \gg 1) \tag{5.1.1}$$

where $\omega_p = n_e q^2/m\epsilon_0$ is the plasma frequency.

When the radiation frequency is smaller than the plasma frequency ($\omega < \omega_p$) and neglecting the scattering time ($1/\tau << \omega$), the permittivity is negative ($\epsilon_r < 0$) and the index of refraction $\tilde{n} = \sqrt{\epsilon_r}$ is purely imaginary. The reflection R, given by Eq. 5.1.2 is then total and the wave can be totally contained and ideally travel without any losses.

$$R = \tilde{r} \times \tilde{r}* \approx \frac{1 - i\kappa}{1 + i\kappa} \times \frac{1 + i\kappa}{1 - i\kappa} = 1 \tag{5.1.2}$$

Compared to waveguides based on dielectric confinement, this technique allows a drastic reduction of the cladding thickness, and allow a significant increase of the overlap factor between the guided mode and and the active material compared to a regular slab waveguide with the same thickness of the waveguide core ($\Gamma > 70\%$ for a single plasmon waveguide, $\Gamma = 100\%$ for the double plasmon waveguide, $\Gamma = 40\%$ for a slab waveguide). Mid-infrared InGaAs waveguides take advantage of the lower refractive index of the InP substrate to confine the optical mode. Surface plasmon confinement was used only on the top side of the

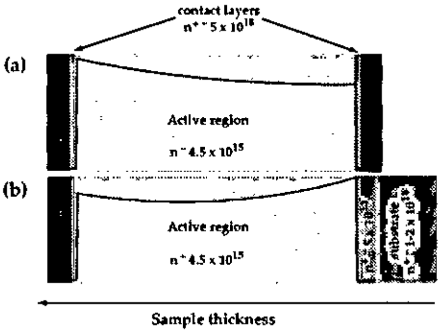

Figure 5.2: Computed mode profile for a double plasmon waveguide with a 120 period active region. Losses of $\alpha = 26cm^{-1}$ have been computed for a waveguide with a bottom gold layer (a) and $\alpha = 51cm^{-1}$ with highly doped GaAs bottom layer (b).

samples. In the GaAs material system the refractive index contrast between the active region and and the substrate is not sufficient to confine the mode. However, confinement is possible by performing a so called double plasmon confinement or simply a metallic waveguide by having a metal layer on both sides of the active region (Fig. 5.2). To make the device easier to manufacture, a heavily doped GaAs ($n = 5 \times 10^{18} cm^{-3}$) layer replaces the metal layer below the active region. Practically, the modes inside the waveguide a computed numerically by solving the Maxwell equations for a TM wave with a complex propagation constant. [49, 78, 79]Each layer is characterized with complex index of refraction leading to an effective refractive index of the multilayered active region calculated by the transfer matrix method. The imaginary part of the refractive index is obtained with the Drude-Jensen model where dielectric constant ϵ is given by Eq. 5.1.3 and the the plasma frequency $\omega_p = 4\pi n_e q^2/m^*$, n_e being the electron concentration and ϵ_∞ the high frequency dielectric

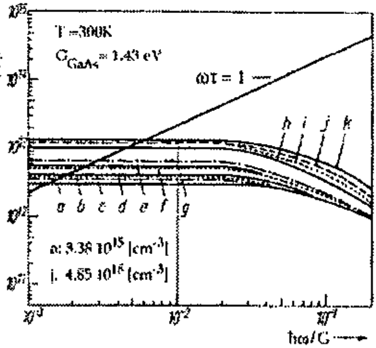

Figure 5.3: The total frequency-dependent relaxation rate versus x = $\hbar\omega/G$ for samples of GaAs of varying concentration. For doping concentrations similar to ones used in our samples, we obtain scattering rates of a:$\tau = 0.5ps$ and j:$\tau = 0.1ps$ at T=300K.

constant.[22] The scattering times τ are chosen depending on the average doping of the layers. The used values are taken from experimental measurements of the scattering times taken from reference [80] reproduced in Fig. 5.3.

$$\epsilon = \frac{\epsilon_{\infty} - \omega_p^2}{\omega^2} + i\frac{\omega_p^2}{\omega^3 \tau} \tag{5.1.3}$$

Replacing the bottom metal layer with highly doped GaAs leads to similar guiding properties as a metal-semiconductor-metal confinement, at the expense of higher calculated waveguide losses ($51cm^{-1}$ with doped GaAs instead of $26cm^{-1}$ for a gold layer). However the expected losses are much smaller to what is expected from extrapolation to the far infrared of mid-infrared waveguide losses. Laser resonator performances may be characterized by the ratio Γ/α of the mode overlap factor and the waveguide losses. In the mid-infrared, typical values

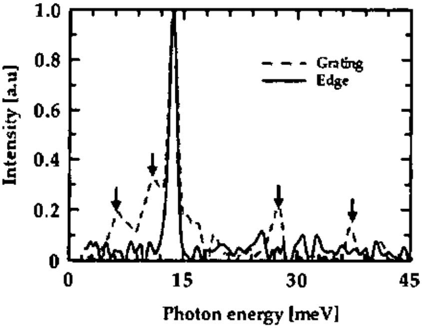

Figure 5.4: A waveguide version of structure S1353, processed in the grating and edge emission configuration. The main emission peak from the intersubband transition occur a the same energy for both configurations.

of the Γ/α ratio is $\approx 4\%\text{cm}^{-1}$.[24, 81] The overlap factor is increased up to Γ =70% to 81% by using a single plasmon waveguide, but with an increase of the waveguide losses of more than an order of magnitude compared to traditional cladding.[76, 22, 82] The double plasmon waveguide allows an overlap of $\Gamma \approx 100\%$ leading to $\Gamma/\alpha = 2$ to 4 in the double metal confinement configuration (Fig. 5.2(a)), with similar waveguide properties in the far-infrared as in the mid-infrared.

5.1.3 Experimental Results

A vertical transition structure similar to S1353, sample S1352 was grown with 60 periods of the active region embedded between 600nm highly doped $n = 8 \times 10^{18}$ GaAs confinement layers. Samples were processed in the grating and waveguide configuration. Emission from both configurations are shown in Fig. 5.4. We observe that the main emission peak from the intersubband transition occur a the same energy for both configurations demonstrating the edge emission capabilities of such waveguides. Side peaks appear on the emission spectra from the grating emission which do not appear on the edge emission spectra. These peaks attributed to plasmon emission are induced by the grating as they are absent from the edge emission spectra.[83]

The structure has been optimized to increase the gain with an injection barrier reduced from 6nm to 5.5nm. This increases the injection into the excited state at the risk of decreasing the non-radiative lifetime but allows an increase of the emission power. The extraction barriers have been shortened from 4nm down to 3nm to enhance the extraction of the electrons from the lower level ($\tau_{out} = 6.4ps \rightarrow 2.5ps$). Sample S1683 is grown with the active region repeated 120 times. The bottom confinement layer is 1000nm thick doped at $n = 5 \times 10^{18} cm^{-3}$ and followed by a 300nm parabolic grading of the potential to compensate the diffusion of the dopant and obtain an abrupt carrier distribution profile. On top of the active region, the same inverted parabolic grading is grown followed by a 80nm highly doped GaAs-InGaAs contact layer. The first well of the injector has been doped with Si and measured by capacitance-voltage measurements with an average doping of $n = 3.4 \times 10^{15} cm^{-3}$. Compared to our first vertical structure, the maximum injection current before appearance of the negative differential resistance region (NDR) is increased from $40.4 cm^{-2}$ to $100.4 cm^{-2}$. The waveguides are processed in 500 μm wide ridges by wet chemical etching and Ti/Au (10/400 nm) non-alloyed ohmic contacts were provided on top of the ridges by e-gun evaporation. The samples are then cleaved at different lengths and light intensity versus injection current density measurements were performed for increasing waveguide length.

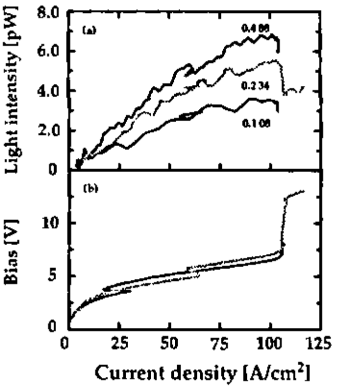

Figure 5.5: (a) Luminescence intensity plotted versus injected current density for various cavity length is shown. A clear dependence of the intensity with waveguide length is observed. (b) Applied bias versus injected current density is shown for the 0.234mm long waveguide. Similar curves have been obtained for the other length. Dotted line as a DC measurements showing similar electrical characteristics.

The $I - V$ curve for the 0.234mm long waveguide is shown in Fig. 5.5(b). In Fig. 5.5(a) we observe that at a fixed current density the light intensity increases with the waveguide length, demonstrating the waveguide properties of our samples. The polarization is found to be normal to the layers, indicating a transverse magnetic (TM) polarization as expected from the intersubband selection rule and also due to the geometry of the waveguide. In a rectangular metallic waveguide the electric field is required to drop to zero on the edges of the waveguide parallel to the wave's electric field, introducing a cut-off frequency. In our case, only the top and the bottom edges of the waveguide have a metallic confinement and the TM mode, having the electric field normal to the metallic planes, has no cut-off. However a cut off frequency is present for the TE mode and is given by the thickness of the spacing

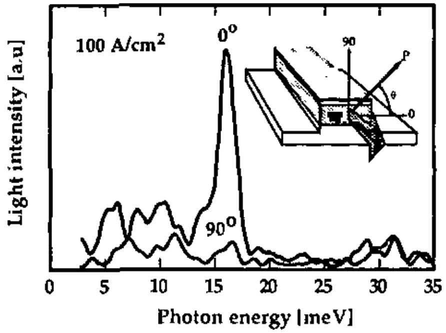

Figure 5.6: Waveguide emission observed after a grating polarizer as sketched in inset is shown. The vector P gives the direction of the grating polarizer. The light is transmitted when the grating is parallel to the layers (0^0) showing a TM polarization with the electric field parallel to the growth direction.

between the two metal layers.[77] Considering an active region of thickness $h = 11\mu m$ for sample S1683, the TE cut-off frequency is $\lambda_c^{TE} = 2 \times h \times n = 70\mu m$, n being the refractive index of the active region . Beyond this wavelength the transverse electric modes (TE) experience very large losses and therefore the waveguide induces a TM polarization of any radiation traveling inside it. In this sense, the intersubband selection rule is not formally demonstrated with the data presented in Fig. 5.6.

A structure grown in the InGaAs material system has been grown similar to sample S1683 embedded into a double plasmon waveguide. Unfortunately, no edge emission has been observed from the structure. This results suggests that the losses are much higher that than in the GaAs material system for such long wavelength. Similar results have be observed by other groups.[84]

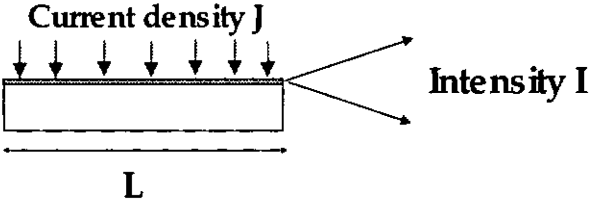

Figure 5.7: The use of a technique based on the analysis of the luminescence intensity as a function of waveguide length is used to extract the $(g(J) - \alpha_w)$ parameter of our samples, where $g(j)[cm^{-1}]$ is the gain inside the structure and α_w the waveguide losses.

5.2 Optical Gain Measurements

5.2.1 Introduction

As laser threshold has not been achieved, no immediate evidence of gain in our structures is observed. Specific measurement must therefore be performed to obtain the waveguide and active region characteristics. The use of a technique based on the analysis of the luminescence intensity as a function of waveguide length is used to extract the $g(j) - \alpha_w$ parameter of our samples, where $g(j)$ is the gain inside the structure and α_w the waveguide losses. When injecting current into the waveguide at a fixed injected current density J, every section of length dx of the waveguide will contribute with an emission intensity $dI(x)$. The guided light will then travel down the waveguide and will either be amplified or absorbed by the neighboring sections until it leaves the waveguide. The transmitted luminescence intensity I_t escaping the waveguide is therefore a function of waveguide length L and of the waveguide parameter $g(j) - \alpha_w$ which can be expressed by relation 5.2.4 where I_0 is the the luminescence

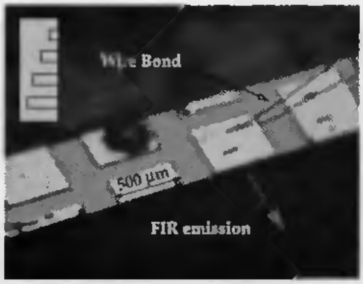

Figure 5.8: Photograph of waveguides of various length laying side by side is shown. This processing configuration as used to perform sample characterization of the gain and loss parameters.

intensity per unit length of the waveguide.

$$I_t = I_0 \times \int_0^L e^{(g-\alpha_w)x}\,dx = I_0 \times \frac{1}{g-\alpha_w} \times [e^{(g-\alpha_w)L} - 1] \qquad (5.2.4)$$

Performing measurements for different cavity lengths and at various injection current densities, allows us to extract both g and α_w separately.

5.2.2 Experimental results

For the experiment, a dedicated photolithographic mask has been designed in order to process waveguides of different length side by side on the same chip. A photograph of the samples processed in such a configuration is shown in Fig. 5.8. Measurements of the light intensity versus injected current density for waveguide lengths ranging between 100 μm and 1 mm are presented in Fig 5.9. Due to the very low light intensity obtained from these samples, we have plotted the results of successive measurements for each waveguide length. Solid

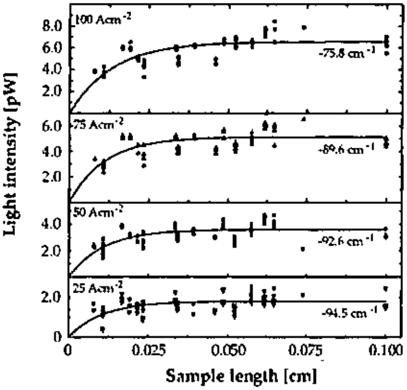

Figure 5.9: Measurements of the light intensity versus injected current density for waveguide lengths ranging between 100 μm and 1 mm is shown.

lines are fits to the data obtained by using Eq. 5.2.4 linking the emission intensity with the sample length. The dependence of the intensity with waveguide length is mainly observed for waveguide length $L < 500\mu m$. For longer waveguides, the light intensity saturates, indicating that light emission occurring further away is totally absorbed before reaching the edge of the waveguide. At the injection current density of 25 Acm^{-2}, the fitted waveguide parameter $g - \alpha_w$ is found to be -94.5 cm^{-1}. The waveguide parameter increases to $g - \alpha_w = -75.8cm^{-1}$ at the maximum injection current density of 100 Acm^{-2} suggesting a differential peak material gain of $G_d = 18.7cm^{-1}$ over the whole range of injected current densities. Computing the gain coefficient between $75Acm^2$ and $100Acm^2$, where the structure is supposed to be fully aligned, leads a differential peak material gain of $G_d = 13.8cm^{-1}$ and to $g = 0.55cmA^{-1}$. The computed peak material gain at $J = 39Acm^{-2}$ (with a 42% injection efficiency) is $G_p = 29cm^{-1}$, with a full width at half maximum of $\Delta\nu = 2.2$ meV

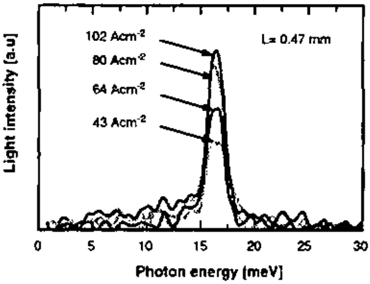

Figure 5.10: Electroluminescence spectra for various injected current density for a 0.4 mm long waveguide. The dip in the peak observed a low injection is due to the absorption of the detector window and is sample independent.

at this current density (Fig. 5.11). The resulting gain coefficient is $g = 0.74cmA^{-1}$ and is expected to decrease with increasing injected current density due the EE scattering rate of the excited state. The obtained results are very encouraging and suggest that gain is present in this structure. However a clear demonstration of the existence of gain is not possible due to the important dispersion in our experimental values. This dispersion is due to the used experimental method and to the very low signal intensities leaving the sample. The experimental method requires a realignment of the sample for different waveguide length. No reference is therefore available assuring an identical positioning of the various waveguides. The positioning criteria is fixed by the relative maximum intensity measured from each waveguide. A small misalignment of a few microns introduces important variation in the intensity. Furthermore, due to the cryogenic operating temperatures of the samples, temperature stabilization is also critical, as variation of the latter introduces variation in the sample holder position and directly affects the collected light intensity. This is particularly

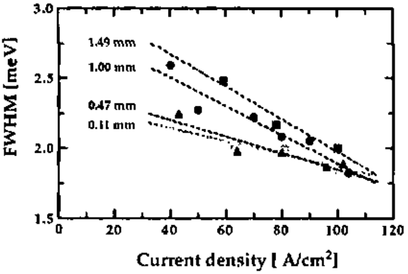

Figure 5.11: The FWHM of the electroluminescence spectra for various waveguide length is shown versus injected current density.

true for long waveguides as the injected current is important and heats the sample.

Signature of optical gain can be observed through luminescence peak narrowing with injected current density when the sample is close to laser threshold. [24]. Electroluminescence spectra for increasing injected current densities and for various waveguide length have been performed. Fig. 5.11 shows the FWHM of the luminescence peak with increasing current density from 43 Acm^{-2} to 100 Acm^{-2}. Narrowing of the FWHM with increasing injection current density is observed for all waveguide length and could suggest sub-threshold conditions. However, at a given current density, increasing the waveguide length, increases the FWHM of the emission, particularly for low injection current densities. The broadening with waveguide length can be explained by resonant reabsorption of the light by ground state carriers as the light travels through a medium of non-inverted population transitions. This reabsorption efficiency should decrease with the increase of the population inversion between the transition states. Results shown of Fig. 5.11 suggest that if the injected current density is increased, further narrowing of the peak linewidth should be observed. Sample

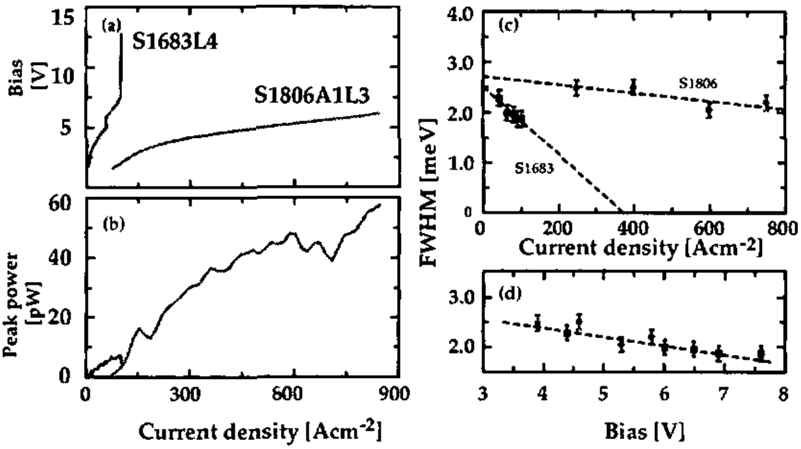

Figure 5.12: I-V (a) and L-I (b) curves versus injected current density for samples S1683 and S1806. Samples are respectively L= 0.46mm and L=0.4mm long and $l = 500\mu m$ wide. Measurements of the FWHM for sample S1683 (squares) and S1806 (disks) plotted versus injected current density (c) and versus applied bias (d).

S1806 optimized for higher injection current has been grown. The injection barrier is reduced to 4.7nm and the extraction barrier to 2.3nm ($\tau_{out} \rightarrow 1.3ps$). The average doping has been increased and measured at $n_{av} = 7.4 \times 10^{15} cm^{-3}$. This optimization allows an increase of the injected current density before appearance of the NDR, from 100 Acm^{-2} for sample S1683 up to 700 Acm^{-2} (fig. 5.12(a) and (b)). The average output power has been brought to more than 20 pW (45 pW peak) in the edge-emitting configuration. Unfortunately, the spectral data do not show any further narrowing of the emission peak (fig. 5.12(c)). Surprisingly, the optimized S1806 structure shows a smaller slope of the FWHM with increasing current than the S1683 structure, suggesting a gain independent process of the narrowing. A plot of the FWHM versus bias, shows however a good overlap between the two samples

(Fig. 5.12(d)) demonstrating a bias dependence of the narrowing. The origin of the observed narrowing is therefore not due to electronic population inversion in the structure, but rather from changes in the electric field. As the structure aligns with the field, the state anti-cross with a minimum energy splitting when the structure is correctly aligned. As the operating temperature is non zero and the injection efficiency smaller than 100%, anti-crossing states are both populated and spontaneous emission may be initiated from both states down to the ground state. The observed decrease of the FWHM correspond to electric field dependant energy splitting of the excited states and reaches its minimum juste before the NDR.

5.3 Waveguide Loss Measurements

5.3.1 Introduction

Conventional techniques usually applied to measure waveguide losses in semiconductor lasers [85, 86, 87] are not applicable in our samples, as the observed luminescence intensity is too weak. The technique using a single, multi-section device, is however feasible as it uses the luminescence generated by the QC structure inside the waveguide as the light source.[88] In this configuration, separated electrical contacts of constant area are provided on top of the waveguide (Fig.5.13). The light intensity I_0 produced in a pumped section will travel down the waveguide to the edge of the sample with the intensity decreasing accordingly to Eq. 5.3.5 where I_t is the transmitted light intensity measured at the edge of the waveguide, L the optical path length measured from the pumped section to the sample edge and α_w the

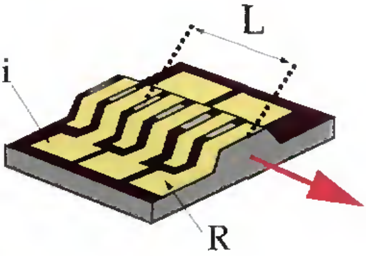

Figure 5.13: Schematic of the sample processed in the multi-section single-pass absorption measurement. The optical path length is modified be sequently pumping different section (i) of the waveguide.

waveguide loss.

$$I_t = I_0 \times e^{-\alpha L} \tag{5.3.5}$$

The initial light intensity I_0, identical for all sections provided that they are pumped with same current, can be obtained by measuring the light intensity produced by pumping the front section (labeled R in Fig. 5.13). Pumping an other section of the waveguide changes the light path length. Practically this means removing the sample from the measuring set-up and rewiring it. Initial alignment can therefore not be perfectly reproduced. This can be overcome by measuring both the transmitted light and the reference light intensity for each path length allowing further renormalization of the intensities. Waveguide losses are obtained by a fit to the renormalized intensities plotted versus light path. A slight complication to this method is that the sections are electrically not completely isolated from each other. A leakage current into the nominally unpumped sections might provide parasitic contributions to the luminescence. This leakage has the final effect to underestimate the true

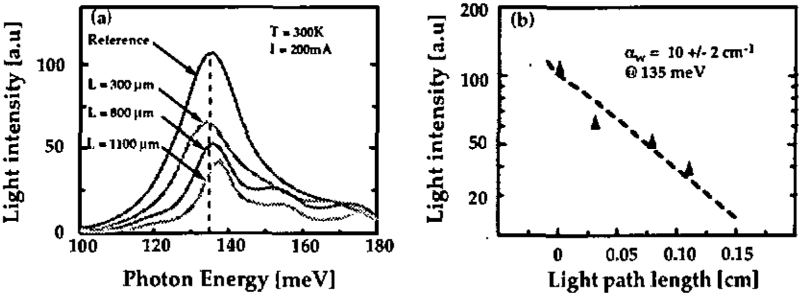

Figure 5.14: (a) Mid-infrared luminescence spectra obtained for different optical path length, from a QC laser (S1850) working under laser threshold at room temperature. (b) the peak intensities at the transition energy are reported versus optical path length. Dotted line is a fit to the data.

waveguide loss. These contributions can however be deduced experimentally and included in the function used for the fit.

5.3.2 Technique Validity Check

To check the validity of the technique, waveguide loss measurements have first been performed on a state of the art 9.1 μm InGaAs/AlInAs mid-infrared quantum cascade laser (S1850)*with an MOCVD re-grown InP waveguide cladding operated below laser threshold.* The sample processing is similar to the one described below for far-infrared measurements.

Spectral measurements have been performed at a constant current of 200 mA and at room temperature. Figure 5.14 shows the luminescence observed from the edge of the sample, for various light propagation lengths. All shown spectra have been renormalized to one com-

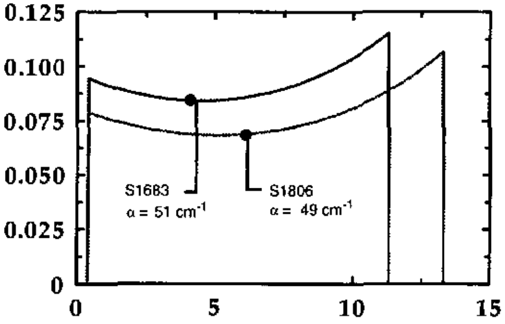

Figure 5.15: Computed mode profile for sample S1683 and S1806. An average doping of $n_{avg} = 3.4 \times 10^{15}$ and $n_{avg} = 7.4 \times 10^{15} cm^{-3}$ have respectively been used for sample S1683 and S1806.

mon reference spectra. The peak intensity is plotted as a function of optical path length in Fig.5.14(b). A fit to the optical data gives loses of $10{\pm}2cm^{-1}$, which correspond well to the calculated loss of 9.5 cm^{-1}. In order to take into account the effect of the leakage current while injecting current into one section, we have measured the bias on the other ones. Current versus voltage curves performed for each section enabled us to obtain the current flow for each section. An exponential approximation for the current versus waveguide length was used as a corrective term in the fitting function, resulting into a 3% increase of the true waveguide losses.

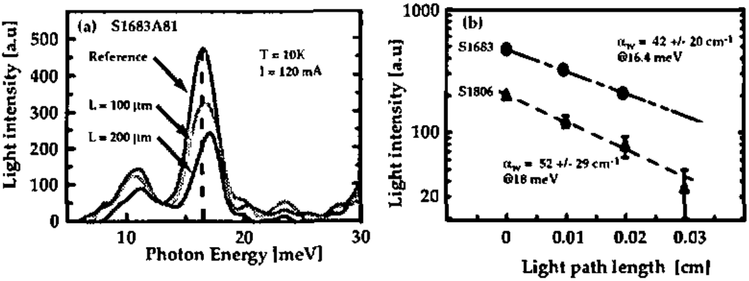

Figure 5.16: (a) Obtained far-infrared luminescence spectra from a double plasmon waveguide for various optical path lengths for similar processing as shown in Fig. 5.13. (b) Reported intensities as a function of light path length for two active regions, emitting at 16.4 and 18meV are presented.

5.3.3 Far-infrared Waveguide Loss Measurements

For far-infrared waveguide loss measurements, layers S1683 and S1806 described in §5.2.2 have been used. For the experiment, the previously etched ridges were processed with 90 μm wide injection sections which had a separation of 10 μm between each other and deposited on top of the 500 μm wide ridges by e-gun evaporation of Ti/Au (10/400 nm). To prevent device short-circuiting due to lateral ridge current injection, a hard-baked resist layer has been used as an electrical insulator. Samples were soldered with indium on copper mounts. Data have been taken at a temperature of 10K for both samples and with an injection current of 120 mA and 500 mA respectively for sample S1683 and S1806. Figure 5.16(a) shows the renormalized spectra for sample S1683. Similar results have been obtained for the other sample. An identical baseline correction has been made to all the spectra in order to remove the black body emission due to sample heating. A decrease of the luminescence peak at

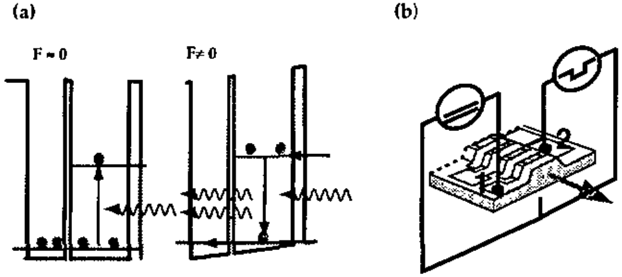

Figure 5.17: (a) When the structure is unbiased, the carriers are located in the ground state of the well. Carriers may be excited by absorbing photons. When the structure is biased, the carriers cascade through the structure and do not accumulate in the ground state of the well and reabsorption is therefore less likely to happen. (b) For the resonant reabsorption experiment, section 2 bias with a pulsed current, and section 1 is either grounded or DC biased.

16.4 meV with increased light path length through the waveguide is clearly visible. However the side peak at 12meV does not show the same clear effect. It is thus attributed as an artifact occurring from the black body background. Luminescence intensity at 16.4 and 18 meV for samples S1683 and S1806 are plotted as a function of optical path (Fig. 5.16(b)). Fits to the data, with the current leakage correction, give cavity losses of $\alpha_w = 42 \pm 20 cm^{-1}$ and $\alpha_w = 52 \pm 29 cm^{-1}$ respectively for sample S1683 and S1806. Calculation of the losses based on free carrier absorption give according values of $\alpha_w = 51 cm^{-1}$ and $\alpha_w = 49 cm^{-1}$. The large error bars on our results originate mainly from the relatively low output power (typically less than 4 pW) in the edge configuration compared to the noise level. These low output powers also limit the range of light path lengths available to the experiment. Noise has been reduced by increased integration time (5 seconds per spectral point), but still remains important (nearly 10 % of the most intense peak presented in Fig. 5.16(a)). The

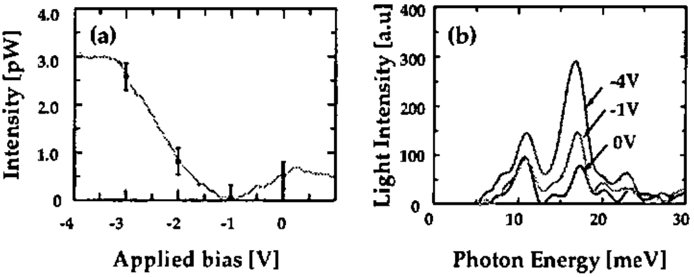

Figure 5.18: Resonant absorption of the luminescence is demonstrated. Pulsed current injection is kept constant in section 2 and section 1 is either grounded or DC biased (Fig. 5.17) The observed luminescence intensity leaving the waveguide increases with applied DC bias on the foremost section (a). Spectral measurements show a spectrally selective increase of the light intensity with increasing negative bias close to the emission energy, showing that this effect originates from the intersubband transition (b).

structures based on a vertical transition, does not exhibit significant Stark shift with applied voltage and will therefore show resonant reabsorption when the ground state is populated. This effect was not significant in our results presented above, because of current leakage, which always slightly biases the front sections. Resonant reabsorption has however been observed when section 1 was either grounded or when a small DC voltage was applied while pulsed injection in section 2 was kept constant (Fig. 5.17). Spectral measurements at various bias show that the optical transition is responsible for this effect, as a selective increase of the light intensity is observed at approximately the luminescence emission energy. Strictly speaking, we are therefore not measuring the waveguide losses at zero injected current, but the ones with which might always contain some small gain effect.

5.4 Vertical Structure in a Magnetic Field

5.4.1 Introduction

Waveguide loss measurements performed on the far-infrared waveguides show that the optical losses are $\alpha_w = 42cm^{-1}$ for sample S1683. Gain calculations performed with the latter waveguides suggested gain coefficient of $G_p = 0.74cmA^{-1}$ with a peak material gain of $G_p = 29cm^{-1}$. An increase of th gain is therefore necessary to reach laser threshold. Blank *et al* have suggested that a quantum well intersubband laser should work much better in the presence of a magnetic field, compared with the original design without a magnetic field.[89] In their proposal, they show that the effect of the magnetic field perpendicular to the AlGaAs/GaAs quantum wells dramatically reduces the EE scattering intersubband rates. If the scattering rate could sufficiently be reduced or even canceled, the gain in our structure could be increased and compensate the waveguide losses until laser action occurs. This inhibition of the scattering processes occur as the magnetic field introduces series of discrete Landau levels for both the excited and the ground state. At appropriately chosen magnetic fields, it is possible to reduce the various interband transitions processes due to new energy conservation requirements (see figure 5.19). Far-infrared intersubband electroluminescence enhancement by a magnetic field is reported by Ulrich *et al* from a vertical transition far-infrared (Al)GaAs QC structure emitting at 17.3meV processed as ridge mesa. At a field of B = 7.2 T they report an emission intensity twice the one measured a B = 0 T demonstrating the non-radiative transition rate reduction by a perpendicular magnetic field.[54]

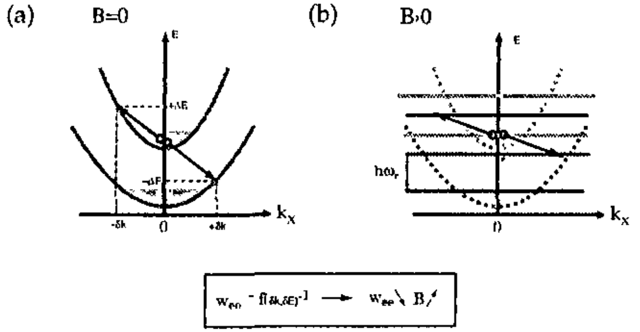

Figure 5.19: (a)Parabolic dispersion of the sub-bands allows a continuous C-C scattering process with energy and momentum conservation (b)Applying a magnetic field normal to the quantum wells discrete Landau levels appear. The parabolic dispersion of the energy is then replaced by a discretized energy spectrum. Energy and momentum conservation rules ruling carrier-carrier scattering are less likely to be satisfied decreasing consequently the non-radiative rate.

5.4.2 Experimental results

In our samples available gain is limited by the extraction lifetime τ_{out} and from the non-radiative lifetime τ_{nr}. Reducing τ_{nr} should increase the gain and posibly reach laser threhold. For the experiment, S1683 samples processed into waveguides were used. A schematics of the used set-up is shown in Fig. 5.20. The emission from the sample is guided by a closed 20 cm long light pipe to an InSb photoconductive detector. The detector is biased with a constant current and operated in the cyclotron resonance mode. The spectral width of the cyclotron resonance photoconductive response is about 1.1 meV. By tuning the magnetic field, the spectral sensitivity can be changed according to the cyclotron resonance frequency $\nu_c = eB/m^*$ where B is the magnetic field and e is the electron charge. The detector has a tuning constant of about 8.06meV per Tesla. Spectral measurements are performed by

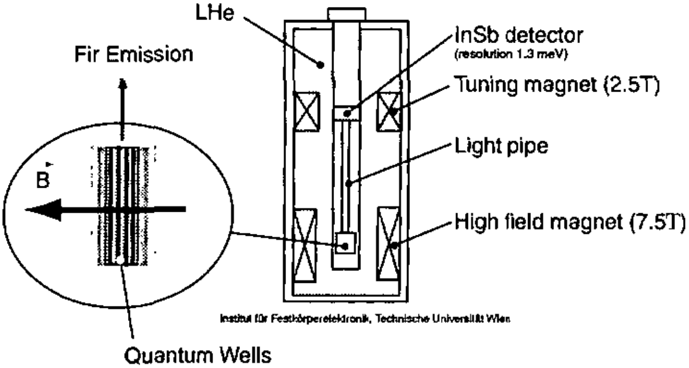

Figure 5.20: Set up used to perform luminescence measurements in a magnetic field normal to the layers. The measurements were done at TU Wien, in collaboration with J. Ulrich *et al.*.

tuning the top superconducting magnets from B=0T to a maximum of B=2.5T changing the cyclotron resonance frequency of the InSb detector of to a maximum photon energy of $\hbar\omega \approx 20meV$.[28] The whole spectrometer and the sample are submerged in liquid helium. Figure 5.21(b) shows the light intensity from the waveguide with the applied magnetic field of B=0T to B = 7.5 T for a constant injected current of 130mA. The Insb detector is constantly tuned at the intersubband transition energy. We observe an increase of the emission intensity with a maximum at B = 6.63 T. This maximum intensity is more than a factor 2.5 higher than a B=0T. This increase of intensity is not monotonous with increasing magnetic field but exhibits oscillations due the Stark-cyclotron resonances (SCR) due to elastic tunneling between the Wanier-Stark-Landau levels with non-equal quantum numbers on neighboring wells. A resonance occur if the energies of the initial and the final state coincide and the

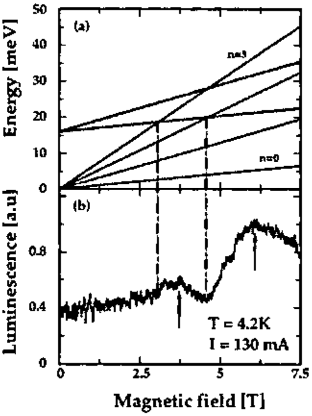

Figure 5.21: (a) Energy levels of sample S1683 plotted versus applied magnetic field for a sub-band energy separation of 16.1 meV. (b) Light intensity plotted against applied magnetic field with a constant injected current. The detector was constantly tuned at the photon emission if the intersubband transition.

carrier may escape through this channel decreasing the overall non-radiative lifetime and thus decreasing the emission intensity.[54, 33] Fig. 5.21 (a) show the energy levels of sample S1683 plotted versus applied magnetic field for a sub-band energy separation of 16.4 meV. The observed minima of the emission correspond very well with the corresponding resonances of the excites state Landau level $n_1 = 0$ and the ground state $n_0 = 3$ and $n_0 = 4$. Similarly, the maxima in the emission intensity correspond to the anti-resonance of these levels. Spectral measurements performed with a constant injected current of $J = 230mA$ ($j = 82.4cm^2$) and increasing magnetic field up to 6.6 Tesla are shown in Fig. 5.22. The poor signal to noise signal obtained during these experiments is due to the low signal intensity from the edge emission. Nevertheless we observe an emission peak occurring at 16.1meV and slightly

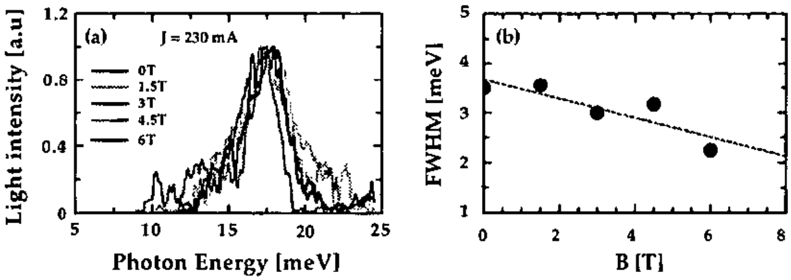

Figure 5.22: (a) Spectral data from a waveguide at a constant current density of $82Acm^{-2}$ with increasing magnetic field.(b) The FWHM of the emission versus applied B field is shown.

red-shifts with increasing field. The red-shift is an artefact due to the influence of the high magnetic field on the InSb detector. The full width at half maximum show a decrease with increasing field from 3.5meV to 2.2meV at B=6.6T (Fig. 5.22(b)). Subtracting the detector linewidth of 1.1 meV we observe a true narrowing of more than 50%. This narrowing of the emission peak is similar to what was observed by Ulrich *et al* on their vertical transition samples (30%) and does not suggest any narrowing from stimulated emission. The narrowing more likely occurs from the in plane dephasing time involving scattering between Landau levels which increases proportionally with the applied magnetic field. [54]. The effect of the intersubband lifetime increase due to the magnetic field is too small to be observed compared to the other broadening processes. Assuming an increase factor independent of current and taking $\tau_{B=0} = 11ps$, the effect of the magnetic field induces a narrowing of $\delta E = 0.25meV$ at 6.6T. Fig. 5.23 shows spectral measurements at a constant high magnetic field of B=6.6 Tesla and for varying injected current from J=90mA up to J=230mA. As expected, no shift of the emission peak are observed. The FWHM of the emission peaks however do show a narrowing

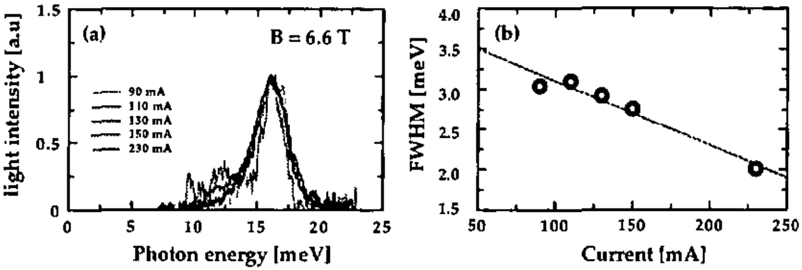

Figure 5.23: (a) Spectral measurements performed with increasing injected current and a constant high magnetic field of $B = 6.6T$. (b) A plot of the FWHM of the emission peak plotted versus injected current is shown.

from $\Delta E = 3.0meV$ at J= 90 mA down to $\Delta E = 2.2meV$ at $J = 230$ mA. These values are very similar to what was obtained in absence of applied magnetic field (see figure 5.11) and therefore do not show evidence of gain in these structures. Further experiments with the high magnetic field set-up in Neuchatel were performed on sample S1683 and samples S1774. The latter is processed with a grating on top of the mesa for surface emission. The objective of these measurements is explore the possibility of gain enhancement with an applied magnetic field perpendicular to the epitaxial layers up to the full quantization limit with a magnetic field of B = 14T. Both structures are similar but not identical as sample S1683 is optimized for carrier extraction as described earlier and cannot directly be compared. In any case, if gain is present in the structures and is enhanced by the magnetic field, the observed narrowing from the waveguide sample should be much stronger than from the surface emission sample. In the first case, narrowing due to gain will be added to the effects due to the reduction of the E-E scattering rate and in-plane dephasing time with applied magnetic field. In the second

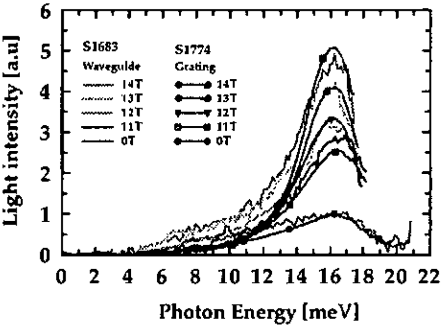

Figure 5.24: Spectral measurements performed with a constant injected current up to a magnetic field of B = 14T for sample S1683 and S1774 processed respectively into a double plasmon $683\mu m$ long waveguide and with grating for surface emission.

case the effect of gain will have no contribution to the narrowing due to the absence of any waveguide. Furthermore the intensity increase with applied magnetic field should increase faster for the waveguide sample than for the surface emission sample. The emission spectra for both configurations is shown in figure 5.24. The measurements have been performed at a constant injected current and increasing applied magnetic field. The emission intensities have been normalized to unity for no applied magnetic field. The data shows an increase of the emission intensity of a factor of ≈ 5 for both samples with an applied magnetic field of B = 14T showing no extra enhancement of the output power for the waveguide sample compared to the surface emission sample. Narrowing is however observed for both samples but with similar values. However true linewidth is difficult to measure due to the presence of the cyclotron resonance emission peak present on the edge emission spectra and due to the relatively large intrinsic linewidth of $\Delta\nu = 3.4meV$ of this InSb detector.

The obtained results do not demonstrate the inexistence of gain in our structures as its effects are only expressed close the laser threshold. Recent achievement of a far-infrared laser allows the open question of gain enhancement with applied magnetic field to reach an answer. If this this assertion is true, a reduction of the threshold current density will be observed with increasing applied magnetic field.

Chapter 6

Second Generation Active Regions

6.1 Introduction

We have seen in the previous chapters that electro-luminescence from an intersubband far-infrared transition is possible, and more more specifically that electrical pumping is possible using a cascade type injection. Our experiments on the active regions suggest that population inversion has been achieved and that some gain is present. Furthermore the plasmon waveguide have shown to have relatively low losses. But as laser threshold is not reached at this stage both the active region and the waveguide must be improved.

Study of the structures has shown two main bottlenecks: the injection and the extraction of the carriers. Increasing the injection allows to have more carriers on the excited state and increases the gain provided population inversion is maintained. In the vertical transition, the non-radiative lifetime of the excited state is inversely proportional to the carrier density, and therefore decreases with increased injection limitating the maximum upper state population. The second bottleneck is the ground state extraction. The extraction time in our structures is relatively slow as the carriers must tunnel through a barrier with a tunneling time dependent on the barrier thickness. The vertical ransition is therefore not adapted as active region for a FIR-QCL. The diagonal structure should be a good candidate but has exhibited broad emission reducing the possibility of high gain.

Since the demonstration of the QCl in the mid-infrared, dramatic performance improvement has been achieved both in output power, temperature and in the increase of the emitted photon wavelength. The output powers and operating temperature have been greatly increased with the so called vertical three quantum wells design (3QW).[90] The injection efficiency was significantly increased by increasing the overlap between the exited state wave-function and the ground state of the injector, while reducing the overlap of the latter with the ground states active region. This overlap increase is done using a chirped superlattice simultaneously as a funnel injector and a Bragg reflector suppressing the escape of the carriers from the excited state of the transition. This allows high performance device to reach an emission peak power of 55mW at a wavelength of $\lambda = 11.5\mu m$ at room temperature.[91] The longest wavelength reached with this design is so far $\lambda \approx 13\mu m$.[92] However, these devices exhibited fairly limited performances with a maximum operating temperature of $T_{max} = 175K$. The limitation is due to a bottleneck with the carrier extraction. Recently a structure design with a mini-band extraction has demonstrated significant increase of operating temperature and output power.[93] Improvement on the emission wavelength has been obtained using devices based on chirped superlattice active regions with demonstrated operation at much longer wavelengths, reaching 17, 19, 21 and finally up to $\lambda \approx 24\mu m$. [94, 95, 82, 27] However, these structures are limited to operation temperatures below $200 - 240K$

6.2 Far-infrared Chirped Superlattice

The successful improvement obtained in the mid-infrared suggest that far-infrared structures could reach laser threshold by taking advantage of the mid-infrared QCL evolution. The main limiting factor in the first generation of far-infrared structures is the extraction of the carrier from the ground state. Reducing significantly the extraction barrier would allow to reduce significantly the tunneling time. This can be done in chirped superlattices consisting of a periodic stack of quantum well and barriers. This type of structure creates an artificial crystal with electronic conduction band and band gaps similar to what is observed in bulk semi-conductors, but inside the conduction band and the valence band. However, to electrically inject carriers in such a true superlattice, it must be biased. This causes the structure to form a Stark ladder , as proposed by Kasarinov and Suris.[9] Such a structure is electrically unstable and practically useless as a quantum cascade active region. Scarmarcio *et al.* have stabilized such a structure by inserting doped region between undoped regions to keep the mini-band structure and simultaneously having a potential drop, creating this way an injector and an active region.[96, 97] The minimize dopants into the structure, the mini-bands can be kept flat without any dopants with the so-called chirped superlattice. An effective quasi-electric field is generated by chirping the superlattice period so that a flat mini-band condition can be reached.[98] Very thin barriers can be used in such designs allowing to have quasi-continuum bands where the carriers travel without being limited by the barrier tunneling time together with the interface roughness scattering from the multiple barriers will enhance the extraction

6.2.1 Structure design

Superlattice with far-infrared interminiband optical transition energies have been designed both in the AlInAs/InGaAs and in the AlGaAs/GaAs material. Schematic band diagram are shown in Fig .6.1 and Fig. 6.2 Both structures are very similar and consist of a four well injector and a three-well active region leading in both cases to two well defined mini-bands. The injectors lower mini-band is matched to the active superlattice upper mini-band through a 2.5 nm AlInAs respectively 4.0 nm AlGaAs injection barrier. The expected terahertz emission should be dominated by a pronounced peak near the wavelength corresponding to the mini-gap between the second and the first mini-band [96]. The ground state of mini-band 1 and the ground state of mini-band 2 of the InGaAs sample reach a minimum of the energy slitting of $\Delta E = 0.84 meV$ with an applied electric field of 2.1 kV/cm. The calculated optical transition occurs with a photon energy of $h\nu = 16.4 meV$. The matrix element is longer than in the vertical structure with a value of $z_{if} = 8.1 nm$. Beyond the minimum, the energy splitting increases strongly (Fig. 6.3 (a))and higher states of the mini-band are then easily populated decreasing the injection efficiency. Similarly, the GaAs sample reaches its minimum energy splitting of $\Delta E = 1.56 meV$ with an applied electric field of 4.0 kV/cm. The computed optical transition is $h\nu = 18.5 meV$ with matrix element $z_{if} = 7.2 nm$.

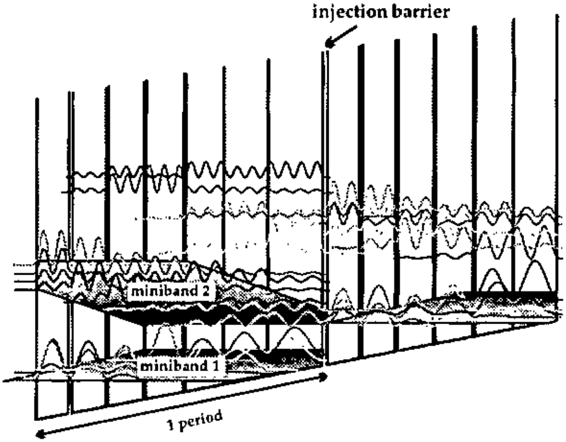

Figure 6.1: Energy band diagram of two periods of the AlInAs/InGaAs structure S1677 under an average applied electric field of $2.0kVcm^{-1}$. The optical transitions occur between two inter-sub-mini-bands. The layer sequence of one period of structure, in nanometers, left to right and starting from the injection barrier is **2.5**/29.0/**0.4**/23.0/**0.3**/20.0/**1.3**/20.0/**1.0**/19.0/$\underline{\mathbf{1.3}}$/18.0/**1.8**/17.0/ where $In_{0.52}Al_{0.48}As$ layers are in bold, $In_{0.53}Ga_{0.47}As$ in Roman and underlined numbers correspond to the doped region ($Si, 3.8\times10^{10}cm^{-2}$).One period of the structure is 154.6 nm long.

6.2.2 Experimental results

For the experiments, the InGaAs design was grown with 35 periods and processed into mesas with a $15\mu m$ grating periodicity on top of the sample. Simultaneous measurements of the voltage and optical output power versus injection current performed at low temperatures (T = 10K) for the InGaAs sample (S1677) are shown in figure 6.4. In contrast to measurements performed on a vertical transition structure [31], the luminescence efficiency is constant with

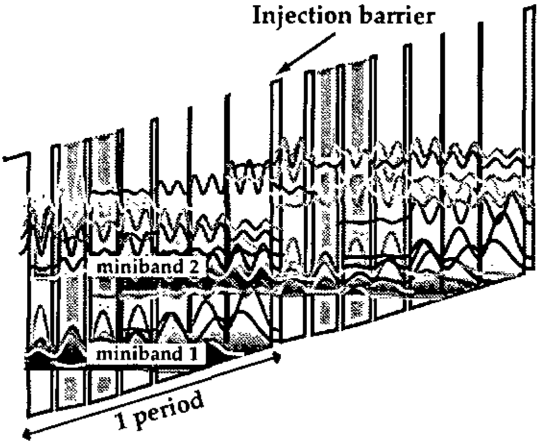

Figure 6.2: Self-consistent energy band diagram of two periods of the AlGaAs/GaAs structure A2432/A2433 under an average applied electric field of 4.2 kV/cm. The doped wells are shown in gray. The layer sequence of one period of structure, in nanometers, left to right and starting from the injection barrier is **4.0**/18.6/**0.8**/15.4/**0.6**/13.6/**2.3**/12.8/**1.8**/11.8/**2.3**/10.8/**3.2**/10.4/ where $Al_{15}Ga_{85}As$ layers are in bold, $GaAs$ in Roman and underlined numbers correspond to the doped region ($Si, 3.9 \times 10^{10} cm^{-2}$). One period of the structure is 108.4 nm long.

the injected current. The optical power rises linearly to a current density of $j = 90Acm^{-2}$ where a negative differential resistance (NDR) occurs. This linear dependence suggests that electron-electron scattering is not as effective in a superlattice as it is in vertical transition structure and is not a limiting factor. The operating region of the sample extends from an applied bias of $V = 0.6V$ to $V = 0.9V$ corresponding to an electric field of $F = 1.1kVcm^{-1}$ and $F = 1.7kVcm^{-1}$, slightly lower than the designed operating bias of $V = 1.1V$.

Spectral measurements of the luminescence were performed using the Nicolet 800 FTIR set-up in the step-scan mode. A few representative spectra taken for increasing injected

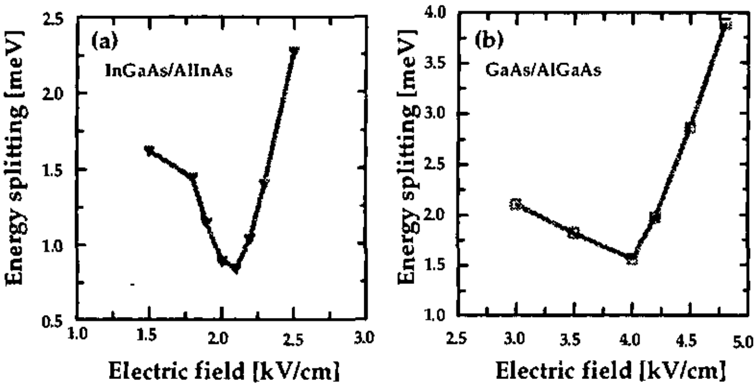

Figure 6.3: Computed splitting energy between the ground state of the injector and the upper state of the transitions versus applied field is shown for the InGaAs (a) and GaAs (b) superlattice designs.

currents at T=10K are displayed in Fig. 6.5. They show that the luminescence spectrum mainly consists of one main peak centered at a photon energy of 15meV. This peak is slightly red-shifted in energy 1.4 meV away from the expected energy corresponding to inter-mini-band transition in the active region. X-ray diffraction data exhibit a higher indium concentration than expected resulting in lowering the barrier potential and thus lowering the energy of the levels, in accordance to our observation. This could also explain the low operating bias of the structure. The FWHM is measured to be 2.1meV, independent of the injected current. This is almost a factor 2 larger that the one observed from the vertical transition (1.1meV). This may come from an increased effect of the interface roughness as the electronic wavefunction spreads over three wells. Increasing the injected current increases the peak intensity. Beyond the NDR, in contrast to the extremely broad optical spectrum

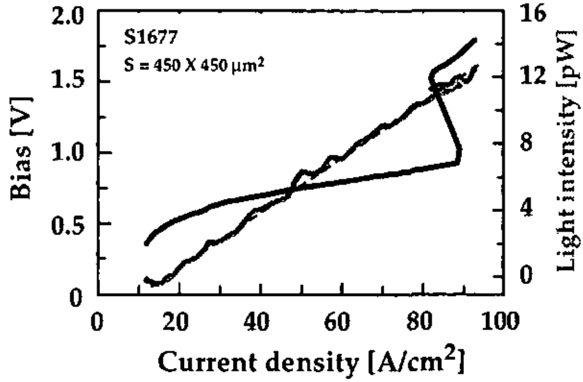

Figure 6.4: Luminescence intensity and applied bias versus injected current at T=10K for sample S1677 is shown (InGaAs/AlInGaAs).

observed on the vertical transition, the peak is still present,(Fig. 6.5 @ $99Acm^{-2}$) but with less intensity, showing that injection into the mini-band is still possible, but with reduced efficiency. We clearly observe that a tail is present on the low energy side of the peak. Such a tail is also observed with increasing current injection in the mid-infrared from luminescence spectra of a superlattice.[96] In contrast to our situation, this tail is on the high energy side of the peak, originating from carriers injected into higher states of the mini-band. These carriers perform a radiative transition before relaxing to the bottom of the lower mini-band. In our case, the tail must result from black-body emission due to sample heating. Figure 6.6 show temperature dependent measurements that have been done at constant injection current density ($j = 76Acm^{-2}$) up to T= 110K. As the temperature is raised, we observe a decrease of the intensity of the main peak. The integrated peak intensity at FWHM plotted versus inverse heat sink temperature is fitted to the data with an exponential function

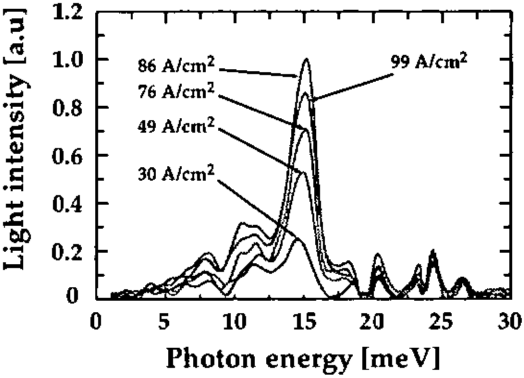

Figure 6.5: Spectral emission from the AlInAs/InGaAs chirped superlattice for increasing injected current densities.

and exhibits an activation energy of $E_a = 10.2meV$ (Fig. 6.6). As previously observed in the vertical transition structures, with raising temperature the electron gain excess kinetic energy and can relax to the lower miniband through emission of an optical phonon. The width of the lower miniband in the three well active region being $\Delta E = 9meV$, the sum of the miniband width in the active region, of the activation energy and of the emission energy is $\Delta E_{tot} \approx 34meV$ corresponding very well with the optical phonon energy ($E_{ph} = 33meV$).

The AlGaAs/GaAs samples A2433 was grown with the elementary cell repeated 120 times. The upper contact and mode confinement layer consist, in contrast to the vertical samples, of an MBE *in situ* grown aluminum layer. This was done to optimize the electrical contact and reduce the waveguide losses with a very clean interface. The sample processing consisted only in etching the waveguides. Figure 6.7 shows light and bias versus injected current density for waveguide length of $L = 880\mu m$ and $L = 220\mu m$. The bias versus injected

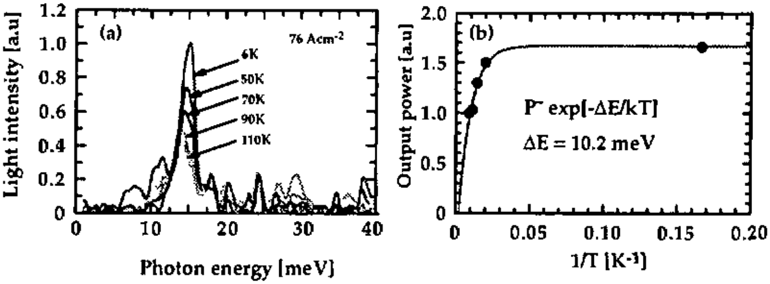

Figure 6.6: (a)Spectral emission from the AlInAs/InGaAs chirped superlattice for an injected current of $76Acm^{-2}$ and increasing heat sink temperature. (b) Activation graph of the integrated peak intensity at the FWHM with inverse temperature. The data is fitted with a decreasing exponential with an activation energy $\Delta E = 10.2meV$.

current density becomes linear with an applied bias of $V = 5.2$ volts corresponding to the expected electric field of $F = 4.0kVcm^{-1}$. This linearity stops with an applied bias of $b \approx 8V(F = 6kVcm^{-1})$ corresponding to an injected current density of $j \approx 750kAcm^{-2}$. The emission power increases non-linearly for the $L = 880\mu m$ samples and linearly for the $L = 220\mu m$ long waveguide up to an injected current density of $j \approx 750Acm^{-2}$. Beyond this current density, the intensity increases non-linearly. Due the high injection currents, low duty-cycles of respectively 7.5% and 10% were used to minimize heating and for limited available power reasons. To understand the nature of the dramatic increase of the intensity, spectral measurements have been performed for both waveguide lengths and are presented in Fig. 6.8. They have been normalized to a common arbitrary duty cycle of 1% to preserve relative spectral intensities. However, due to sample heating, integrated intensities are not relative to each other and do not correspond to what would have truly been measured at 1% duty cycle. All spectra show an emission peak centered at the photon energy of

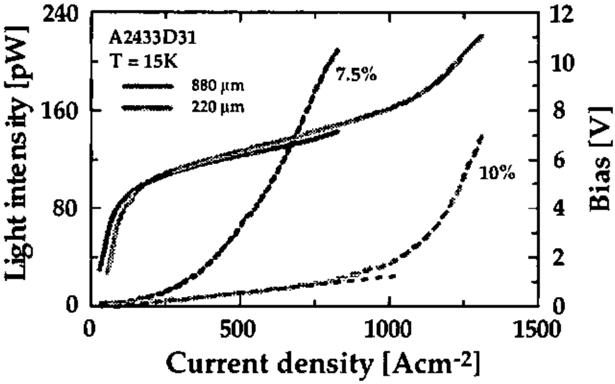

Figure 6.7: Light (dashed) and applied bias (plain) are plotted versus injected current density for sample 2433 at T = 15K. The measurements were performed at respectively 7.5% and 10% duty cycle for $880\mu m$ and $222\mu m$ long waveguides.The waveguide width of the samples is $l = 500\mu m$.

$h\nu = 18.5meV$ as expected from the structure design. We also see that the peaks are sitting on top of a broad emission due to sample heating. This heating is very important in these samples as it represent more than 80% of the total emission power. On the L = $200\mu m$ long sample we observe that a high energy tail appears with increasing injection current densities, suggesting the presence of hot carriers performing a transition to the lower miniband with a cut-off near 30meV as similar effect is reported in the mid infrared.[96] But no clear conclusion can be made as the apparent cut-off of the shoulder corresponds to a spectral minima of sensitivity of the detector. The increase of intensity of the low energy side shoulder suggests rather black-body emission from sample heating, which also supports the strong non linear increase of the intensity observed in Fig. 6.7. The integrated peak intensity where the black-body has been removed is shown in Fig 6.9(a) versus injected current density.

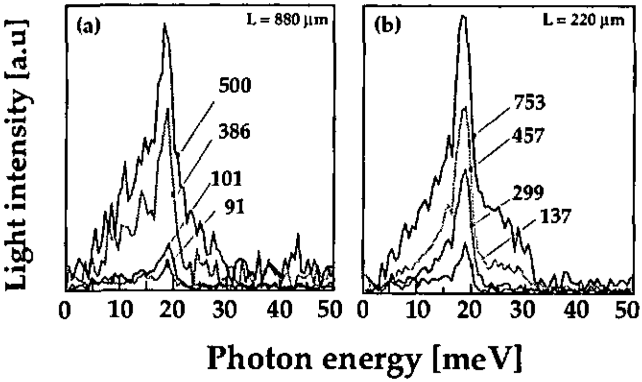

Figure 6.8: Spectral emission for L= $880\mu m$ (a) and L = $220\mu m$ (b). Current densities are given in Acm^{-2}. The spectra are presented normalized to a common duty cycle of 1% to preserve relative spectra intensities. However, due to sample heating, integrated intensities are not relative to each other and do not correspond to what would have been measured at 1% duty cycle.

The peak intensity in greater for the L=$880\mu m$ sample than for the L=$220\mu m$ long sample. Close to laser threshold, the waveguide is transparent and the output power should be at least proportional to the sample length. We however observe less than a factor of two increase of the output power with a four times longer waveguide. This is slightly better to what is observed with the vertical transition samples and a similar waveguide(see figure 5.9) suggesting higher gain. Unfortunately higher statistics is necessary to apply the same technique in order to evaluate the gain.

The FWHM of the emission peak are shown in figure 6.9 for waveguide length of L= $880\mu m$ and L = $220\mu m$ versus injected current density. A base line has been subtracted from the emission spectra before measuring the FWHM of the peaks as the spectra clearly contain

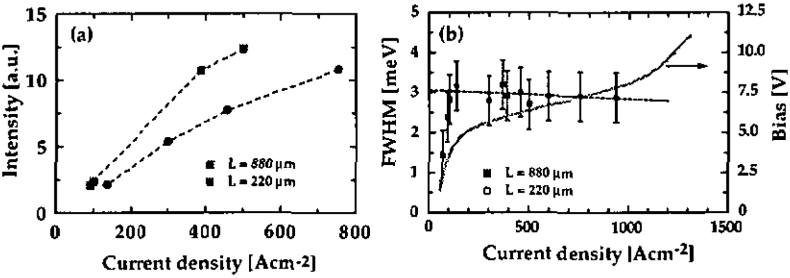

Figure 6.9: (a) The integrated peak intensity where the black-body emission is removed are plotted versus injected current.(b) FWHM of the emission peak are shown versus injected current density. A base line has been subtracted from the emission spectra before measuring the *FWHM* of the peaks. *Without the base line suppression, the FWHM has a linear increase* with injected current.

an important contribution from black-body emission. Without the base line suppression, the FWHM has a linear increase with injected current. The *I-V* curve of the sample is also shown. The FWHM increases strongly up to 3meV at the operating bias of the structure, and then have a slight decrease with injected current.However no clear difference is observed between the two length . A slight narrowing is observed with increasing current density for both samples. This decrease seems to be more pronounced for the long waveguide. Clear conclusions on the cause of this small effect cannot be made as the errors bars are relatively important. Furthermore, the heating is dominating the emission spectra and may reduce the performances of the device. Further exploration of this type of sample structure is required as the observation of far-infrared emission is possible with a chirped superlattice. Monte-Carlo simulations performed on a very similar structure predict a gain coefficient of $31cm^{-1}$ [99]. Considering obtained waveguide losses obtained in section 5.3, a reduction of the waveguide

Table 6.1: The overlap, loss and Γ/α parameter have been computed for various waveguide geometries with the same active region thickness (AR) and for various Semi-Insulating GaAs thicknesses. The reported thicknesses correspond to the highest Γ/α value.

	Waveguide	SI GaAs Thickness $[\mu m]$	Γ [%]	α $[cm^{-1}]$	Γ/α $[\% cm^{-1}]$
(a)	SIGaAs-AR-SIGaAs	500	7	0.6	11.7
(b)	Metal-AR-SIGaAs-Air	100	30	3.4	8.8
(c)	Metal-AR-SIGaAs-Metal	250	22	2.6	8.5
(d)	Metal-AR-Metal	-	100	13.5	7.4
(e)	Metal-AR-n^+GaAs	-	100	46.0	2.2

loss has to be achieved to reach laser action.

As discussed in chapter 5, a parameter characterizing the efficiency of a waveguide is given by the ratio Γ/α of the overlap factor and the waveguide losses. The double plasmon waveguide has the advantage to have a unity overlap factor and the disadvantage of relatively high losses compared to the double metal waveguide. This approach was used for technological reasons and the experience shows that it's performances are insufficient to obtain laser threshold with the available far-infrared active regions. The Γ/α parameter has been computed for various waveguide configuration for an identical active region. The results are presented in table 6.1. The simulations have been performed for a far-infrared radiation at $\lambda = 67\mu m$ and assuming zero losses in the semi-insulating GaAs. They show that configuration (a) is the best even with an overlap factor of only $\Gamma = 7$ % due to the very low waveguide losses. This configuration requires to have thick semi-insulating GaAs cladding on both sides of the active region. This configuration was rejected at due to the impossibility to

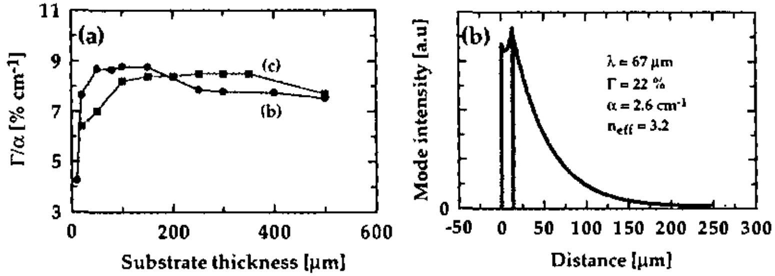

Figure 6.10: (a)Γ/α ratio plotted versus semi-insulating GaAs substrate thickness for configuration (b) and (c).(b)Mode profile versus sample thickness for waveguide configuration (c).

grow such a cladding and secondly due to the difficulty to contact the active region. The easiest configuration is the double plasmon waveguide (d) but it is also the one with smallest Γ/α factor, even with a 100% overlap. However, increasing the bottom doped layer of one order magnitude to $n = 5 \times 10^{19} cm^{-3}$ would bring down the losses to $\alpha = 17 cm^{-1}$ close to the metal-active region-metal configuration (d). Unfortunately such doping levels cannot be reached in GaAs. Configuration (b) and (c) have very similar properties (Fig. 6.10 but are not equally easy to process. The difficulty of configuration (a) is suppressed by having a top metal layer to confine the wave and the use of a the semi-insulating GaAs substrate to carry the wave. This configuration has very small computed waveguide loss as most of the wave is in the undoped substrate. The overlap factor is relatively high compared to (a) leading to a $\Gamma/\alpha = 8.5$ for configuration (c). This configuration is much easier to process than configuration (b) as in the latter an air separation has to be left between the substrate and the sample holder. The only difficulty to process the waveguide in configuration (c)

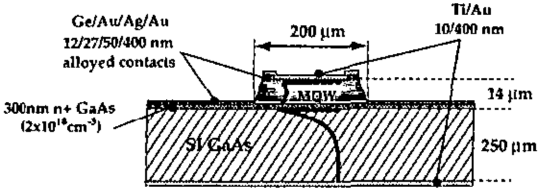

Figure 6.11: Schematics of the sample processing in configuration (c) of table 6.1.

is to etch the waveguide down to the highly doped 300nm thick contact layer separating the active region from the semi-insulating substrate (Figure 6.11). For the experiment, the samples were grown on semi-insulating GaAs (SIGaAs) wafers. The growth was initiated with a 300 nm highly doped $n = 2 \times 10^{18} cm^{-3}$ GaAs bottom contact layer followed by a parabolic grading to produce an abrupt carrier density profile. The active region is a chirped superlattice identical to sample A2433 shown in Fig. 6.2 doped with a nominal sheet density of $n_s = 4 \times 10^{10}$. The elementary cell is repeated 120 times. The structures continues with a 300nm parabolic grading and ends with a highly doped $n = 5 \times 10^{18}$ 80nm thick top contact layer. The sample is processed into waveguide etched down to the bottom contact layer. Two small $10 \mu m$ Ge/Au/Ag/Au alloyed contacts stripes are deposited on the top sided of the ridges. Evaporation of 10/400nm Ti/Au on top of the ridges provides the top confinement layer. The bottom Ge/Au/Ag/Au alloyed contact layer is then deposited. The substrate is then thinned down to $250 \mu m$ and polished before evaporation of a 10/400nm Ti/Au layer. The waveguides are then cleaved and soldered on a copper mount with indium.

The luminescence spectra of sample A2672L2 is shown in figure 6.12 (a). The emission

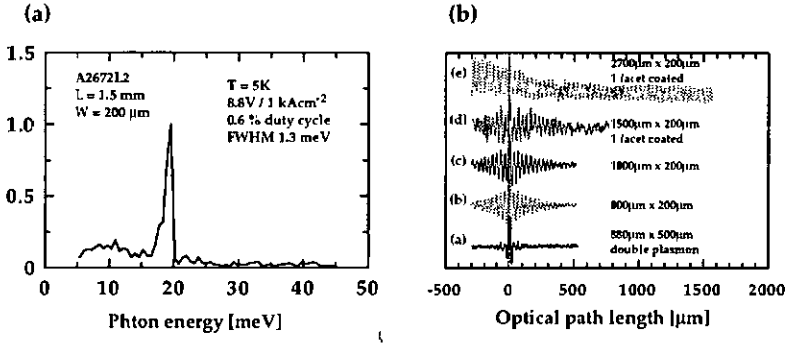

Figure 6.12: (a) Luminescence spectra obtained from a $200\mu m \times 1500\mu m$ long waveguide. (b) Obtained interferogram from a double plasmon waveguide (a) and from the (c) waveguide configuration of table 6.1 ((b)-(e)).

occurs at a photon energy of 19 meV. The integrated emission power is 30 pW with a duty-cycle of 0.6%. Similar average output power were observed from the double plasmon waveguide but with duty-cycles of 10% (fig. 6.7). Comparing the peak output power from the two waveguides of respectively 400pW and 5000pW for samples A2433 and A2672 with similar injected current densities clearly demonstrates the efficiency of the new waveguide configuration. Furthermore the emission spectra of the latter show reduced contribution of black body radiation to the total output power compared to sample A2433. The presence of gain is clearly observed as the emission linewidth has been reduced from 3meV to 1.3meV with the new waveguide. Very similar interferograms labeled (b) and (c) in figure 6.12(b) from respectively $L = 800\mu m$ and $L = 1500\mu m$ long waveguides show that the waveguide loss is not anymore the dominant loss source preventing the sample to reach laser threshold. The total mirror loss given by relation 6.2.1, where L is the cavity length and R the reflectivity

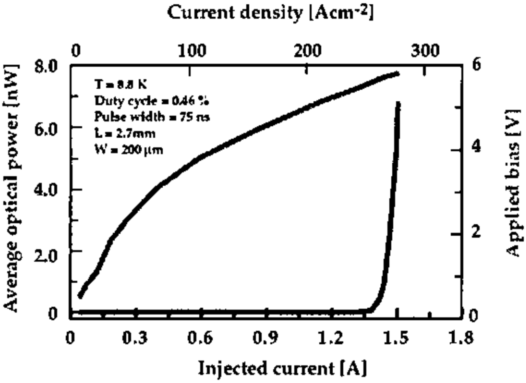

Figure 6.13: Light and bias versus injected current $(L - I - V)$ for sample A2672B42 is shown.

are computed to be respectively $\alpha_m = 32cm^{-1}$ and $17cm^{-1}$ for the $800\mu m$ and $1.5mm$ long waveguides.[24, 49] In order to reduce the mirror loss without increasing the current, one facet of the waveguide is HR coated with 100nm ZnSe used as insulator to prevent short circuits and 50nm of gold leading to a mirror reflectivity in the order of 95% reducing the waveguide mirror losses to $\alpha_m = 9cm^{-1}$ for the 1.5mm long waveguide. The linewidth of the luminescence was reduced to 1.1 meV as suggested from the longer oscillating interferogram labeled (d) in Fig. 6.12.

$$\alpha_m = -\frac{1}{L} ln(\sqrt{R_1 R_2}) \quad with\ R = (\frac{n_1 - n_2}{n_1 + n_2})^2 \tag{6.2.1}$$

Going one step further, a 2.7mm long waveguide with the identical facet coating has been processed reducing the mirror losses down to $\alpha_w = 5cm^{-1}$ allowing the the sample to reach

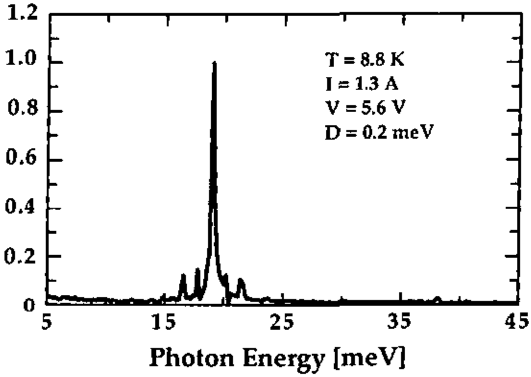

Figure 6.14: Step-scan of the laser emission. The resolution between two spectral points is 0.2 meV and do not allow us to resolve the peak. The interferogram is shown in figure 6.12(b) under label (e).

laser threshold at a current density of $j_{th} = 250Acm^{-2}$ at T = 8K (Fig. 6.13). The applied bias of 5.6V ($F = 4.3kVcm^{-1}$) corresponds well with the structure s designed operating value of $F = 4.0kVcm^{-1}$ (Fig. 6.3). An output power of 7nW was measured with 150 pulses 75ns long per period matched with the bolometer response at 413Hz. The overall duty-cycle is 0.46% leading to a peak output power of $P_{peak} \approx 1.5\mu W$. The peak material gain at threshold is estimated to be $G_p = (\alpha_w + \alpha_m)/\Gamma = 35cm^{-1}$. This value corresponds very well with the predicted value of $G_p = 31cm^1$ from Monte-Carlo simulations performed on a similar structure.[99] The spectral emission is shown in figure 6.14. It consist of a narrow peak centered at a photon energy of $h\nu = 19meV$ as expected from the structure design. Small peaks are present on each side of the main peak. These features are equally spaced with an energy difference of $\Delta\nu = 1.2meV$. These peaks are artefacts due the Fabry-Perot.

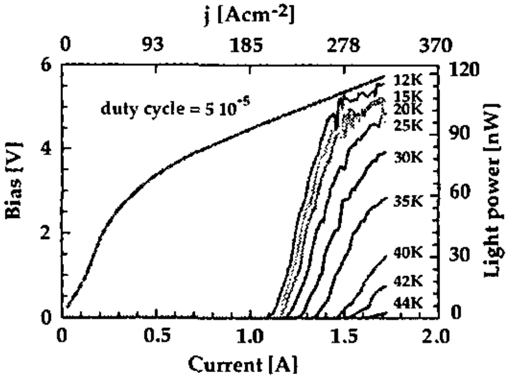

Figure 6.15: Temperature dependent $L-I$ curves.

resonances in the beam-splitter (Chapter 2.5). Temperature dependent measurements of the light output power versus injected current have been performed between 12K and the maximum operating temperature of 44K at a very low duty cycle of 5×10^{-5}. A threshold current density of $j_{th} = 210Acm^{-1}$ is observed at T=12k and $j_{th} = 300Acm^{-2}$ at T = 44k. At T=12K saturation of the gain is reached with a current density of $j = 315Acm^{-2}$. The average output power is $P_{avg} = 114nW$ leading to a peak power of $P_{peak} = 4.7mW$, taking into account that only half the power is transmitted trough the FTIR. With further optimization of the structure liquid nitrogen temperatures should be reached as the excess kinetic energy of the carriers at this temperature is one third of the optical transition energy. The very low threshold current density should also allow to obtain continuous wave operation of the device (CW). A structure based on the bound-to-continuum transition should increase the injection efficiency of the carriers and thus increase temperature performances.

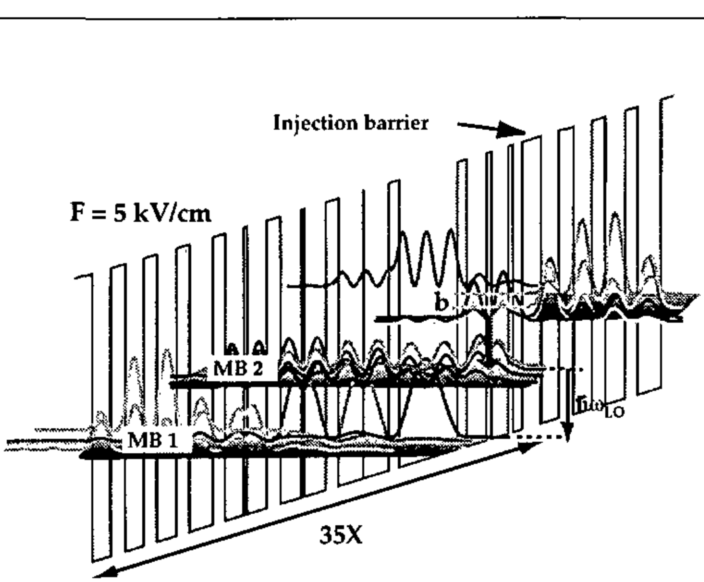

Figure 6.16: Energy band structure for sample A2567 in the GaAs/AlGaAs material system biased at $F = 5.0kV/cm$. The layer sequence in nanometers starting from the injection barrier is **6.0**/2.9/**1.4**/5.4/**1.5**/6.3/**3.0**/18.5/ **3.2**/8.0/**0.2**/7.8/**4.0**/6.8/ **0.9**/6.6/**4.5**/6.2/**1.0** /5.9/**4.0**/7.4/**4.0**/6.3/**4.2**/5.8/**4.7**/5.7/ where $Al_{0.15}As$ layers are in bold, $GaAs$ in Roman and underlined numbers correspond to the doped well (Si, n_s = $6.2 10^{10} cm^{-2}$).

6.3 Vertical Transition with an Optical Phonon

Pushing the concept of fast carrier extraction from the ground state of a far-infrared vertical transition, a structure taking the advantage of optical phonon emission has been designed. The energy band structure is shown in figure 6.16. The optical transition occurs between the state labeled b and mini-band 2. The optical transition energy is $h\nu = 23.3meV$ and has matrix element of $z_{if} = 4.9nm$. High energy far-infrared photon energy is chosen to push the excited state as far as possible to prevent optical phonon emission from the excited state to mini-band 1. The excited state and the ground state of the transition are localized in a well

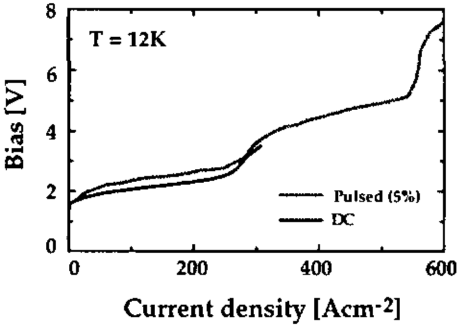

Figure 6.17: Bias versus injected current density is shown for a pulsed and a dc current. The first NDR occurs at a bias of b=2.5V corresponding very well with designed operating field of $F = 5kVcm^{-1}$.

with a small barrier in its center. The purpose of this small well is to be able to control the independently the energy of the excited state and the ground state. The energy difference of $h\nu = 37meV$ between the top of mini-band 2 and mini-band 1 allows emission of optical phonons. Two mini-bands have been used instead of one to prevent possible reabsorption of the photons from the structure

For the experiment, the structure was grown with the elementary cell repeated 35 times and processed into meas with a $15\mu m$ period grating for surface emission. Alloyed Ge/Au/Ag/Au contacts were deposited in top of the mesas. Figure 6.17 shows the bias versus injected current density obtained both for a pulsed (5% duty-cycle) and dc current injection a T = 12K. The structure aligns very quickly with an applied bias of $V \approx 2V$. A NDR occurs at $V \approx 2.5V$ and a second NDR occurs at higher voltage. The first NDR corresponds to the designed operating field of $F = 5kVcm^{-1}$.

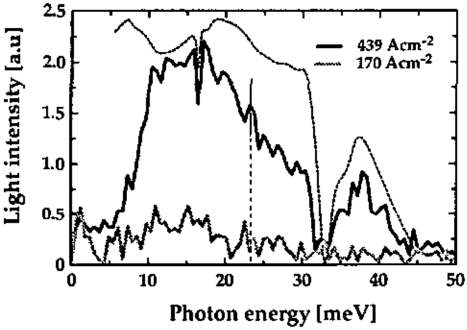

Figure 6.18: Spectra obtained for injected current densities above an before the first region of NDR. Vertical dashed line indicated the energy position of the expected intersubband transition. The other dashed line correspond to to the detector spectral responsivity on an arbitrary scale.

Spectral measurements have been performed both in the region below and above the first NDR. Before the NDR, a broad and weak emission is observe in the 10-20meV spectral region. As the current is increased above the NDR, the emission is much more intense but in neither cases a peak is observed at the expected photon transition (vertical dashed line). The observed broad emission is however attributed to black-body emission, filtered by the detector's responsivity (dashed line).

The absence of intersubband emission from this structure may be due to optical phonon emission from level b to top of mini-band 2 or to the bottom of mini-band 2 with $k \neq 0$ wave-vectors. Indeed at $k = 0$ this energy is $h\nu = 34meV$, very close to the phonon energy, thus explaining the very good carrier transport capabilities of the structure, but unfortunately also the missing intersubband emission. This effect could suppressed by removing the dispersion of the levels with application of a magnetic field.

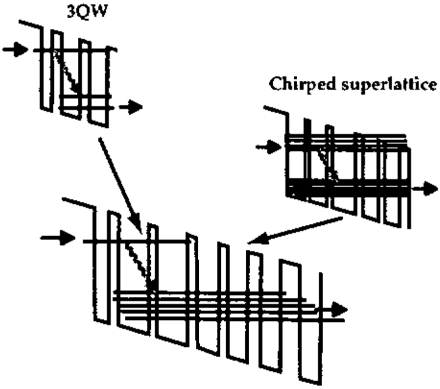

Figure 6.19: The bound-to-continuum structure takes advantage if the very efficient injection of the 3QW quantum cascade laser and the efficient extraction of the chirped superlattice design.

6.4 Long Wavelength Mid-IR Laser

When trying to design long wavelength quantum cascade lasers, for photon energies larger than the reststrahlen band, population inversion is more difficult to achieve as the upper state lifetime decreases with emitted photon energy, due to the dependence of the optical phonon scattering rate on exchanged wave-vector. The lower state lifetime, on the other hand, remains practically unchanged. For this reason, and especially if high temperature operation is sought, long wavelength QC lasers must be designed with extremely short lower state lifetimes. Transport in wide mini-bands, compared with the optical phonon energy, provides efficient lower state extraction mechanism. As the "bound–to–continuum" design combines the fast mini-band extraction from the lower state with the efficient resonant tunneling injection into the upper state, [93] this approach is very well suited for long wavelength

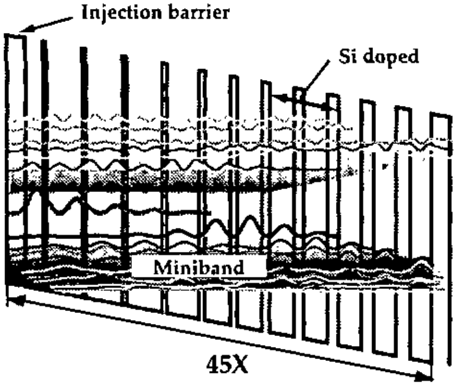

Figure 6.20: Schematic conduction band diagram of one stage of the structure under an applied electric field of $2.1 \times 10^4 Vcm^{-1}$. The moduli squared of the relevant wavefunctions are shown. The layer sequence of one period of structure, in nanometers, left to right and starting from the injection barrier is **3.3**/3.2/**0.5**/6.5/**0.6**/6.6/**0.7**/6.3/ 0.8/5.8/**1.0**/4.6/**1.2**/ 4.4/**1.4**/4.4/**1.7**/4.2/**2.0**/4.1/**2.2**/4.0/**2.5**/3.8/ where $In_{0.52}Al_{0.48}As$ layers are in bold, $In_{0.53}Ga_{0.47}As$ in Roman and underlined numbers correspond to the doped region $(Si, 3 \times 10^{17} cm^{-3})$.

lasers and perhaps could even allow an inrease of the performances of the far-infrared laser. As shown schematically in Fig.6.20, the active region of the structure spans the whole period and consists of a chirped superlattice presenting a tilted lower mini-band whose width is maximum in the center and decreases on both sides close to the injection barriers. The upper state is created in the mini-gap by a small well adjacent to the injection barrier. Its wavefunction has a maximum close to the injection barrier and decreases smoothly in the active region. This upper state is well-separated from the higher-lying states of the superlattice, lying in its first mini-gap and therefore does not need to be confined by separating the structure into an active region and an injection/relaxation region. The computed upper

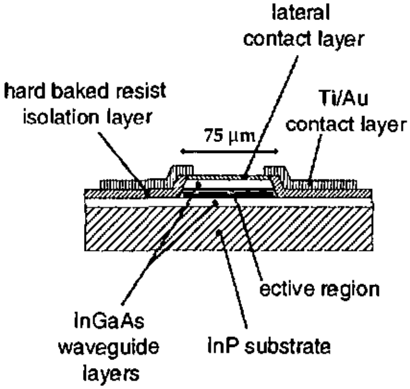

Figure 6.21: Skematics of the processing of the waveguide used for the experiment.

state lifetime $\tau_{up} = 0.68ps$, is longer than the one $\tau_{up} = 0.55ps$ computed for a chirped superlattice emitting at $\lambda = 17\mu m$.[94] This is due to the slightly diagonal nature of the laser transition which leads to a reduced overlap of the upper and lower state wavefunctions and leads to a further improved ratio of upper to lower state lifetimes.

Because of the reduced overlap between upper and lower laser state wavefunction, the equivalent dipole matrix element of the laser transition (averaged over the transitions to the two upper states of the lower mini-band)) is $z = 4.0nm$, lower than the value obtained for a chirped superlattice sample ($z = 5.0nm$).

The structure (S2018) was grown by Molecular Beam Epitaxy (MBE) using InGaAs and AlInAs alloys lattice matched on top of a very low n-doped InP substrate (Si, $n = 1 \times 10^{17} cm^{-3}$) and consist of a 45 period active region embedded in an optical waveguide. In contrast to the previous works, where extensive use of surface plasmon waveguide was made,

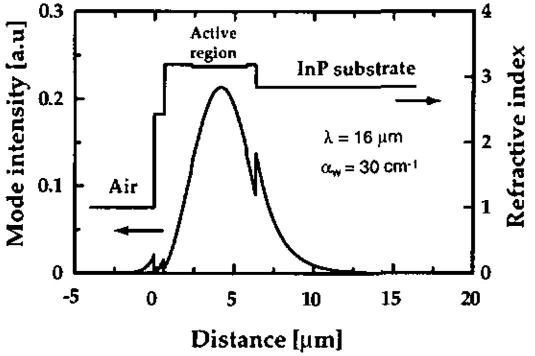

Figure 6.22: Refractive index and mode profile for the waveguide used for the long-wavelength laser. The air cladding has the advantage to allow to incorporate a gating into the waveguide.

[76] we chose a waveguide which relies on dielectric confinement (Fig. 6.22). It consists of two low doped (Si, $n = 6 \times 10^{16} cm^{-3}$) InGaAs guiding layers 600 and 1750nm thick, respectively grown below and above the active region. The computed waveguide absorption caused by free carriers is $\alpha = 30 cm^{-1}$, neglecting the contributions from multi-phonon processes. Electrical injection in the structure is obtained laterally through a heavily doped (Si, $n = 1 \times 10^{18} cm^{-3}$) 600nm thick InGaAs n-doped contact layer. The devices were processed in $50 - 75 \mu m$ wide mesa ridge waveguides using wet chemical etching and a hard baked resist layer for passivation. Contacts were then provided by a Ti/Au metalization (10/400 nm) on the top edges of the waveguides.[100] Back contacting (Ge/Au/Ag/Au, 12/27/50/100 nm) the thinned substrate ended the processing. The samples were then soldered with indium on a copper heat sink and mounted on a Peltier cooler inside an aluminum box with a ZnSe

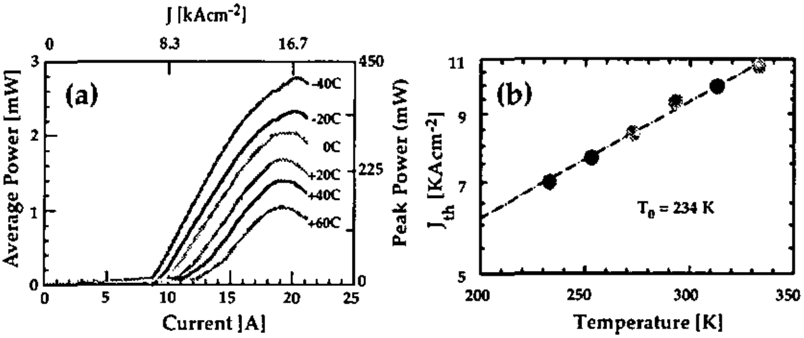

Figure 6.23: (a) Optical output power versus injected current in pulsed mode with a duty cycle of 0.67% at various temperatures for a device with a Fabry-Perot cavity. (b) Threshold current density as a function of temperature.

window. The electrical power was provided to the lasers with a commercial pulse generator (Alpes Lasers,TPG 128 pulser, and a LDD 100 power supply) delivering 25 to 50 ns long current pulses at a variable repetition rate up to 5 MHz. The optical output power was directly measured by a calibrated thermopile. Spectral measurements were performed by a Fourier transform infrared spectrometer in rapid scan mode and liquid-nitrogen cooled MCT detector. Typical *L-I* curves from a $75\mu m$ wide and $1.6mm$ long Fabry-Perot device are shown in Figure 6.23 for temperatures ranging from -40C up to 60C. The sample was driven with $25ns$ long current pulses and a duty cycle of 0.67%. At -40C the threshold current density is $6.7kAcm^{-2}$ with a maximum average output power 2.8 mW leading to a peak power of more than 400mW. At 60C, the threshold current density is $10kAcm^{-2}$ and the maximum output power is measured to be more than 1mW. At -40C, we achieved a maximum output power of 5.5 mW with 3% duty cycle and 1.2mW at 60C (1.5 % duty).

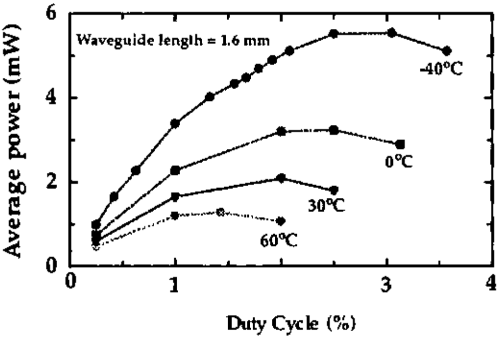

Figure 6.24: Maximum output power versus injected current duty cycle for various heat sink temperatures. The current was chosen to maximise the output power.

At -40C, the highest achieved duty cycle was 9.6 %. A fit to the threshold current density dependence with temperature (Fig. 6.23 (b)) using the usual expression $J = J_0 exp(T/T_0)$ yields a value of $T_0 = 234K$.[101]

The emission spectrum of this multi-mode device,(Fig.6.25(a)) consists mainly of modes around $644cm^{-1}$ ($\lambda \approx 15.5\mu m$). However weaker features around $607cm^{-1}$ ($\lambda \approx 16.5\mu m$) are also visible. They show that the gain curve of the device is broad (more than $40cm^{-1}$) and suggest the possibility to force the device to lase in this spectral region. Dotted line above the spectra represents the two-phonon absorption of InP on a linear arbitrary scale.[102] We clearly observe a correlation between the minima of the two phonon absorption and the lasing frequencies of our device. To demonstrate the possibility for our structure to lase in two spectrally distant regions, we have processed two series of samples with gratings etched ($\approx 0.5\mu m$) into the waveguide with periods designed to force waveguide modes at $\lambda \approx 16.5\mu m$ and $\lambda \approx 15.5\mu m$ [103]. An effective refractive index $n_{eff} = 3.001$ was used to compute the

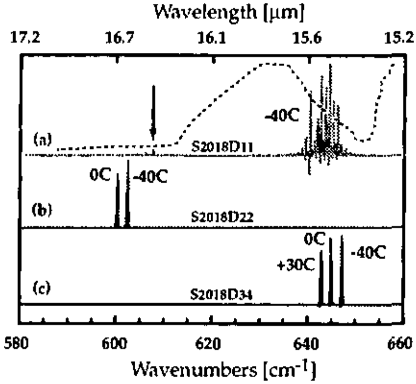

Figure 6.25: (a) Spectral emission from a device with a Fabry-Perot waveguide; (b) with a grating designed to force the lasing mode at $\lambda \approx 16.5\mu m$ and (c) with a grating designed for $\lambda \approx 15.5\mu m$. The dashed line is the two-phonon absorption line of InP on an arbitrary scale.

periodicity. Figure 6.25(b) displays the spectral measurements for the 1.5 mm long and 50 μm wide sample S2018D22. At -40C, the threshold current density is $7.0kAcm^{-2}$. Up to a an average power of P = 0.2mW , the emission is single frequency at $602cm^{-1}$ ($\lambda \approx 16.6\mu m$). However, as the driving current is increased further, side modes around the main peak at $602cm^{-1}$ build up and the peak at $647cm^{-1}$ reappear. A maximum (multi-mode) output power of 2.1 mW has been achieved. With increasing temperature, the peak redshifts from $602cm^{-1}$ down to $600cm^{-1}$ ($\lambda \approx 16.7\mu m$) at 0C. Results from sample S2018D34 are shown in Figure 6.25(c). At -40C, the emission peak is centered at $647cm^{-1}$ with a threshold current density of $6.1kAcm^{-1}$. Furthermore, at -40C, (Fig. 6.26 (b)), the emission is single mode up to an injected current density of $8.7kAcm^{-1}$ with an output power of P = 0.85 mW (64 mW peak). Increasing the injection current density up to $11kAcm^{-1}$ leads to a saturation of the

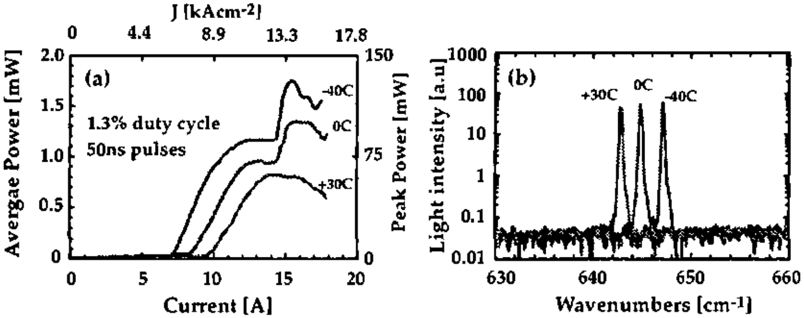

Figure 6.26: (a) $L-I$ curves with increasing temperature are shown for sample S2018D34. The sample is processed into a 2.250 mm long and 50 μm wide waveguide. (b) Spectral emission from sample S2018D34 plotted on a logarithmic scale,showing that the emission is single mode with a maximum output power 0.9 mW at -40C.

output power at 1.2 mW. At this current density, the emission consist of a single frequency peak around $647 cm^{-1}$ and a small feature at $638 cm^{-1}$. Increasing further the current, increases strongly the output power until the maximum output of 1.75 mW is reached. At this stage, the emission spectra is multi-mode and centered at $646 cm^{-1}$. At +30C, the emission is single mode up to the device's maximum operation capabilities with an average output power of P = 0.8 mW with a duty cycle of 1.3 %. The peak is redshifted down to $642 cm^{-1}$ leading to a temperature tuning $\frac{\Delta\nu}{\Delta T}$ of $-0.07 cm^{-1} K^{-1}$

Measurements done on 750 μm long structures show that the spectral emission is not single mode and suggest the need for a much stronger grating in order to achieve single mode laser operation for such short cavities. Similarly, higher power output in single mode operation should be achieved in the $600 cm^{-1}$ region with deeper etched gratings.

Chapter 7

Summary and Conclusion

In this work, the quantum cascade (QC) technology was used to explore far-infrared intersubband optical transitions. Intersubband far-infrared emission was demonstrated in the AlGaAs/GaAs and AlInAs/InGaAs material system with a vertical intersubband transitions using the quantum cascade electrical injection philosophy. Photon energies at $h\nu \approx 14meV$ with output emission power in the order of a few picowatts is observed. The emission full width at half maximum is very narrow between $\Delta\nu = 0.7meV$ and $\Delta\nu = 1.1meV$ respectively for the GaAs and the InGaAs material system. No difference in the performances of the GaAs and the InGaAs devices has been observed. Far-infrared emission has also been demonstrated with photon assisted transitions, but with much broader emission peaks, ranging from $\Delta\nu = 2.4meV$ with an injected current density $29.4Acm^{-2}$ up to $\Delta\nu = 12meV$ at $114Acm^{-2}$

At low temperature, the output power shows a square root dependence with injected current for the vertical transition structures. The excited state relaxation process is dominated by the carrier density dependent carrier-carrier scattering. At high temperature the output power becomes linear and activated optical phonon emission from carriers with excess kinetic energy becomes dominant with increasing temperature. Temperature dependant measurements allows to experimentally extract the scattering rates for the carrier-carrier scattering. The obtained values correspond very well with pump-probe experiments performed on similar structures.

In vertical far-infrared structures, due to the nature of the non-radiative scattering of the excited state, the gain is expected to decrease with increasing current injection. This unfortunately limits the operating range of such structures. The diagonal transition is a promising active structure for a FIR-QCL as the gain in such a structure is controlled by the injection barrier. However the broad full width a half maximum of the luminescence reduces strongly the gain. Graded interfaces in the active region could reduce significantly the FWHM of the emission and show enough gain for laser action

Waveguide based on the double plasmon electromagnetic wave confinement have been demonstrated in the far-infrared. Vertical structures have however not shown laser action. Gain measurement performed with a vertical structure with an optimized carrier extraction shows differential gain with injected current. This result suggest a gain coefficient of $g = 0.55 cmA^{-1}$. But due experimental imprecision, clear demonstration of gain has not been obtained. Other signs of gain have been sought by looking at emission peak narrowing as expected to happen close to laser threshold. Emission peak narrowing with injected current, cavity length and an applied magnetic field have been performed. Narrowing has been observed but not identified to be caused by gain in the structure. Waveguide loss measurements based on the single-pass multi section technique has however demonstrated encouragingly low waveguide losses of $\alpha_w = 42cm^{-1}$, similar to the computed values. No edge-emission has however been observed from an AlInAs/InGaAs structure.

Experimental exploration of the first generation far-infrared quantum cascade structures suggest that laser action is in reach provided an increase of the gain of the active region or a reduction of the waveguide losses. Improvement of the structure design in the mid-infrared suggested that the gain could be greatly increased by the use of the a chirped superlattice as published simulations predict increased gain in such structures, but still lower than the measured waveguide loss of the double plasmon waveguide. A structure with much higher predicted gain based on optical phonon extraction has been been tested. Unfortunately no intersubband emission has been observed from the structure.

A new approach to the waveguide design allowed to reach very low loss waveguide by the use of an undoped semi-insulating substrate as lower cladding. The chirped superlattice active region was embedded into this new waveguide. Narrow luminescence was observed from the device suggesting that the mirror losses were the main barrier to achieve laser threshold. Finally, a long waveguide together with a high reflecting coating deposited on one facet allowed to reduce sufficiently the loss and reach laser action at $\lambda = 67\mu m$ with a threshold current density of $j \approx 210A cm^{-2}$ at T = 12K. The peak measured output power is more than $P_{peak} = 4mW$. The gain at threshold is estimated to be $G_p = 35cm^{-1}$ and the maximum operating temperature is T = 44K.

In the mid-infrared, a structure based on the bound-to-continuum allowed to reach laser threshold above room temperature at $\lambda = 16.5\mu m$ with high output power demonstrating the possibility of high performance laser with new structure design a long wavelengths. This suggests that performances of far-infrared QCL could greatly be enhanced using the similar design philosophy and operation of far-infrared laser at liquid nitrogen temperature should be achievable. At this temperature the carrier excess kinetic energy is $E_{kT} = 6.6meV$, smaller than the optical transition energy of our devices. Reaching liquid nitrogen operating temperatures with far-infrared laser would allow commercial applications of such devices to be developed and open new roads for spectroscopy and telecommunications.

Bibliography

[1] A. Einstein. *Phys.Z.*, 18(121), 1917.

[2] T.H. Maiman. Stimulated radiation in ruby masers. *Nature*, 187, 1960.

[3] S. M. Sze. Modern semiconductor physics. *John Willey and Sons, Inc.*, (ISBN 0-471-15237-4), 1997.

[4] D. Hofstetter, M. Beck, J. Faist, M. Ngele, and M. W. Sigrist. Photoacoustic spectroscopy with quantum cascade distributed-feedback lasers. *Optics Letters*, 26(12), 2001.

[5] S. Blaser, D. Hofstetter, M. Beck, and J. Faist. Free-space optical data link using peltier-cooled quantum cascade laser. *Electronics Letters*, 37(12), 2001.

[6] A. Muller, M. Beck, J. Faist, R. Schindler, H. Elmoser, and B. Lendl J.-P. Pellaux. Novel quantum cascade laser based measurements of chemicals in liquid and gases with 50 fold improved signal to noise ratio. *99 Sensors Expo*, 1999.

[7] K. Unterrainer and C. Kremser E. Gornick C.R. Pigeon Yu. L. Ivanov E.E. Haller. *Tunable cyclotron resonance laser in germanium.* *Physical Review Letters*, 64(19), 1990.

[8] V. Swaminathan and A.T. Macrander. Materials aspects of gaas and inp based structures. *Prentice Hall Advanced Reference Series*, (ISBN 0-13-346826- 7), 1991.

[9] R.F Kazarinov and R.A. Suris. Possibility of the amplification of electromagnetic waves in a semiconductor with a superlattice. *Soviet Physics- semiconductors*, 5(4), 1971.

[10] Tsuneya Ando, Alan B. Fowler, and Frank Stern. Electronic properties of two-dimensional systems. *Review of Modern Physics*, 54(2), 1982.

[11] Kevin Daniel Maranowski. Parabolically graded semiconductor quantum wells for emission of far-infrared radiation. *Ph.D. Thesis, University of California Santa Barbara USA*, 2000. maranowski.

[12] L.C. West and S.J. Eglash. First observation of an extremely large-dipole infrared transition within the conduction band of a GaA quantum well. *Applied Physics Letters*, 46(12), 1985.

[13] A. Cho. Molecular beam epitaxy. *AIP Press Woodbury, NW*, 1994. cho.

[14] M. Helm, E. Colas, P. England, F. DeRosa, and S.J. Allen Jr. Observation of grating-induced intersubband emission from GaAs/AlGaAs superlattices. *Applied Physics Letters*, 53(18), 1988.

[15] M.Helm, P.England E.Colas, F. DeRosa, S.J Allen, and Jr. Intersubband emission from semiconductor superlattices excited by sequential resonant tunneling. *Physical Review Letters*, 63(1), 1989.

[16] Federico Capasso, Khalid Mohammed, and Alfred Y. Cho. Resonant tunneling through double barriers, perpendicular quantum transport phenomena in superlattices, and their device applications. *IEEE Journal of Quantum Electronics*, 22(9), 1986.

[17] W.M Yee and K.A. Shore. Threshold current density calculations for far-infrared semiconductor lasers. *Semicond. Sci. Technol.*, 9, 1994.

[18] Jurgen H. Smet, Clifton G. Fonstad, and Qing Hu. Intrawell and interwell intersubband transitions in multiple quantum wells for far-infrared sources. *Journal of Applied Physics*, 79(12), 1996.

[19] Shmuel I. Borenstain and Joseph Katz. Evaluation of the feasibility of a far-infrared laser based on intersubband transitions in GaAs quantum wells. *Applied Physics Letters*, 55(7), 1989.

[20] Qing Hu and Shechao Feng. Feasibility of far-infrared lasers using multiple semiconductor quantum wells. *Applied Physics Letters*, 59(23), 1991.

[21] Vincent Berger. Three-level laser based on intersubband transitions in asymetric quantum wells : a theoretical study. *Semicond. Sci. Technol.*, 9, 1994.

[22] J. Faist, F. Capasso, C. Sirtori, D. Sivco, and A. Cho. Quantum cascade lasers. *Intersubband transitions in quantum wells: Physics and device applications II, edited by H. Liu and F. Capasso Academic Press*, 66(1), 2000.

[23] J. Faist, F. Capasso, C. Sirtori, D. L. Sivco, A. L. Hutchinson, S, N.G Chu, and A.Y. Cho. Quantum-well intersub-band electroluminescence at $\lambda = 5\mu m$. *Electronics Letters*, 29(25), 1993.

[24] Jérôme Faist, Federico Capasso, Deborah L. Sivco, Carlo Sirtori, Albert L. Hutchinson, and Alfred Y. Cho. Quantum cascade laser. *Science*, 264, 1994.

[25] Mattias Beck, Daniel Hofstetter, Thierry Aellen, Jérome Faist, Ursula Oesterle, Marc Ilegems, Emilio Gini, and Hans Melchior. Continuous wave operation of mid-infrared semiconductor laser at room temperature. *Science*, 295, 2002.

[26] Jérôme Faist, Federico Capasso, Deborah L. Sivco, Albert L. Hutchinson, Sung-Nee G. Chu, and Alfred Y. Cho. Short wavelength $\lambda \approx 3.4 \mu m$ quantum cascade laser based on strained compensated InGaAs/AlInAs. *Applied Physics Letters*, 72(6), 1998.

[27] Raffaele Colombelli, Federico Capasso, Claire Gmachl, Albert L. Hutchinson, Deborah L. Sivco, Alessandro Tredicucci, Michael C. Wanke, A. Michael Sergent, and Alfred Y. Cho. Far- infrared surface-plasmon quantum-cascade lasers at 21.5 μm and 24 μm wavelength. *Applied Physics Letters*, 78(18), 2001.

[28] K.D. Maranowski, A.C. Gossard K. Unterrainer, and E. Gornik. Far- infrared emission from parabolically graded quantum wells. *Applied Physics Letters*, 69(23), 1996.

[29] Bin Xu, Quing Hu, and Michael R. Melloch. Electrically pumped tunable terahertz emitter based on intersubband transitions. *Applied Physics Letters*, 71(4), 1997.

[30] Benjamin S. Williams, Bin Xu, Quing Hu, and Micheal R. Melloch. Narrow- linewidth terahertz intersubband emission from three-level systrems. *Applied Physics Letters*, 75(19), 1999.

[31] Michel Rochat, Jérôme Faist, Mattias Beck, Ursula Oesterle, and Marc Ilegems. Far-infrared($\lambda = 88 \mu m$) electroluminescence in a quantum cascade structure. *Applied Physics Letters*, 73(25), 1998.

[32] J. Ulrich and a) R. Zobl, W. Schrenk, G. Strasser, K. Unterrainer, and E. Gornik. Terahertz quantum cascade structures: Intra- versus interwell transition. *Applied Physics Letters*, 77(13), 2000.

[33] Stéphane Blaser, Michel Rochat, Mattias Beck, Jérôme Faist, and Ursula Oesterle. Far-infrared and stark-cyclotron resonances in a quantum cascade structure based on photon-assisted tunneling transition. *Physical Review B*, 61(12), 2000.

[34] K.-Y. Cheng. Molecular beam epitaxy technology of III-V compound semiconductors for optoelectronic applications. *Proceedings of the IEEE*, 85(11), 1997.

[35] G. Bastard. Wave mechanics applied to semiconductor heterostructures. *Les Edions de Physique*, (ISBN 0-470-21708-1), 1988.

[36] Barry L. Levine. *Journal of applied Physics*, 74, 1993.

[37] Jérôme Faist, Carlo Sirtori, Federico Capasso, Sung-Nee G. Chu, Loren N. Pfeiffer, and Ken W. West. Tunable fano interference in intersubband absorption. *Optics Letters*, 21(13), 1996.

[38] Jérôme Faist, Federico Capasso, Carlo Sirtori, Deborah L. Sivco, Albert L. Hutchinson, Sung-Nee G. Chu, and Alfred Y. Cho. Measurement of the intersubband scattering rate in semiconductor quantum wells by excited state differential absorption spectroscopy. *Applied Physics Letters*, 63(10), 1993.

[39] Jérôme Faist, Federico Capasso, Carlo Sirtori, Albert L. Hutchinson, Ken W. West, and Loren N. Pfeiffer. Intersubband emission in double-well structures with quantum interference in absorption. *Applied Physics Letters*, 71(24), 1997.

[40] C. Sirtori, F. Capasso, J. Faist, L.N. Pfeiffer, and K.W. West. Far-infrared generation by doubly resonant difference frequency mixing in a coupled quantum well two-dimensional electron gas system. *Applied Physics Letters*, 65(4), 1994.

[41] Manfred Helm. The basic physics of intersubband transitions. *Intersubband transitions in quantum wells: Physics and device applications II, edited by H. Liu and F. Capasso Academic Press.*

[42] Lian Zheng, W. L. Schaich, and A.H. MacDonald. Theory of two-dimensional grating couplers. *Physical Review B*, 41(12), 1990.

[43] Bin Xu and Quing Hu. Grating coupling for intersubband emission. *Applied Physics Letters*, 70(19), 1997.

[44] W. J. Li and B. D. Mc Combe. Coupling efficiency of metallic gratings for excitation of intersubband transitions in quantum-well structures. *Journal of Applied Physics*, 71(2), 1992.

[45] William P. Dumke. Quantum theory of free carrier absorption. *Physical Review B*, 124(6), 1961.

[46] Henry Mathieu. Physique des semiconducteurs et des composants électroniques. *Masson*, (ISBN 2-225-83151-3), 1998.

[47] Pallab Bhattachara. Properties of lattice-matched and strained indium gallium arsenide. *INSPEC*, (ISBN 0 85296 865 5), 1993.

[48] Sadao Adachi. Properties of aluminum gallium arsenide. *INSPEC*, (ISBN 0 85296 558 3), 1993.

[49] Amnon Yaiv. Quantum eletronics. *John Willey and Sons Inc.*, (ISBN 0-471-60997-8), 1998.

[50] John Morris. Silicon bolometer instruction manual. *Infrared Laboratories Inc.*, 1997.

[51] Frank J. Low. Low-temperature germanium bolometer. *Journal Opt. Soc. Am.*, 51(11), 1961.

[52] Jean Rossel. Physique générale. *Edition du Griffon, Neuchatel*, 1960.

[53] B. Diu, C. Guthmann, D. Lederer, and B. Roulet. Physique statistique. *Hermann*, 1989.

[54] J. Ulrich, R. Zobl, K. Unterrainer, G. Strasser, and E. Gornik. Magnetic field enhanced quantum cascade emission. *Applied Physics Letters*, 76(1), 2000.

[55] R. Ferreira and G. Bastard. Evaluation of some scattering times for electrons in unbiased and biased single- and multiple- quantum-well structures. *Physical Review B*, 40(2), 1989.

[56] M. Betz, G. Goedes, A. Leitenstorfer K. Ortner, C.R. Becker, G. Boehm, and A. Laudereau. Ultrafast electron-phonon scattering in semiconductors studied by nondegenerate four-wave mixing. *Physical Review B*, 60(16), 1999.

[57] Jérôme Faist, Federico Capasso, Carlo Sirtori, Deborah L. Sivco, Albert L. Hutchinson, Sung-Nee G. Chu, and Alfred Y. Cho. Narrowing of the intersubband electroluminescent spectrum in coupled-quantum well heterostructures. *Applied Physics Letters*, 65(1), 1994.

[58] Jérôme Faist, Federico Capasso, Carlo Sirtori, Debbie Sivco, Albert L. Hutchinson, Sung-Nee G. Chu, and Alfred Y. Cho. Mid-infrared field-tunable intersubband electroluminescence at room temperature by photon-assisted tunneling in coupled- quantum wells. *Applied Physics Letters*, 64(9), 1994.

[59] Jérôme Faist, Alessandro Tredicucci, Federico Capasso, Carlo Sirtori, Deborah L. Sivco, James N. Baillargeon, Albert L. Hutchinson, and Alfred Y. Cho. High-power continuous-wave quantum cascade lasers. *IEEE Journal of Quantum Electronics*, 34(2), 1998.

[60] J.N. Heyman, K. Unterrainer, K. Craig, J. Williams, M.S. Sherwin, K. Campman, P.F. Hopkins, A.C. Gossard, B.N. Mrdin, and C.J.M. Langerak. Far- infrared pump-probe measurements of the intersubband lifetime in an AlGaAs/GaAs coupled-quantum well. *Applied Physics Letters*, 68(21), 1996.

[61] Per Hyldgaard and John W. Wilkins. Electron-electron scattering in far-infrared quantum cascade lasers. *Physical Review B*, 53(11), 1996.

[62] M. Hartig, S. Haacke, P.E. Selbmann, B. Deveaud R.A. Taylor, and L. Rota. Efficient intersubband scattering via carrier-carrier interaction in quantum wells. *Physical Review Letters*, 80(9), 1998.

[63] G. Strasser, P. Kruck, M. Helm, J.N. Heyman, L. Hvozdara, and E. Gornik. Mid-infrared electroluminescence in GaAs/AlGaAs structures. *Applied Physics Letters*, 71(20), 1997.

[64] K.L. Campman, H. Schmidt, A. Imamoglu, and A.C. Gossard. Interface roughness and alloy-disorder scattering contributions to intersubband transition linewidths. *Applied Physics Letters*, 69(17), 1996.

[65] Jérôme Faist, Federico Capasso, Carlo Sirtori, Deborah L. Sivco, Albert L. Hutchinson, and Alfred Y. Cho. Laser action by tuning the oscillator strength. *Nature*, 387, 1997.

[66] M. Hartig, J.D. Ganiere, P.E. Selbmann, B. Deveaud, and L. Rota. Density dependance of carrier-carrier -induced intersubband scattering in GaAs/AlxGa(1-x)As quantum wells. *Physical Review B*, 60(3), 1999.

[67] Jérôme Faist, Federico Capasso, Loren Pfeiffer, and Ken W. West. Phonon limited intersubband lifetimes and linewidths in a two-dimensional electron gas. *Applied Physics Letters*, 64(7), 1994.

[68] S.M Goodnick P. Lugli. Effet of electron-electron scattering on nonequilibrium transport in quantum-well systems. *Physical Review B*, 37(5), 1988.

[69] Manfred Dur, Stephen M. Goodnick, Paolo Lugli, and Benoit Deveaud. Effect of intercarrier scattering on intersubband transitions in AlGaAs/GaAs quantum well systems. *Physica B*, (272), 1999.

[70] J. Ulrich, R. Zobl, K. Unterrainer, G. Strasser, E. Gornik K.D. Maranovski, and A.C. Gossard. Temperature dependence of far-infrared electroluminescence in parabolic quantum wells. *Applied Physics Letters*, 74(21), 1999.

[71] J.N. Heyman, K. Unterrainer, K. Vraig, B. Galdrokian, M.S. Sherwin, K. Campman, P.F. Hopkins, and A.C. Gossard. Temperature and intensity dependance of intersubband relaxation rates from photovoltage and absorption. *Physical Review Letters*, 74(14), 1995.

[72] Jérôme Faist, Federico Capasso, Deborah L. Sivco, Albert L. Hutchinson, Carlo Sirtori, Sung-Nee G. Chu, and Alfred Y. Cho. Quantum cascade laser: Temperature dependence of the performance characteristics and high t_0 operation. *Journal of Applied Physics*, 65(23), 1994.

[73] Carlo Sirtori, Jérôme Faist, Federico Capasso, Deborah L. Sivco, Albert L. Hutchinson, Sung-Nee G. Chu, and Alfred Y. Cho. Continuous wave operation of mid-infrared (7.4 - 8.6 μm) quantum cascade lasers up to 110k temperature. *Applied Physics Letters*, 68(13), 1996.

[74] Emmanuel Rosencher and Borge Vinter. Optoélectronique. *Masson*, (ISBN 2-225-82935- 7), 1998.

[75] Claude Cohen-Tannoudji, Bernard Diu, and Franck Laloe. Mécanique quantique tome 1. *Hermann*, (ISBN 2-7056-6074- 7), 1973.

[76] Carlo Sirtori, Claire Gmachl, Federico Capasso, Jérôme Faist, Deborah L. Sivco, Albert L. Hutchinson, and Alfred Y. Cho. Long-wavelength ($\lambda \approx 8 - 11.5 \mu m$) semiconductor lasers with waveguide based on surface plasmons. *Optics Letters*, 23(17), 1998.

[77] José-Philippe Pérez, Robert Carles, and Robert Fleckinger. Electromagnétisme vide et milieux matériels. *Masson*, (ISBN 2-225-82294-8), 1990.

[78] Jérôme Faist. Etude théorique et expérimentale de la modulation de phase dans les doubles hétérostructures GaAa/Al(x)Ga(1-x)As. *Ph.D. Thesis EPFL, Switzeland*, (776), 1989.

[79] Daniel Hofstetter. Monolithically integrated interferometer for optical displacement measurement. *Ph.D. Thesis UNINE, Switzerland*, 1996.

[80] Edward D. Palik. Handbook of optical constants of solids.

[81] Michel Rochat, Mattias Beck, and Jérôme Faist Ursula Oesterle. Measurement of far-infrared waveguide loss using a multisection single-pass technique. *Applied Physics Letters*, 78(14), 2001.

[82] Alessandro Tredicucci, Claire Gmachl, Michael C. Wanke, Federico Capasso, Albert L. Hutchinson, Deborah L. Sivco, Sung-Nee G. Chu, and Alfred Y. Cho. Surface plasmon quantum cascade laser at $\lambda \approx 19\mu m$. *Applied Physics Letters*, 77(15), 2000.

[83] P. Bakshi, K. Kempa, A. Scorupsky, C.G. Du, G. Feng R. Zobls, G.Strasser, C. Rauch, Ch. Pacher, K. Unterrainer, and E. Gornik. Plasmon-based terahertz emission from quantum well structures. *Applied Physics Letters*, 75(12), 1999.

[84] Alessandro Tredicucci. *private communication.*

[85] Daniel T. Cassidy. Technique for measurement of the gain spectra of semiconductor diode laser. *Journal of Applied Physics*, 56(11), 1984.

[86] Basil W. Hakki and Thomas L. Paoli. Gain spectra in GaAs double-hetrostructure injection lasers. *Journal of Applied Physics*, 46(3), 1975.

[87] Daniel Hofstetter and Jérôme Faist. Measurements of semiconductor laser gain and dispersion curves utilizing fourier transforms of the emission spectra. *IEEE Photonics Technology Letters*, 11(11), 1999.

[88] J.D. Thomson, H.D. Summers, P.J. Hulyer, P.M. Smowton, and P. Blood. Determination of single-pass optical gain and internal loss using a multisection device. *Applied Physics Letters*, 75(17), 1999.

[89] Alexander Blank and Shchao Feng. Suppression of intersubband nonradiative transitions by a magnetic field in quantum well laser devices. *Journal of Applied Physics*, 74(7), 1993.

[90] Jérôme Faist, Federico Capasso, Carlo Sirtori, Deborah L. Sivco, James N. Baillargeon, Albert L. Hutchinson, Sung-Nee G. Chu, and Alfred Y. Cho. High power mid-infrared ($\lambda \approx 5\mu m$) quantum cascade lasers operating above room temperature. *Applied Physics Letters*, 68(26), 1996.

[91] Jérôme Faist, Carlo Sirtori, Federico Capasso, Deborah L. Sivco, James N. Baillargeon, Albert L. Hutchinson, and Alfred Y. Cho. High-power long- wavelength ($\lambda \approx 11.5 \mu m$) quantum cascade lasers operating above room temperature. *IEEE Photonics Technology Letters*, 10(8), 1998.

[92] C. Gmachl, F. Capasso, A. Tredicucci, D. L Sivcom A.L. Hutchinson, and A. Y. Cho. Long wavelength ($\lambda = 13 \mu m$) quantum cascade laser. *Electronics Letters*, 34(11), 1998.

[93] Jérôme Faist, Mattias Beck, Thierry Aellen, and Emilio Gini. Quantum-cascade lasers based on a bound-to-continuum transition. *Applied Physics Letters*, 78(2), 2001.

[94] Alessandro Tredicucci, Claire Gmachl, Federico Capasso, Deborah L. Sivco, Albert L. Hutchinson, and Alfred Y. Cho. Long vavelength superlattice quantum cascade lasers at $\lambda = 17 \mu m$. *Applied Physics Letters*, 74(5), 1999.

[95] Alessandro Tredicucci, Claire Gmachl, Federico Capasso, Albert L. Hutchinson, Deborah L. Sivco, and Alfred Y. Cho. Single-mode surface-plasmon laser. *Applied Physics Letters*, 76(16), 2000.

[96] Gaetano Scamarcio, Federico Capasso, Jérôme Faist, Carlo Sirtori, Deborah L. Sivco, Albert L. Hutchinson, and Alfred Y. Cho. Tunable interminiband infrared emission in superlattice electron transport. *Applied Physics Letters*, 70(14), 1997.

[97] Gaetano Scamarcio, Federico Capasso, Carlo Sirtori, Jérôme Faist, Albert L. Hutchinson, Deborah L. Sivco, and Alfred Y. Cho. High-power infrared (8 - micrometer wavelength) superlattice lasers. *Science*, 276, 1997.

[98] Alessandro Trediducci, Federico Capasso, Claire Gmachl, Deborah L. Sivco, Albert L. Hutchinson, and Alfred Y. Cho. High performance interminiband quantum cascade lasers with graded superlattices. *Applied Physics Letters*, 73(15), 1998.

[99] Ruedegger Koehler, Rita C. Iotti, Alessandro Tredicucci, and Fausto Rossi. Design and simulation of Thz Quantum Cascade Lasers. *Applied Physics Letters*, 79(24), 2001.

[100] Daniel Hofstetter, Jérôme Faist, Mattias Beck, and Antoine Mueller Ursula Oesterle. Demonstration of high-performance 10.16 μm quantum cascade distributed feedback lasers fabricated without epitaxial regrowth. *Applied Physics Letters*, 75(14), 1999.

[101] Panhove. *IEEE J.Q.Electronics*, QE4, 1968.

[102] E. S. Koteles and W. R. Datars. Two-phonon absorption in inp and gap. *Solid State Communications*, 19, 1976.

[103] Daniel Hofstter, Thierry Aellen, Mattias Beck, and Jérôme Faist. High average power first-order distributed feedback quantum cascade lasers. *IEEE Photonics Technology Letters*, 12(12), 2000.

Index

Appendix A

Publications

- **M. Rochat**, J. Faist, M. Beck, U. Oesterle, M. Ilegems
  Far-Infrared ($\lambda = 88\mu m$) electroluminescence in a quantum cascade structure. Appl. Phys. Lett., vol. 73, no. 25, pp. 3724-3726, 1998

- S. Blaser, **M. Rochat**, M. Beck, J. Faist, U. Oesterle
  Far-infrared and Stark-cyclotron resonances in a quantum cascade structure based on photon-assisted tunneling transition. Phys. Rev. B, vol. 61, no. 12, pp 8369-8374, 2000

- **M. Rochat**, J. Faist, M. Beck, U. Oesterle
  Electrically pumped Terahertz quantum well sources. Physica E, vol. 7, issue 1-2, pp. 44-47, 2000

- **M. Rochat**, M. Beck, J. Faist, U. Oesterle
  Measurement of far-infrared waveguide loss using a multisection single-pass technique. Appl. Phys. Lett., vol. 78, no. 14, pp. 1967-1969, 2001

- S. Blaser, **M. Rochat**, L. Ajili, M. Beck, J. Faist, H. Beere, G. Davies, E. Linfield, D. Ritchie
  Terahertz interminiband emission and magneto-transport measured from a quantum cascade chirped superlattice. Physica E **13**, 854–857 (2002)

- **M. Rochat**, D. Hofstetter, M. Beck, J. Faist
  Long-wavelength ($\lambda = 16\mu m$), room-temperature, single-frequency quantum cascade lasers based on a bound-to-continuum transition. Appl. Phys. Lett., vol. 79, no 26, pp.4271-4273, 2001

- J. Faist, D. Hofstetter, M. Beck, T. Aellen, **M. Rochat**, and S. Blaser
  Bound-to-continuum and two-phonon resonance quantum cascade lasers for high duty cycle, high temperature operation. IEEE J. Quantum Electron, vol 38,–, 2002

- S. Blaser, **M. Rochat**, M. Beck, D. Hofstetter, and J. Faist
  Terahertz intersubband emission in strong magnetic fields. Appl. Phys. Lett., vol 81, no 1, 2002

- **M. Rochat**, H. Willenberg, L. Ajili, M. Beck, J. Faist, H. Beere, G. Davies, E. Linfield, D. Ritchie
  Low Threshold Terahertz Quantum Cascade Lasers. Appl. Phys. Lett., vol 81, no 2, pp. 1381-183, 2002

- A.A. Kosterev, R.F. Curl, F.K. Tittel, **M. Rochat**, M. Beck, D. Hofstetter, J. Faist
  Chemical sensing with pulsed QC-B lasers operating at 15.6μm. Appl. Phys. B, (2002)

Appendix B

Contributions

- **M. Rochat**,J. Faist, M. Beck, U. Oesterle, M. Illegems
  Electrically Pumped Terahertz Quantum Well Sources
  5th International Conference on Intersubband Transitions in Quantum Wells, ITQW'99, Bad Ischl (Austria), September 7-11, 1999

- **M.Rochat**, S. Blaser, M. Beck, J. Faist, U. Oesterle, M. Illegems Electrically Pumped Terahertz Quantum Well Sources Invited seminar talk at the Semiconductor Physics Group
  Cavendish Laboratory,University of Cambridge (United Kingdom), February 7, 2000

- **M. Rochat**, M. Beck, J, Faist, H.E. Beere, A. G. Davies, E. H. Linfield, D. A Ritchie Electrically Pumped Far-infrared Quantum Well Sources, Invited talk at the Workshop on Quantum Heterostructure and Terahertz Electronics
  Institut fuer Experimentelle und Angewandte Physik, Universitat Regensburg, Regensburg (Germany), February 1s, 2001

- **M. Rochat**, M. Beck, J, Faist, H.E. Beere, A. G. Davies, E. H. Linfield, D. A Ritchie
  Latest Results on mid-IR and far-IR quantum cascade structures,
  WANTED 6 months meeting
  IEMN, Lille (France), April 4th 2001.

- **M. Rochat**, M. Beck, J. Faist
  High power (400mW) Long wavelength $\lambda = 16\mu m$ Room Temperature Quantum Cascade Laser.
  Postdeadline talk at the Conference on Lasers and Electro-Optics,
  CLEO 2001, Baltimore, MD (USA), May 6-11, 2001.

- **M. Rochat**, D. Hofstetter, M. Beck, J. Faist
  Towars a Far-infrared Quantum Cascade Laser.
  Talk at the International Conference on Intersubband Transitions, ITQW'01
  Asilomar-Monterey, CA (USA), September 10-14, 2001.

Acknowledgments

First of all, I would like to greatly thank my thesis supervisor Prof. Jérôme Faist for taking me with him "into the adventure for the quest of a new intense light source in the far-infrared". These years passed in his team are highlighted by constant enthusiasm, intellectual stimulation and cooperation. Working with him was an opportunity of great personal enrichment.

Special thanks go to the members of my thesis jury, Prof. Piero Martinoli, Prof. Karl Unterrainer and Prof. Carlo Sirtori for critically reading the manuscript and for their presence at the thesis examination.

I would like to thank Dr. Mattias Beck, Dr. Antoine Müller and Prof. Daniel Hofstetter for stimulating discussions, suggestions, questions and answers to my numerous questions and doubts. Special thanks go to Dr. Mattias Beck and Dr. Ursula Oesterle for the time they spent growing my samples.

Dr. Stéphane Blaser, my Ph.D colleague for the time we spent together either cooling down our cryostats or discussing about nearly anything including quantum physics. His help with LaTeX is still greatly appreciated!

Mr.Harald Willenberg "Monte Carlo", for also discussing about nearly anything including quantum physics and for helping me understand how electronic wave functions behave in heterostructures.

Mr. Laurent Diehl, Mr. Thierry Aellen, Mr. Lassaad Agili, Dr. Marcella Giovannini, Mr. Giacomo Scalari, Mrs. Hege Bianchini and Dr. Yargo Bonetti for their cooperation and stimulating discussions about quantum physics and nearly anything else.

Mr. Tobbias Gresh for introducing me to the Linux operating system and for helping me to solve most of the problems I encountered.

My gratitude also goes to the people working in the various departments and research groups of the Physics Institute, and more specifically the people at the workshop, the electronics and the cryogenics for the high quality of their support, their availability and their creativity.

Finally to Catherine for her constant and immoderate support.

This work was supported by the Swiss National Science Foundation.